UNIVERSIDAD DE CHILE
FACULTAD DE CIENCIAS FÍSICAS Y MATEMÁTICAS
DEPARTAMENTO DE ASTRONOMÍA

RADIO CONTINUUM OBSERVATIONS OF THE MICRO-PHYSICS OF INTER- AND CIRCUMSTELLAR DUST

TESIS PARA OPTAR AL GRADO DE
DOCTORA EN CIENCIAS, MENCIÓN ASTRONOMÍA

CARLA ALESSANDRA ARCE TORD

PROFESOR GUÍA:
SIMÓN CASASSUS MONTERO

MIEMBROS DE LA COMISIÓN:
WILLIAM DENT
MÓNICA RUBIO LÓPEZ
LUCAS CIEZA
CESAR FUENTES GONZÁLEZ

SANTIAGO DE CHILE
2023

RESUMEN DE LA TESIS PARA OPTAR AL GRADO DE
DOCTORA EN CIENCIAS, MENCIÓN ASTRONOMÍA
POR: CARLA ALESSANDRA ARCE TORD
FECHA: 2023
PROF. GUÍA: SIMÓN CASASSUS MONTERO

OBSERVACIONES DEL CONTINUO EN RADIO DE LA MICROFÍSICA DEL POLVO INTER Y CIRCUMESTELAR

El estudio de la microfísica del polvo cósmico abarca diversos fenómenos astrofísicos: desde los mecanismos de emisión en el medio interestelar, hasta la formación de planetesimales en discos circumestelares. En este contexto, los estudios observacionales de alta resolución angular permiten comprender las propiedades de los granos de polvo y su interacción con el entorno. Esta tesis se enfoca en el análisis de los mecanismos de emisión del polvo en longitudes de onda de radio, (sub)milimétricas e infrarrojas, desde la escala de tamaño de nubes moleculares, hasta la de discos protoplanetarios.

La Emisión Anómala en Microondas (AME) es un mecanismo de emisión que coincide con la radiación dipolar eléctrica de granos de polvo muy pequeños que giran rápidamente. Sin embargo, la naturaleza de los granos y los mecanismos responsables de su rotación no se han confirmado. Esta tesis presenta observaciones de alta resolución angular del *Cosmic Background Imager 2* que revelan variaciones del AME en la región de fotodisociación ρ Oph W. El máximo, a 31 GHz, se concentra en la región de fotodisociación, y muestra una fuerte correlación con la presencia local de Hidrocarburos Aromáticos Policíclicos, prevalentes en el medio interestelar. Esto sugiere que las variaciones del AME dependen de las características ambientales de la región y de sus efectos sobre las propiedades de los granos de polvo.

El campo magnético desempeña un rol importante en el colapso de los núcleos pre-estelares y en las condiciones iniciales de la formación de discos protoplanetarios. Esta tesis presenta datos de emisión de polvo polarizada de los núcleos pre-estelares en la región W43-MM1, tomados con el *Atacama Large Millimeter Array* (ALMA). El análisis de la relación entre el campo magnético y los núcleos pre-estelares en W43-MM1 sugiere que el campo magnético está fuertemente acoplado al material, y parece ser lo suficientemente fuerte a escalas circumestelares como para mantener una orientación consistente de los flujos bipolares.

Las propiedades de los granos de polvo en el medio interestelar son cruciales para analizar la evolución de los discos protoplanetarios. En los *discos de transición* se observan anillos muy brillantes y asimétricos en el continuo submilimétrico. Estas asimetrías apuntan a deformaciones en los discos internos que proyectan sombras sobre los discos externos. Esta tesis presenta observaciones multifrecuencia con ALMA y SPHERE (en el infrarrojo) del sistema DoAr 44, que confirman la presencia de decrementos de intensidad muy pronunciados en el disco externo consistentes con sombras producidas por un disco interno inclinado.

Esta tesis contribuye con nuevos resultados sobre las características de los mecanismos de emisión del polvo interestelar y su conexión con los procesos de formación de estrellas y planetas. Las conclusiones presentadas se proyectan como base para futuras observaciones multifrecuencia de alta resolución angular, en particular, para una caracterización más detallada de las propiedades del polvo en las escalas de tamaño de discos protoplanetarios.

Abstract

The area of the micro-physics of cosmic dust comprises a variety of astrophysical phenomena: from the emission mechanisms observed in the interstellar medium (ISM) to the formation of planetesimals in circumstellar disks. From the observational point of view, low frequency studies at high-angular resolutions can contribute to a better understanding of the properties of the dust grains and their interaction with their surroundings. This thesis focuses on the analysis of dust-related emission mechanisms at radio, (sub-)millimeter and infrared (IR) wavelengths, from the scale of molecular clouds, with sizes of $\sim 10\,\mathrm{pc}$, down to protoplanetary disks, with sizes of $\sim 10\,\mathrm{au}$.

The Anomalous Microwave Emission (AME) points at new micro-physics associated with dust grains. Observations have shown that AME matches the spectrum of electric dipole emission from rapidly spinning very small grains (VSGs). However, the exact nature of the VSGs and the mechanisms responsible for spinning them up remain unconfirmed. This thesis presents observations from the *Cosmic Background Imager 2* that reveal variations in the spinning dust emission across the $\rho\,\mathrm{Oph\,W}$ photo-dissociation-region (PDR). The 31 GHz emission peaks on the PDR and shows the strongest correlation with IR tracers of Polycyclic Aromatic Hydrocarbons (PAHs), ubiquitous in the ISM. This suggests that the emission variations mainly depend on the characteristics of the local environment and their effects on the properties of the VSGs.

The interstellar magnetic field is also an important environmental parameter that can be traced when interacting with dust grains. The gravitational collapse of pre-stellar cores set up the initial conditions for the formation of protoplanetary disks. This thesis uses *Atacama Large Millimeter Array* (ALMA) observations of polarized dust emission from the W43-MM1 high-mass star-forming region, that examine the relation between the magnetic field, the pre-stellar cores and their outflows. The analysis suggests that the magnetic field in W43-MM1 might be strongly coupled with the material of the cores, and it appears to be strong enough at circumstellar scales to maintain a consistent orientation of the bipolar outflows.

The physical properties of the dust grains are also crucial to understand the evolution of protoplanetary disks. In the case of *transition disks*, very bright sub-mm continuum rings surround the cavities and can be extremely lopsided. The presence of warps reveal tilted inner disks that cast shadows on outer rings, and their characterization is important due to their impact in disk evolution. This thesis presents new multi-frequency ALMA and SPHERE-IRDIS infrared scattered light observations of the disk around TTauri star DoAr 44, that confirm the presence of intensity decrements in the outer disk that are consistent with a tilted inner disk and a large continuum crescent.

This thesis provides insights on dust-related emission mechanisms aimed to improve our understanding of interstellar dust and its connection to the processes of star and planet formation. The conclusions presented on the role of ISM dust at different size-scales provide a basis for upcoming high-resolution multi-frequency observations, in particular, for a more detailed characterization of the dust properties at the size-scales of protoplanetary disks.

Para Socos, la estrella más brillante de mi universo.
Este trabajo es tuyo, como todo lo que fue y todo lo que vendrá.
Gracias por todo.

Acknowledgments

I would like to express my profound gratitude to my PhD advisor, Simón Casassus. Thank you very much for your supervision, for the trust, and for your constant support during my PhD journey. I also want to sincerely acknowledge Matias Vidal and Fabien Louvet for being the best co-supervisors. Thank you for the great advice and for answering all of my questions with incredible patience and kindness. I had the fortune of working, not only with excellent scientists, but also with great persons, and this thesis would not have been possible without their guidance. I would also like to thank Seba Pérez for his kind support through the YEMS group and the members of my thesis committee for their interest in my work.

Durante esta travesía, tuve la enorme fortuna de contar con personas increíbles. Gracias de todo corazón a Jonathan, por haber estado en las buenas, en las malas y en las peores. Gracias por creer en mi y por tu invaluable apoyo en los momentos más importantes. Agradecimiento infinito a mis hermanas de vida: Kelli, Mayra, Marita, mi Vale, Jolanda y Carla. Sus sabios consejos y su incomparable amistad hicieron más sencilla esta travesía.

En esta etapa, también conocí a maravillosas personas que ahora son amigos para toda la vida. Gracias a mis causas de Calán: el Vines, Sudeep, Blake, Nathen, Valentin y Nina, por las noches de trabajo y de carretes. Gracias a los coleguitas de la ESO: el Camilito, el Jaime, Kevin, Bibi y Alejandro, por apañar con los "academic rants" y por los increíbles recuerdos. Gracias a mis astro-amigos: a la Vale-Ciencia-en-Arte, a Rocío, a la Coni y al Diego por el apañe y la buenísima onda. Muchas gracias a todos mis amigos por hacer de Chile mi entrañable segundo hogar. Y, por supuesto, un agradecimiento especial al infaltable café.

Hay agradecimientos que datan de toda una vida, y se los debo a mi familia por siempre estar conmigo. Gracias a mi tía Maribel, por siempre estar pendiente de nosotros. Gracias a Aria, mi hijita perruna, que con sus travesuras y su cariño siempre me saca una sonrisa. Gracias a mis "hermanitos bebes" que me llevan dos cabezas en tamaño: a Tico, el músico más talentoso y disciplinado que conozco. Gracias por siempre escucharme, por ser mi cómplice y mi mejor amigo. Gracias a Yis, por quien me convertí en la hermana mayor, aunque los mejores ejemplos de fortaleza y nobleza, en realidad, me los ha dado él. Gracias a mi papito, por entender y apoyar mi curiosidad por el universo.

Pero, sobre todo, el más profundo agradecimiento se lo dedico a mi mamá. Las palabras nunca me van a alcanzar para expresarte toda la gratitud que siento, ya que si no fuera por ti, no sería quien soy. No hay nadie en el mundo a quien admire más por su fortaleza, inteligencia y enorme corazón. Siempre estuviste y seguirás estando conmigo, aquí y en cualquier rincón del universo. Este logro, y todo lo que venga en el camino, será por ti y para ti.

Table of Content

1 Introduction **1**

1.1 Cosmic dust . . . 1

1.1.1 Origins . . . 1

1.1.2 Evolution . . . 2

1.1.3 Composition and Structure . . . 3

1.1.4 Thermal dust emission . . . 6

1.1.5 The dust-correlated Anomalous Microwave Emission . . . 6

1.2 Observation and characterization of dust . . . 9

1.2.1 Absorption, scattering and optical depth . . . 9

1.2.2 Dust opacity . . . 11

1.2.3 Spectral index . . . 11

1.2.4 Polarization by dust grains . . . 12

1.3 This thesis: dust emission at different size-scales . . . 17

1.3.1 Main objective . . . 17

1.3.2 Spinning dust emission in PDRs . . . 17

1.3.3 Polarized dust emission of pre-stellar cores . . . 18

1.3.4 Dust continuum emission in protoplanetary disks . . . 19

2 Resolved observations of spinning dust emissivity variations in PDRs **20**

2.1 AME: brief state of the art . . . 20

2.2 Case of molecular cloud ρ Oph . . . 21

2.2.1 The data . . . 22
2.2.2 Qualitative Radio/IR comparisons . . . 27
2.2.3 Correlation analysis . . . 28
2.2.4 Qualitative analysis of the PAH sizes . . . 36
2.2.5 Spinning dust emissivity variations . . . 37
2.3 Summary . . . 39

3 ALMA observations of polarized dust emission at pre-stellar core-scales 40
3.1 Magnetic fields in star-forming regions . . . 40
3.2 Case of high-mass-SFR W43-MM1 . . . 41
3.2.1 Polarimetric observations . . . 41
3.2.2 Outflows, cores and magnetic field orientations . . . 43
3.2.3 Orientation between the magnetic field and the cores major axes . . . 46
3.2.4 Orientation between the magnetic field and the outflows axes . . . 47
3.2.5 Orientation between the outflows and the cores . . . 50
3.3 Summary . . . 51

4 Dust continuum observations of transition disks at au-scales 54
4.1 Warps in transition disks . . . 54
4.2 Case study of T-Tauri DoAr 44 . . . 55
4.2.1 Observations and data reduction . . . 56
4.2.2 Azimuthal profiles . . . 59
4.2.3 Radio/IR intensity decrements . . . 61
4.2.4 Warped inner disk . . . 62
4.2.5 Spectral index map . . . 64
4.2.6 Disk gas mass estimation . . . 65
4.3 Summary . . . 67

5 Conclusions and future prospects 69

5.1 Emissivity variations of PAHs: radiative torques or environmental factors? . 70
5.2 The impact of the core-scale magnetic field in W43-MM1 72
5.3 The lopsided disk of DoAr 44 73
5.4 Future prospects and upcoming work 74
5.4.1 The spectrum and characterization of resolved AME 75
5.4.2 Multi-frequency characterization of dust grains at au-scales 76

Bibliography **85**

List of Tables

2.1 Technical specifications for the CBI and CBI 2. 23

2.2 Coordinates for the observation of the ρ Oph W PDR and the pointings defined around it. S1 and SR3 are the early-type stars of interest. The angular resolution of the observation is 4.5 arcmin. 23

2.3 Flux densities and spectral indexes for source PMN J1626-2426, detected at RA 16:27:01.8, DEC -24:26:33.7 (J2000). The spectral index follows the convention $S_\nu \propto \nu^\alpha$ and it was calculated between the 31 GHz flux from the `clean` map and the catalogued fluxes. The reported fluxes correspond to different epochs, indicating variability in the spectrum. 25

2.4 Summary of the ancillary data. 26

2.5 Pearson correlations between the 31 GHz data and different templates, for the plane of the sky ($r_{\rm sky}$) and the uv-plane ($r_{\rm uv}$). 33

2.6 Pearson coefficients for the original visibility data-set and the visibility data-set using uv-tapering for an equivalent angular resolution of 13.5 arcmin (~ 3 times the original CBI 2 angular resolution). The ratio between the Pearson coefficients of the two data-sets are shown. In particular, we see that the dust radiance coefficient tends to increase the most at a lower equivalent angular resolution. 34

2.7 AME correlation slopes for ρ Oph W between typical AME frequencies and dust templates. The τ_{353} map can be considered a better dust template as it traces the dust column density. We find that most of the ρ Oph 31 GHz flux must be coming from ρ Oph W. 35

2.8 Emissivities variations in ρ Oph measured with the $\hat{j}_{\nu\,\rm proxy}$ map. 39

3.1 Central coordinates in J2000 and noise values for each pointing. We also show the noise values of the linear polarization maps ($\sigma_{\rm P}$), that we used to define the $3\sigma_{\rm P}$ and $5\sigma_{\rm P}$ thresholds to plot the polarization vectors for the individual pointings. Since we did not analyze the polarized emission in the mosaic, we only present its Stokes I noise level. The noise values are in units of mJy/beam. 43

4.1 Position angle and ring inclination values for DoAr44 from the polar optimization. 59

4.2 Summary of results from the optimization for the intensity decrements in the 230 GHz and 350 GHz continuum and $Q_\phi(H)$. 61

4.3 Observed and calculated values for the orientation of the inner disk in DoAr44 using the idealized geometrical argument. 62

4.4 Parameters for the disk mass calculation. 66

List of Figures

1.1 Representation of the evolution of interstellar matter from Tielens and Allamandola (1987). 2

1.2 Spectral energy distribution of dust in a nearby galaxy, adapted from University of Cambridge (2012). 5

1.3 SED of molecular cloud ρ Oph by Génova-Santos et al. (2015). 7

1.4 Spinning dust emissivity SEDs for different ISM phases computed with the `SPDUST` code (extracted from Dickinson et al. (2018)). 8

2.1 Mosaic of the 31 GHz continuum measured by CBI 2 in units of Jy beam^{-1}. This image was reconstructed using the CASA `clean` task. The RMS noise is $\sigma \approx 0.01$ Jy beam^{-1} and intensity contours for 3σ, 5σ, 10σ, 15σ and 20σ are shown. The star markers indicate the three early-type stars in the field: S1, SR3 and HD 147889. We also detected radio galaxy PMN J1626-2426 (labeled in the figure). The CBI 2 synthesized beam (4.6×4.0 arcmin) is shown as a green ellipse on the bottom left and the primary beam for the main pointing (28.2 arcmin FWHM) is shown as a dashed circle. 24

2.2 Overview of ρ Oph. Red: SPIRE 250 µm, green: MIPS 24 µm, blue: IRAC 8 µm (PDR). The center of the image is at RA 16:25:55.20, DEC -24:25:48.0 (J2000). The markers indicate the locations of the 3 early-type stars in the field. Contours follow a `gpu-uvmem` model of the 31 GHz continuum measured by the CBI 2, at 30%, 50%, 70% and 90% of the emission peak at 0.51 Jy beam^{-1}. The white dashed arrow indicates the direction of the cut used to construct the emission profiles of the templates. 27

2.3 Normalized emission profiles vs. distance to ionizing star HD 147889. The emission profiles in 2.3a correspond to the 31 GHz and IR maps, and the ones in 2.3b correspond to the 31 GHz and proxy maps. The profile cut, as shown by the dashed arrow in Fig. 2.2, was extracted starting from star HD 147889 and crossing the 31 GHz emission peak. 29

2.4 `clean` 31 GHz map (2.4a, close-up from Fig. 2.1), normalized proxies for PAHs column densities (2.4b-2.4e) and radiance map (2.4f). The proxies for column densities correlate better with the 31 GHz data, and the morphology between them is very similar. In 2.4a, the dashed region shows the area within which we calculated the plane of the sky correlations; it corresponds to 50% of the mosaic's primary beam. The position for the three early-type stars are also marked in each map. 30

2.5 Linear correlations between the 31 GHz data and the column density proxies $I_{12\,\mu m}/G_\circ$ (2.5a) and $f_{12\,\mu m} \cdot \tau_{250}$ (2.5b), in the plane of the sky. RMS error bars (~ 0.03 MJy sr^{-1}) are shown for the 31 GHz data. The column density proxies axis (x-axis) are normalized in both cases and their errors are negligible. 32

2.6 2.6a: Normalized 12 µm / 3 µm ratio in the ρ Oph W PDR. 2.6b: normalized emission profiles vs. distance to ionizing star HD 147889 for the 12 µm / 3 µm and 3 µm / 8 µm ratios in comparison to the 31 GHz and 250 µm emission. The profile cut corresponds to the dashed arrow in Fig. 2.2 and the black vertical lines define the PDR. 37

2.7 2.7a: CBI 2 31 GHz `gpu-uvmem` model image. 2.7b: normalized $\hat{j}_{\nu\,\mathrm{proxy}}$ map (with a peak of 2.19 ± 0.04, in arbitrary units) and 2.7c: $\hat{j}_{\nu\,\mathrm{proxy}}$ - normalized noise map (the scale corresponds to that of Fig. 2.7b). We used a mask around HD 147889 in order to avoid the bulk of the free-free emission. The observed blob towards the northern part of the filament is detected at 3σ over the noise in the CBI 2 `clean` map and could be the continuation of the PDR emission (no catalogued source was identified in that position). 38

3.1 The map displays the continuum emission at 1.3 mm of the W43-MM1 HMSFR. Contours start at 3σ with steps of 3σ, where σ=2.4 mJy/beam. Black circles illustrate 1/3 of the primary beam for each of the 5 pointings, which are further presented in Figs. 3.2 and 3.3. The magenta ellipses indicate the cores presented by Motte et al. (2018). 42

3.2 Dust polarization semi-vectors (rotated by 90° to show the inferred magnetic field orientation) over the continuum emission at 1.3 mm for pointings 1, 2 and 3 toward W43-MM1. Continuum contours levels are at 3, 5, 10, 50, and 100 σ_I (σ_I levels in Table 3.1). The semi vectors in red and blue show the magnetic field orientation where the polarized intensity exceeds a noise level of $3\sigma_P$ and $5\sigma_P$, respectively; see Table 3.1. The semi-vectors are plotted every 3 pixels, which correspond to a Nyquist spatial frequency of four vectors per synthesized beam (two in each dimension). The red and blue cones represent the red-shifted and blue-shifted outflow lobes, respectively. Circles in dashed grey represent 1/3 of the $\sim 24''$ primary beam, within which we performed the analysis. The solid green ellipse shows the synthesized beam of $0.55'' \times 0.49''$, PA = -79.4°. 44

3.3 Following Fig. 3.2: Dust polarization semi-vectors (rotated by 90° to show the inferred magnetic field orientation) over the continuum emission at 1.3 mm for pointings 4 and 5. Continuum contours levels are at 3, 5, 10, 40 $\sigma_{\rm I}$ for ($\sigma_{\rm I}$ levels in Table 3.1). 45

3.4 Cumulative distribution function (CDF, black points) of the angle difference between the magnetic field orientation and the PA of the cores in W43-MM1. The black histogram shows the CDF with 5° bin-widths. The brown bars show the errors on the CDF for each bin. Curves in color are the CDFs resulting from Monte Carlo simulations of different 3D angles projected onto the plane of the sky. The different intervals of angles considered for the synthetic populations are indicated on the bottom right of the plots. 47

3.5 Cumulative distribution function (CDF, black points) of the angle difference between the magnetic field orientation and the PA of the outflows in W43-MM1. The black histogram shows the CDF with 5° bin-widths. The brown bars show the errors on the CDF for each bin. Curves in color are the CDFs resulting from Monte Carlo simulations of different 3D angles projected onto the plane of the sky. The different intervals of angles considered for the synthetic populations are indicated on the bottom right of the plots. 48

3.6 Cumulative distribution function (CDF, black points) of the angle difference between the outflows and the PA of the cores in W43-MM1. The black histogram shows the CDF with 5° bin-widths. The brown bars show the errors on the CDF for each bin. Curves in color are the CDFs resulting from Monte Carlo simulations of different 3D angles projected onto the plane of the sky. The different intervals of angles considered for the synthetic populations are indicated on the bottom right of the plots. 50

4.1 4.1a: 230 GHz continuum restored image. The grey ellipse shows the synthesized beam (72.4 mas × 62.7 mas for Briggs 1.0). 4.1b: the 350 GHz continuum restored image. The grey ellipse shows the synthesized beam (70.2 mas × 53.8 mas for Briggs 1.0). 4.1c: H-band polarized intensity image, $Q_\phi(H)$. 56

4.2 4.2a: H-band polarized intensity image, $Q_\phi(H)$, after unresolved polarization subtraction. The green referential contours correspond to our $Q_\phi(H)$ intensity image, while the black contours correspond to the 2016 $Q_\phi(H)$ polarized intensity observations presented by paper I, both after unresolved polarization subtraction. Both intensity contours are spaced at fractions of 0.13, 0.48, 0.74 and 0.87 times the peak intensity. 4.2b: Ring intensity profiles extracted along constant radii (east of north): the green line corresponds to our $Q_\phi(H)$ observations after unresolved polarization subtraction and the black line corresponds to the previous $Q_\phi(H)$ observations, from 2016, analyzed in Avenhaus et al. (2018) and in paper I. The total height of the shaded areas correspond to $\pm 1\sigma$. 57

4.3 4.3a: the 230 GHz and the 350 GHz restored `uvmem` continuum in black and red contours, respectively, overlaid on the $Q_\phi(H)$-band image. The 230 GHz intensity contours are spaced at fractions of 0.5, 0.6, 0.7, 0.8 and 0.9 times the peak intensity and the 350 GHz contours are spaced at fractions of 0.68, 0.82 and 0.94 times the peak intensity. The contours for $Q_\phi(H)$ at 0.1, 0.5, 0.7 and 0.9 times the peak are shown in green. The grey circular marker at the center of the image indicates the position of the star (Sec. 4.2.2). The dashed circular markers indicate the location of the decrements along projected circles: black for 230 GHz and 350 GHz, and green for $Q_\phi(H)$. 4.3b: Ring intensity profiles extracted along constant radii. The green line corresponds to $I_H(\theta)$, the red line corresponds to $I_{350\ \mathrm{GHz}}(\theta)$ and the grey line corresponds to $I_{230\ \mathrm{GHz}}(\theta)$. The dashed grey and red lines mark the location of the decrements for 230 GHz and 350 GHz, respectively, and the solid green lines mark the location of the decrements for $Q_\phi(H)$. Note that the angle θ in 4.3b increases in the east of north direction. Also note that the $I_H(\theta)$ profile was integrated along a range of radii ($0.08\,\mathrm{arcsec} < r < 0.22\,\mathrm{arcsec}$) in order to obtain a better signal. The total height of the shaded areas correspond to 1σ. 60

4.4 4.4a: Spectral index map of DoAr 44, computed between 230 GHz and 350 GHz. The 350 GHz intensity profiles are shown in black contours, at 0.67, 0.77 and 0.95 times the peak, in order to highlight the location of the decrement. The grey ellipse shows the synthesized beam ($84.9\,\mathrm{mas} \times 69.9\,\mathrm{mas}$). 4.4b: Spectral index error map with 350 GHz intensity profiles in black contours, at 0.67, 0.77 and 0.95 times the peak. 65

4.5 Radial profile of the spectral index derived from the radial profiles of the 230 GHz and 350 GHz continuum following Eq. 4.1. The shaded regions trace the radial profile errors. The profile is derived following the radial range that corresponds to the values presented in Fig. 4.4a ($0.13\,\mathrm{arcsec} < r < 0.55\,\mathrm{arcsec}$). 66

4.6 Profiles $T(\phi)$ that approximate DoAr 44. The curves were computed for $a_{\mathrm{max}} = 1$ cm, $f_{\mathrm{gd}} = 100$ and $f = 1$. The direction of the gas Keplerian rotation is towards $+\phi$ 67

Chapter 1

Introduction

1.1 Cosmic dust

The life cycle of cosmic matter is the process that describes its evolution through different stages and cosmic environments: from its role in the formation of clouds in the interstellar medium (ISM) at parsec (pc) scales, to the formation of planets at astronomical unit (au) scales. In this context, cosmic dust, which accounts for $\sim 1\,\%$ of the total mass of the ISM, plays a leading role: small solid particles, less than $\sim 1\mu$m and up to a few centimeters in size, that originate from material ejected by stars and evolve to be the building blocks of pebbles, asteroids, and planets (Draine, 2011). Cosmic dust grains originate in the envelopes of evolved stars and are subsequently found in the enriched ISM. Due to their stellar origins, the chemical compositions of cosmic dust grains are varied, with carbon and silicate grains being the most common (Schlemmer et al., 2015). As the dust grains evolve through various cosmic regions, such as diffuse and dense clouds, protostellar envelopes, and protoplanetary disks, they influence the thermodynamic properties of the medium by absorbing and re-emitting interstellar radiation, as well as acting as catalysts in key chemical reactions (Whittet, 2022). In this sense, the analysis of the cosmic dust properties and its emission mechanisms has a fundamental role in tracing the physical and chemical characteristics of different cosmic environments, making it a wide and important field in theoretical and observational astrophysics.

1.1.1 Origins

Stellar spectroscopy has provided insights on the elemental composition of the stars. When comparing the detection of elements in the spectra of different kinds of stars with observations of the composition of the ISM, a depletion of heavy elements in the latter has been noticed (Draine, 2011). This characteristic suggests that these elements might be trapped in the form of dust particles. The basic components of these dust particles originate from asymptotic giant branch (AGB) stars, which are transiting through the *red giant* phase of their evolution, right after leaving the *main sequence*. AGB stars develop extended atmospheres with different

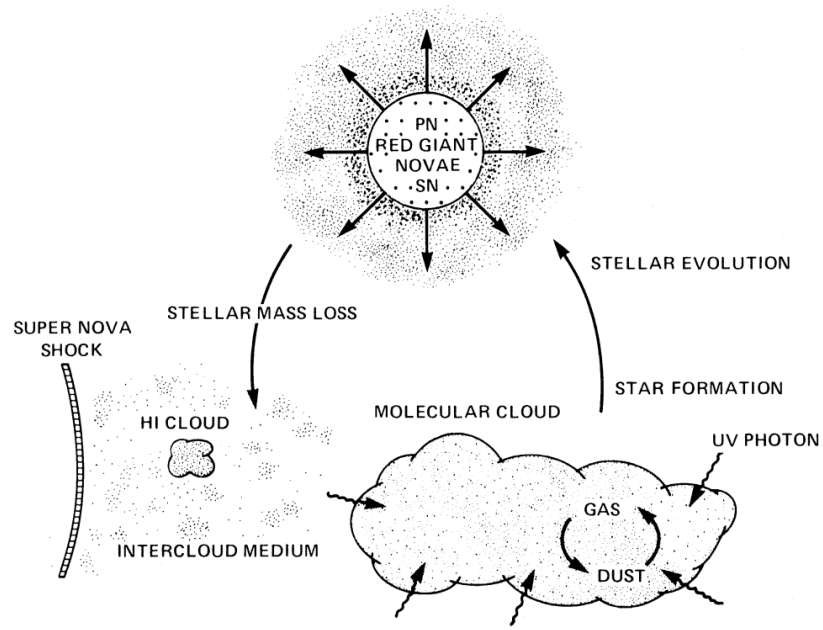

Figure 1.1: Representation of the evolution of interstellar matter from Tielens and Allamandola (1987).

chemical compositions, mainly categorized as either oxygen-rich or carbon-rich. This results in the production of different types of dust materials. In particular, oxygen-rich AGB stars contribute to the production of silicate and oxide materials. On the other hand, carbon-rich AGB stars produce carbon-based materials. Additionally, more massive stars that undergo silicon thermonuclear burning, release molecules such as silicon monoxide (SiO) and silicate dust during their supernova explosions (Schlemmer et al., 2015).

Once expelled from their parent stars, dust grains experience radiation pressure exerted by the supernova shock wave and by the interstellar radiation field (ISRF), propelling them into the ISM. In this environment, dust grains undergo transformation processes triggered by the ISRF and the surrounding gases (Whittet, 2022). These interactions lead to alterations in their physical, structural, and chemical properties. Some of the most common processes are grain destruction in shocks, low-temperature dust condensation, and grain modification due to ultraviolet (UV) radiation or heat. A schematic representation of the evolution of ISM matter is presented in Figure 1.1. All of the described stages and phenomena have a significant impact on the properties of dust particles and contribute to their evolution.

1.1.2 Evolution

The physical conditions of the ISM will determine the evolution of the dust grains properties. The characterization of these properties, constrained by observations of the dust emission, lead to the estimation of important astrophysical parameters, such as the temperature, mass or dynamics of various cosmic environments (e.g. molecular clouds, star-forming regions (SFRs) or protoplanetary disks). The main components of cosmic dust particles are the elements formed in the atmosphere of stars and scattered in their gaseous state throughout

the ISM by shock waves (Dehant et al., 2021). Therefore, the abundance of the solid-phase elements in the ISM can be estimated by comparing their abundance in gaseous state in the ISM, to their abundance in the stellar atmospheres. The estimated missing abundances in the ISM can be explained by the depletion of heavy elements in their solid phase (elements heavier than helium), which will be the main contributors to the formation of dust particles (Sofia and Meyer, 2001). The depletion of heavy elements in the ISM varies with the density of the environment. In regions with high densities this depletion is more pronounced than in cold and diffuse environments. On the other hand, cold and diffuse environments show greater depletion compared to warmer and diffuse environments. These environmental variations also contribute to the composition and characteristics of the interstellar material, including gas. Therefore, the dust to gas mass ratio can give us an estimation of the metallicity in the ISM (Draine, 2011).

Grain growth is also related to the density and temperature of the ISM, and can be describe by three stages: nucleation, coagulation and agglomeration (Shu et al., 2021). In regions with high temperatures and low densities, elements in their gas phase are more abundant due to high sublimation pressures. If the temperature decreases and density increases, the vaporized material is supersaturated and a nucleation process begins, through which very small grains (VSGs, ∼nm sizes) form due to the deposition of the gaseous elements. Since regions with high densities are better shielded from shock waves and UV radiation fields, the accretion and coagulation of grains are favored. Hence, a further decrease in temperature in a high density environment leads to an agglomeration process, through which the dust grains can grow up to micro-meter sizes (Draine, 2011). Within the ISM, other processes can also contribute to the modification of the dust grains properties, e.g. high velocity shocks, grain collisions, cosmic rays, among others (Jones and Ysard, 2019).

The growth and evolution of nanoscale ($\sim 100\,\mathrm{nm}$) to microscale ($\sim 10\,\mu\mathrm{m}$) VSGs in the ISM has been analyzed through various measurement methods. These include interstellar extinction, emission features of polycyclic aromatic hydrocarbons (PAHs) at different wavelengths, and broad-band emissions in the near and mid-infrared (IR) (Draine, 2011). The evolution of the spectral energy distribution (SED) reveal spectral features that allow for estimations of the composition, size distribution and abundances of VSGs (Kim et al., 1994). Larger grains can be traced using sub-millimeter, millimeter and microwave emission from the ISM and from the galactic background. Dust evolution models are used alongside observations to infer the dust grains properties. In these calculations, dust grains are generally approximated as spherical or cylindrical shapes for simplicity. However, it is more likely that grains have irregular shapes due to processes such as adhesion, collision, or fragmentation, and polarization of the ISRF suggests the presence of non-spherical and aligned grains (Gunkelmann et al., 2016).

1.1.3 Composition and Structure

The ISM consists of ∼70 % hydrogen, ∼25 % helium and ∼2 % heavier elements by mass. The basic elements that constitute dust grains can be categorized based on their solid-phase abundances as primary elements (carbon and oxygen) and secondary elements (magnesium, silicon and iron) (Jones and Nuth, 2011). Energetic processes in the ISM, such as shock

waves, contribute to hydrogen implantation into carbon-rich dust. Some examples of these are PAHs, hydrogenated amorphous carbons (HACs), aliphatic hydrocarbons, and fullerenes. Carbonaceous dust grains exhibit a wide variety of forms, ranging from pure crystalline carbon (diamond and graphite) to amorphous forms that are mixtures of graphite and diamonds (Jones and Ysard, 2019).

The most prominent features in the ISM extinction curve seen in Figure 1.2, between $\sim 0.1\,\mu m$ and $\sim 10\,\mu m$ (e.g. 9.7 and 18 µm for amorphous silicates, or 217.5 nm for graphite), have been used to constrain a power-law size distribution of the dust grains (also known as the *MRN size distribution*, Mathis et al., 1977; Draine and Lee, 1984), such that:

$$N(a)\,da \propto a^{-3.5} da, \tag{1.1}$$

where a is the dust grain radius, and the slope $p = 3.5$ is typical for a mixture of spherical graphite (including PAHs) and silicate grains in the ISM. From equation 1.1 we can infer that larger grains will dominate the total mass, while smaller grains will dominate the total grain surface area (Draine, 2011).

PAHs and Silicates

In particular, PAHs represent an ubiquitous component of organic matter and the largest class of carbon-based complex molecules in various cosmic environments. PAHs are large organic molecules with one or more benzene rings. Observations suggest that they enclose $\sim 20\,\%$ of the ISM carbon abundance, making them the most common molecule in the structure of dust grains. PAHs are particularly interesting as they exhibit strong emission features in the mid-IR, specifically, at 3.3 µm, 6.2 µm, 7.7 µm, 8.6 µm, 11.3 µm and 12.7 µm (Sadjadi et al., 2016), as shown in Figure 1.2. These IR bands are related to IR fluorescence that results from a UV (starlight) radiation field over the PAHs (Allamandola et al., 1985). Their characteristic large internal energy puts PAHs into highly excited states, and then back to the ground state via several IR transitions. As a consequence, PAH emission dominates at the near and mid-IR, and is widely used to trace the physical properties of the ISM and star-forming regions.

Silicates are an important component of cosmic dust as they dominate the dust emission in various astrophysical environments (Schlemmer et al., 2015). They exhibit two prominent spectral features: the Si-O stretching feature at 9.7 µm and the O-Si-O bending feature at 18 µm (Higdon et al., 2014). Even when silicates are formed at high temperatures and pressures in stellar outflows, resulting in crystalline materials under near-equilibrium conditions, the observed spectral features are broad and lack distinct characteristics (Draine and Li, 2007). This suggests that most silicates in interstellar dust are found in an amorphous state. The main types of interstellar crystalline silicates are pyroxenes and olivines. These materials are also commonly found in meteorites, and their spectroscopic signatures have been detected in the dust shells around oxygen-rich AGB stars (Jones and Ysard, 2019).

There are several other components found in the ISM dust grains, although, in lower abundances compared to hydrocarbons and silicates, e.g. metal oxides, silicon carbides,

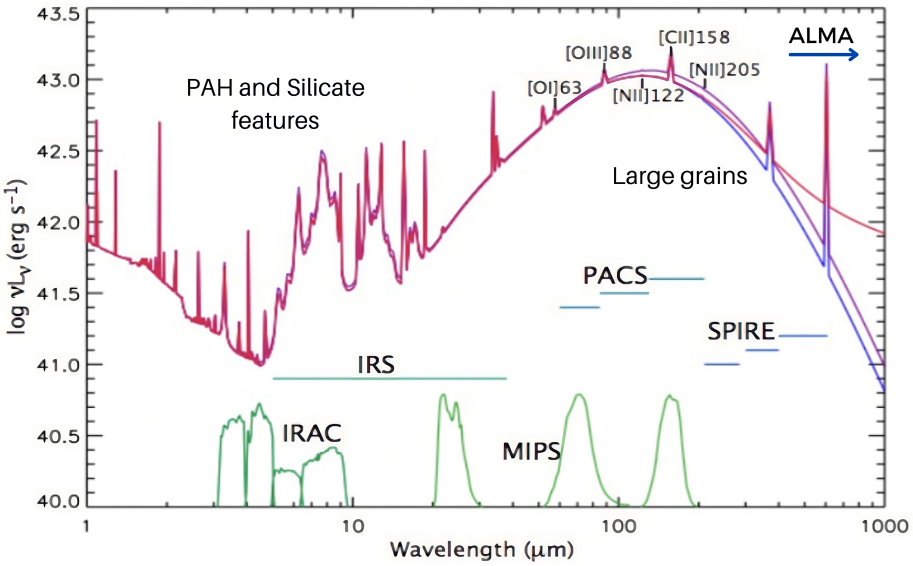

Figure 1.2: Spectral energy distribution of dust in a nearby galaxy, adapted from University of Cambridge (2012).

and various forms of iron-based metals. In primitive meteorites, micrometer-sized grains with isotopic compositions have been identified, including graphite, silicon carbide (SiC), corundum (Al2O3), and silicon nitride (Si3N4). Furthermore, presolar silica grains have been found in interplanetary dust particles (IDPs) (Schlemmer et al., 2015).

Porosity

Dust porosity describes the degree of void space or empty volume within the grain structure. During the early stages of grain formation in molecular clouds, dust grains condense from the gas phase, resulting in the aggregation of small solid particles (Krause and Blum, 2004). These aggregates can have varying levels of porosity depending on the specific conditions and mechanisms involved in their formation (Umurhan et al., 2020). Exposure to high-energy or radiation can lead to further compaction or disruption of dust grains, altering their porosity. Porosity affects certain parameters, such as thermal conductivity and optical properties, influencing the way dust grains interact with radiation.

Compact dust grains are characterized by a relatively high density and a tightly packed arrangement of constituent particles. These grains can form through various processes, such as condensation in the outflows of evolved stars or through grain growth in dense molecular clouds. Compact grains often have well-defined shapes and can exhibit crystalline structures, depending on their composition and formation history (Okuzumi et al., 2012). Due to their higher density, compact grains tend to scatter and absorb light more efficiently, have higher thermal conductivity, and are less susceptible to disruption by external forces like radiation pressure. On the other hand, fluffy dust grains are highly porous and have a weaker structure. They are composed of loosely bound aggregates or clusters of smaller particles, resulting in a low density structure. Fluffy grains can form through coagulation and agglomeration processes, where individual particles collide and adhere to each other (Kataoka et al., 2014).

As opposed to compact grains, fluffy grains tend to scatter light more diffusely, have lower thermal conductivity and are more susceptible to disruption (for a detailed review on dust porosity, see Miotello et al., 2023).

Dust evolution models have shown that grains in the ISM can grow by forming sub-micron-sized grains aggregates with porosities of up to 80% (Potapov et al., 2020). Studies of dust evolution models and laboratory experiments have revealed that grains in interstellar clouds, protostellar envelopes, and protoplanetary disks can have a highly porous structure (Clayton and Nittler, 2004; Potapov et al., 2020). Understanding the differences between compact and fluffy dust grains is important for accurately modeling their impact on various astrophysical processes, such as radiative transfer, grain dynamics, and the formation of planetary systems (Wolff et al., 1994).

1.1.4 Thermal dust emission

Historically, the presence of interstellar dust in different evolution stages has been revealed by various IR surveys, such as the Infrared Astronomical Satellite (IRS), the Multiband Imaging Photometer for Spitzer (MIPS), the Spitzer Space Telescope or the Spectral and Photometric Imaging REceiver in the Herschel telescope (Herschel-SPIRE) (their wavelength coverage is shown in Figure 1.2). The thermal state of the dust grains depends on the equilibrium between the absorbed interstellar radiation and the re-irradiated thermal emission in the mid- and far-IR (Hocuk et al., 2017). The ISRF is mainly dominated by galactic synchrotron emission, the cosmic microwave background, starlight radiation, and emission from heated grains. As a consequence, thermal dust becomes the dominant emission between $\sim 5\,\mu$m and $\sim 600\,\mu$m. Dust grains are thermalized upon contact with stellar radiation, resulting in a spectrum that derives from the continuum re-emission of a distribution of grain sizes (a), temperatures (T_d), and with various chemical compositions (Draine, 2011).

The flux density of thermal dust can be expressed as a single-component greybody curve. This is a modified blackbody with an opacity term for grains with $a > 10\,$nm. In this case, the spectral brightness depends on the frequency and the T_d, while the frequency varies according to a power law with (β_{dust}). The typical values derived for the diffuse ISM are $T_d = 17.5\,$K and $\beta_{dust} = 2$ (Draine, 2011). The smaller dust grains ($a \lesssim 10\,$nm) can reach high temperatures quickly by stochastic heating, therefore, unlike the large grains at thermal equilibrium, the spectral shape of the smallest grains does not depend on the intensity of the external radiation field. This is reflected in the total thermal emission power: two-thirds of the thermal dust emission is radiated at wavelengths $> 50\,\mu$m, and the remaining power corresponds to characteristic peaks between $3\,\mu$m and $12\,\mu$m, hence the PAHs vibrational emission bands, as seen in Figure 1.2.

1.1.5 The dust-correlated Anomalous Microwave Emission

Besides thermal emission, ISRFs upon dust grains can also result in radio emissions, in the cm and mm wavelength range. In particular, the Anomalous Microwave Emission (AME, Dickinson et al., 2018) is a dust-correlated emission detected in the 10-100 GHz frequency

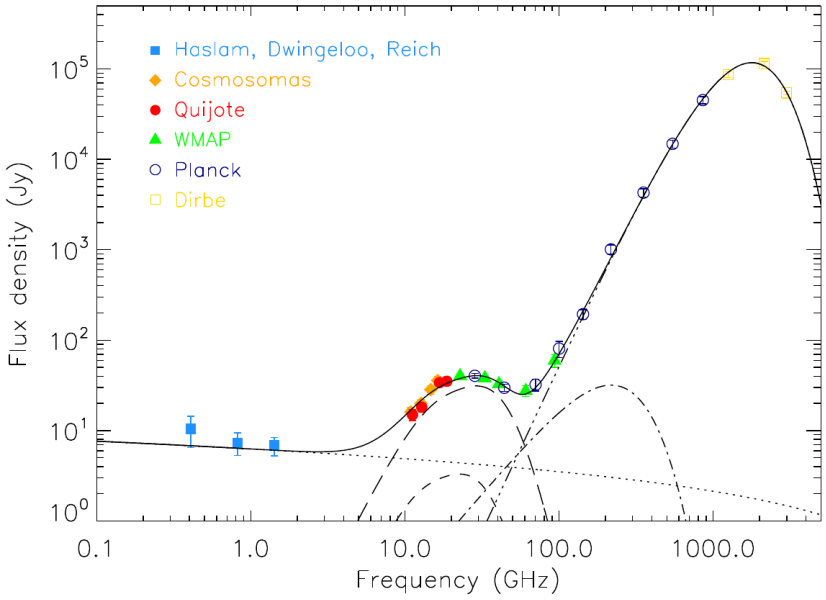

Figure 1.3: SED of molecular cloud ρ Oph by Génova-Santos et al. (2015).

range. It is an additional component, in excess of the cosmic microwave background (CMB), and separate from synchrotron, free-free and Rayleigh-Jeans dust emission. An example of the AME excess can be seen, between 10 GHz and 100 GHz, in the SED of molecular cloud ρ Oph in Figure 1.3.

AME is thought to originate from dust grains rotating at GHz frequencies that radiate through electric dipole emission. These torques can be produced due to UV radiation from an ionizing star (a *radiative torque*), or by interactions between the dust grains and ambient passing ions (*plasma drag*). The radiation produced by the rotating small grains is usually referred as *spinning dust emissivity* (j_ν), this is, the amount of radiation emitted per unit volume or column density (N_H), in units of [Jy sr^{-1} cm^2 H^{-1}] (Draine and Lazarian, 1998a). The spinning dust emissivity is defined as a function of the grains size, their angular velocity and the electric dipole moment. The intensity of the AME is expressed in terms of j_ν as:

$$I_{AME}(\nu) = N_H j_\nu / 4\pi. \tag{1.2}$$

The spinning dust model

In the *spinning dust* model, the emission from the rotating grains produce a concave spectrum that peaks around 30 GHz, at levels that can account for the observed excess. Detailed theoretical models have been constructed to calculate the spinning dust emission taking into account all the known physical effects that affect the rotation of the grains. The original Draine and Lazarian (1998a) spinning dust model takes into consideration parameters such as the grain size (of a spherical grain), the electric dipole moment of the VSG, the angular momentum of the spinning grain, the damping and excitation of the dust grains due to interaction with atoms and ions, and the total emissivity per H-atom of the spinning VSG. More refined models, that considered the wobbling of the grains, irregular grain shapes or

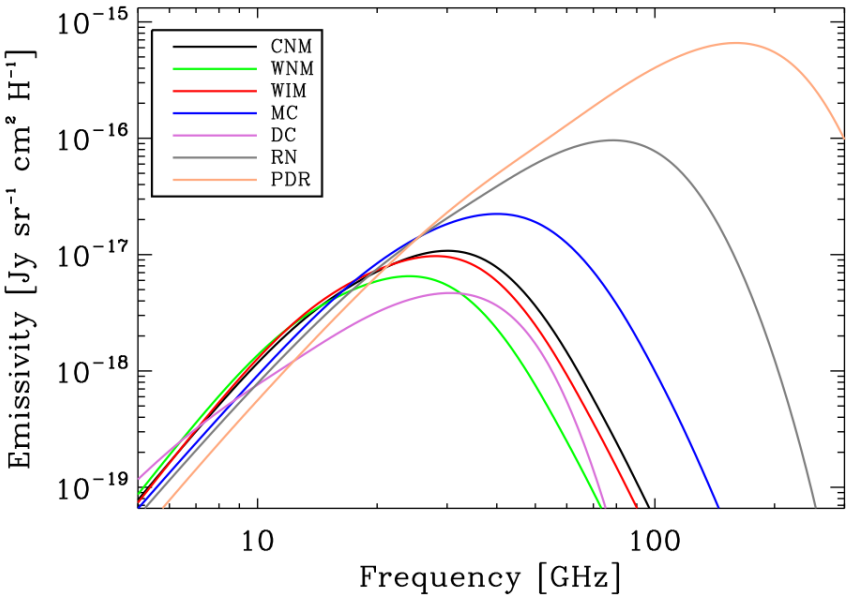

Figure 1.4: Spinning dust emissivity SEDs for different ISM phases computed with the SPDUST code (extracted from Dickinson et al. (2018)).

stochastic heating, were presented by Ali-Haïmoud et al. (2009) and Hoang et al. (2011). Using this model, spinning dust emissivity curves can be estimated for different ISM physical conditions with the SPDUST code presented in Ali-Haimoud (2010). This algorithm considers idealized ISM environmental conditions or phases: dark clouds (DC), molecular clouds (MC), cold neutral medium (CNM), warm neutral/ionized medium (WNM/WIM), reflection nebulae (RN) and photo-dissociation regions (PDR) (Ali-Haimoud, 2011). Each of these phases present different values for the following parameters: gas density, temperature, dust temperature, strength of the radiation field, the fraction of molecular, ionized hydrogen and heavier ions, dust size distribution and electric dipole moments of the grains (Dickinson et al., 2018). An example of the SEDs for each ISM phase is presented in Figure 1.4.

Figure 1.4 also shows that the peak of the spinning dust spectra depends on the environmental conditions, both in frequency and emissivity. These differences in the emissivity arise from the interactions between the dust grains and the various ISM phases, but also due to physical and chemical variations in the dust grain distribution. Within the spinning dust model, the smallest grains are the largest contributors to the emission, as they are more susceptible to the effects that govern their rotation. This has placed PAHs as a natural candidate for the AME carriers, as they are a well established nanometric-sized dust population (Tielens, 2008). Their electronic transitions and rotational properties make them efficient emitters of microwave radiation. However, the presence of nanosilicates in cosmic dust grains could also provide additional contributions to AME. Rotational nanosilicates have also been considered as the carriers of the AME and they can account for all the emission without the need of PAHs (Hoang et al., 2016; Hensley and Draine, 2017a). The exact mechanisms of silicate emission in the microwave range are still a subject of ongoing research. Several studies suggest that the heating of silicate grains by starlight or other radiation sources can induce thermal emission that contributes to the overall AME spectrum (e.g. Hoang and Lazarian, 2009; Hensley et al., 2016). The observed spectral energy distributions (SEDs) of a number

of detections are a qualitative match to spinning dust models (e.g. Planck Collaboration et al., 2014c). Thus, the spinning dust hypothesis has been the most accepted to describe the nature of the AME.

1.2 Observation and characterization of dust

Continuum emission from cosmic dust is mainly related to thermal radiation at different wavelengths (IR and (sub-)mm). Its observation and characterization depends on the interaction of the grains with electromagnetic radiation (the ISRF), through extinction (scattering and absorption), re-emission and polarization processes. UV and optical photons are absorbed and/or scattered by the dust grains and re-emitted with a certain polarization and at longer wavelengths, following a characteristic blackbody distribution (Draine, 2011). By observing this continuum emission, we can determine the temperature of the dust and infer its composition and physical properties. This technique is particularly useful for studying regions of active star formation, such as molecular clouds and protoplanetary disks, where dust grains are heated by young, hot stars.

Continuum observations of cosmic dust emission are conducted using a variety of telescopes and instruments, such as ground-based observatories and space-based missions equipped with sensitive IR and sub-mm detectors. These observations, combined with theoretical models and laboratory studies of dust properties, are key to derive the physical and chemical characteristics, namely, grain size and distribution, composition and porosity.

1.2.1 Absorption, scattering and optical depth

Cosmic dust absorption and scattering processes are fundamental phenomena that influence the propagation of electromagnetic radiation in the ISM. Their observed characteristics allow to understand processes like star and planet formation, the interaction between dust and gas in the ISM, and the evolution of galaxies. Absorption occurs when photons are absorbed by dust grains, leading to an increase in their internal energy. This absorbed energy is subsequently re-emitted as thermal radiation. On the other hand, dust scattering involves the deflection of incident photons in different directions due to interactions with dust grains. The attenuation of radiation caused by these two components is observable from mid-IR wavelengths, up to the far-UV, both in the continuum and in its spectral features (Draine, 2011).

The efficiency of the extinction will be given by the extinction coefficient, η_ν, as the sum of the absorption and scattering coefficients:

$$\eta_\nu = \varepsilon_\nu + \sigma_\nu. \tag{1.3}$$

The absorption coefficients ($\varepsilon_\nu(a)$) accounts for the fraction of radiation absorbed by the dust grains per unit length. The scattering coefficient ($\sigma_\nu(a)$) represents the fraction of

incident radiation scattered by the dust grains per unit length. Both $\varepsilon_\nu(a)$ and $\sigma_\nu(a)$ can be calculated by comparing a grain distribution model with the observed extinction.

If we consider a distribution of small spherical dust grains, with number density n_d per unit volume, the attenuation of the specific intensity due to extinction is expressed by the radiative transfer equation:

$$dI_\nu/d\tau_\nu \;=\; -I_\nu \;+\; S_\nu(T), \tag{1.4}$$

where τ_ν is the optical depth along the line of sight and $S_\nu(T)$ is the source function ($B_\nu(T)$ in the case of thermal equilibrium). Considering Z as the distance in the line of sight, the expression for the optical depth of the extinction caused by the grains is:

$$d\tau_\nu/dZ \;=\; \eta_{\tau_\nu}\, n_d. \tag{1.5}$$

The optical depth, τ_ν, describes the absorption and scattering of radiation by dust grains along the line of sight (Rybicki and Lightman, 1979). It quantifies the fraction of incident radiation that is attenuated as it passes through the dust medium. The optical depth is influenced by factors such as grain density, composition, and grain size distribution. From this expression, we can infer that the extinction of the background stellar radiation is a direct tracer of the dust column density along the line of sight.

In particular, scattering effects will become important as the dust grains approach a similar size as the observed wavelength (Miyake and Nakagawa, 1993). This will determine the scattering regimes, which can be defined using:

$$x \;=\; 2\pi a/\lambda, \tag{1.6}$$

where λ is the observed wavelength. When the size of the dust grains is much smaller than the wavelength of the incident radiation (λ), $x \ll 1$ in the Rayleigh scattering regime (Rybicki and Lightman, 1979). The scattering cross-section for the Rayleigh regime is strongly wavelength-dependent, such that $\sigma_R \propto a^6/\lambda^4$. It is more prominent for shorter wavelengths, such as blue and UV light, where the scattering cross-section is larger. The phase function for Rayleigh scattering is strongly peaked in the forward direction, meaning that the scattered radiation is primarily redirected along the incident direction. As a result, the scattered light tends to be polarized, with the electric field oscillating preferentially in the plane perpendicular to the incident direction.

On the other hand, when the size of the dust grains is much larger than the wavelength of the incident radiation, $x \gg 1$ in the geometrical scattering regime (Rybicki and Lightman, 1979). In this regime, the scattering cross-section is independent of wavelength, so it can be described using classical geometric optics principles, where the light rays are treated as straight lines. Geometrical scattering is commonly observed in macroscopic objects, such as mirrors, prisms, and lenses. It is used in various optical systems, including telescopes, microscopes, and camera lenses, where the desired behavior is to redirect and focus light.

1.2.2 Dust opacity

Cosmic dust opacity refers to the measure of how effectively interstellar dust attenuates or absorbs radiation as it propagates through the ISM. It arises due to the interaction of photons with grains through absorption and scattering, so the overall opacity of cosmic dust can be described by the so-called *opacity coefficients*: η_ν, ε_ν and σ_ν (Rybicki and Lightman, 1979).

Several factors influence the magnitude of cosmic dust opacity. These include the dust grain properties: the size, composition, and shape of dust grains significantly affect their scattering and absorption properties (Testi et al., 2014). The size distribution of dust grains in the ISM affects the overall opacity: larger grains tend to scatter light more efficiently, while smaller grains exhibit stronger absorption at shorter wavelengths (Miyake and Nakagawa, 1993; Draine, 2006). The chemical composition of the grains also plays a role, as different materials have distinct optical properties (Kataoka et al., 2014). A broader range of grain sizes can contribute to enhanced scattering and absorption over a wider range of wavelengths, and regions with higher dust densities will have higher opacities due to increased interactions with dust grains. Also, aligned dust grains with respect to magnetic fields exhibit preferential scattering in specific directions, leading to variations in opacity measurements depending on the line of sight (Dent et al., 2019).

When comparing the observed scattering intensity from a dust distribution to the estimated intensity of the ISRF, we can estimate the albedo (ω_ν) of the grains as:

$$\omega_\nu \; = \; \sigma_\nu / \eta_\nu, \tag{1.7}$$

At (sub-)mm wavelengths, where the continuum emission can trace the column densities in the ISM, the opacity coefficients have a power-law dependence on the frequency, such that,

$$\eta_\nu, \varepsilon_\nu, \sigma_\nu \propto \nu^\beta, \tag{1.8}$$

where β is the emissivity index for each dust opacity coefficient, and it depends on the maximum grain size a_{max}. The albedo, ω_ν, is also described by a power-law of the frequency with an emissivity index given by $\beta_\omega = \beta_\sigma$ - β_η. When the observed wavelength has a similar size as the dust grains, scattering becomes the main opacity source (Rybicki and Lightman, 1979).

1.2.3 Spectral index

The spectral index is defined as the slope of a power-law relationship between the observed intensity of dust emission, $I(\lambda)$, and λ (Draine, 2011). It describes how the brightness or intensity of dust emission varies with wavelength, and it is expressed as:

$$\alpha \; = \; d \, \log(I(\lambda)) \, / \, d \, \log(\lambda), \tag{1.9}$$

The common solution to the thermal emergent intensity in equation 1.4 is:

$$I_\nu \;=\; B_\nu(T)\,(1 \;-\; e^{-\tau_{\varepsilon_\nu}}), \tag{1.10}$$

which does not consider the scattering opacity coefficient (so $\varepsilon_\nu \gg \sigma_\nu$). In the Rayleigh regime (for (sub-)mm observations) and for an optically thin limit ($\tau_{\varepsilon_\nu} \ll 1$), the spectral index ($\alpha$) of the emergent intensity, $I_\nu \propto \nu^\alpha$, is related to the dust emissivity index, β as:

$$\alpha \;=\; 2 \;+\; \beta_\varepsilon \tag{1.11}$$

The emissivity index describes how the dust opacity varies with wavelength. By fitting a power law to the observed thermal emission, we obtain values for β_ε and, hence, for the size of dust grains and optical depths. For instance, $\alpha = 2$ corresponds to a dust emissivity index of $\beta_\varepsilon = 0$, indicating a flat spectrum where the intensity remains constant across wavelengths. A spectral index that deviates from $\alpha \sim 2$ falls out of the simple optically thick Rayleigh regime and suggests the presence of more complex physical processes. A spectral index value much lower than $\alpha \sim 2$ indicates an excess emission at longer wavelengths, suggesting the presence of colder dust components or a different dust composition. For $\alpha \sim 2$, low values of β_ε indicate the presence of grains with $a_{max} \gtrsim 0.1\,\mu$m, suggesting grain growth (Kataoka et al., 2014). On the other hand, a spectral index much higher than $\alpha \sim 2$, indicates a steeper decrease in intensity at longer wavelengths, which can be indicative of hotter dust components or changes in the dust size distribution (Testi et al., 2014; Sierra and Lizano, 2020). These are also the typical α values in the ISM, where $a_{max} \ll 100\,\mu$m is indicative of the presence of smaller grains, and where the typical value for the emissivity index is $\beta_\eta = \beta_\varepsilon \sim 1.7$, as $\omega_\nu \sim 0$ (Draine, 2006, 2011).

However, the effects of dust scattering are not negligible at (sub-)mm wavelengths. Estimated values for a_{max} will depend on whether β_η is actually considered for the spectral index fitting. This is the case of protoplanetary disks, where the dust opacity starts to be dominated by scattering since $100\,\mu\text{m} \ll a_{max} \ll 10\,\text{cm}$ (Testi et al., 2014; Casassus et al., 2015b, 2019a). This results in an increase of ω_ν and a broad range of observed values for the emissivity index (from ~ 1 to ~ 4). In this context, the *Mie* approach is used to describe the scattering by considering a broad range size distribution of spherical dust grains (e.g. Guillet et al., 2020). In the Mie regime, the opacity properties of the grains are estimated as a function of the variations in their refractive index, and the relation between the wavelength and the grain size. An analytical solution that relates the emergent intensity (equation 1.4) to the dust properties, and that considers the effects of self-scattering, can be obtained using the *uniform slab approximation* method, as in Sierra et al. (2019) and Casassus et al. (2023).

1.2.4 Polarization by dust grains

Magnetic fields have a significant impact on the formation and evolution of astronomical objects such as molecular clouds, stars, stellar-cores and their outflows, or protoplanetary disks. Studies on magnetic fields have been conducted at various spatial scales, ranging

from large-scale molecular clouds to smaller clumps, dense cores, and protostellar envelopes surrounding forming systems (e.g. Hull et al., 2013; Motte et al., 2018; Cortes et al., 2016). These observations have been mainly performed by high-resolution (sub)millimeter interferometers, such as ALMA, the Combined Array for Research in Millimeter-wave Astronomy (CARMA) or the Submillimeter Array (SMA). The design and capabilities of polarimetry instruments can vary depending on the specific scientific goals and wavelength ranges of interest. For instance, telescopes such as the James Clerk Maxwell Telescope (JCMT) or the Subaru use *imaging polarimeters*, that capture images of objects while simultaneously measuring their polarization properties (Greaves et al., 2003; Watanabe et al., 2018). These instruments typically employ devices such as wave plates, polarizing beam-splitters, or liquid crystal modulators to estimate the polarization state of light before it reaches the detector. *Spectropolarimeters* are also used by ground-based telescopes, such as the Very Large Telescope (VLT), or space telescopes, such as the Herschel (HST) (Watanabe et al., 2018; Leone, 2007). These are specialized instruments that measure the polarization of light as a function of wavelength to study the polarization properties of specific spectral features or entire spectral ranges. Spectropolarimeters often use techniques such as rotating wave plates or liquid crystal retarders in combination with spectrographs to analyze the spectral and polarization information simultaneously.

Polarized dust emission

In various astrophysical environments, such as molecular clouds and circumstellar disks, dust grains can become aligned with the ambient magnetic field (e.g. Chapman et al., 2013; Hull et al., 2013; Andersson et al., 2015; Hull and Zhang, 2019). An ISRF, such as UV stellar radiation, can cause dust grains to spin up and, as a consequence, contribute to an efficient alignment between the grains angular momentum and the interstellar magnetic field lines (Hoang and Lazarian, 2009). Elongated ISM dust grains with sizes $a \ll 100$ μm tend to align their long axes perpendicular to the magnetic field lines, and re-emit thermal radiation that is now polarized perpendicular to the magnetic field (Lazarian, 2007). This process is commonly observed in SFRs, where the magnetic field can be traced using the polarized thermal emission from dust grains, at (sub-)arcminute resolutions and (sub-)millimeter wavelengths (e.g. Hull et al., 2014; Cortes et al., 2016).

One of the leading mechanisms responsible for aligning dust grains with magnetic fields is known as the Radiative Alignment Torque (RAT) mechanism (Hoang and Lazarian, 2009). In the RAT mechanism, an anisotropic radiation field interacts with elongated (non-spherical) dust grains causing them to align relative to the ambient magnetic field lines. This process is most effective for grains with sizes ranging from a few tens of nanometers to a few micrometers, however, the alignment efficiency also depends on other factors, including the grain shape, composition, and the strength and direction of the magnetic field (Hull and Zhang, 2019). When the elongated grains are exposed to the radiation field, they experience an asymmetric absorption and re-emission of photons. This leads to the generation of internal radiation torques, and the resulting rotation tends to align the grains with their long axes parallel to the local magnetic field (Andersson et al., 2015). Also, the interaction between radiation torques and magnetic torques acting on the grains can cause them to precess around the magnetic field lines, resulting in grain reorientation. As a result, at the physical scales

of stellar cores and envelopes (i.e., scales smaller than ∼1000 au), dust grains aligned to the magnetic lines will emit polarized thermal radiation perpendicular to the magnetic field, which is observed as continuum polarized dust emission (e.g. Hull et al., 2014; Cortes et al., 2016, 2019). While the RAT mechanism is the dominant process responsible for the alignment of dust grains, other mechanisms, such as paramagnetic alignment, can also contribute in certain astrophysical environments (Hull and Zhang, 2019). These mechanisms operate on different grain sizes and under different physical conditions. It is also important to note that polarization from synchrotron, cyclotron and scattering might also be part of the observed polarized dust emission.

Polarization of spinning dust

The polarization of spinning dust emission plays a crucial role in the analysis of CMB polarization data (e.g. Génova-Santos et al., 2015; Planck Collaboration et al., 2016a). Due to the anisotropic nature of spinning PAHs and silicates, the radiation is preferentially emitted along a particular axis, resulting in a specific polarization pattern (Hoang et al., 2016). The electric field of spinning radiation lies in a plane perpendicular to the rotational axis, and it is prone to vary due to randomization caused by gas collisions, hence, the overall polarization is determined by the alignment of PAHs with the magnetic field (Lazarian and Draine, 2000; Hoang, 2015). Observations using sensitive polarimeters, such as the *Planck* satellite, have revealed that the polarization of AME exhibits a variety of patterns across different regions of the sky. These patterns can be influenced by a range of factors, including the size and shape of the dust grains, their composition, and the strength and orientation of magnetic fields in the interstellar medium. However, the predicted spinning dust polarization for typical ISM conditions is estimated to be negligible, below 5% (Hoang and Lazarian, 2016).

Observations of polarized emission

The magnetic field morphology onto the plane-of-the-sky can be inferred if we assume perfect grain alignment (Hoang and Lazarian, 2009). When dust grains are aligned with the magnetic field via the RAT mechanism, their long axes tend to become parallel to the local magnetic field lines. This alignment leads to a preferential polarization of the radiation emitted by the grains. This polarization is the strongest when perpendicular to the magnetic field direction and decreases as the angle between the line of sight and the magnetic field increases (Andersson et al., 2015). For an homogeneous magnetic field at large scales, we can compute the local electric vector position angle (EVPA) using the continuum Stokes Q and U maps and calculate the magnetic field morphology (BF) by rotating the EVPA by 90 deg:

$$\mathrm{BF} \;=\; 0.5\,\arctan(U/Q) + \pi/2. \tag{1.12}$$

In regions with complex magnetic field structures, superposition effects, or regions where multiple polarization mechanisms are at play, the interpretation of the observed polarization patterns can be more challenging.

The magnetic field strength (B_{POS}) can be estimated from observations of aligned dust grains that provide information about the morphology of the plane-of-sky magnetic field. In this sense, the Chandrasekhar-Fermi (CF, Chandrasekhar and Fermi, 1953; Crutcher et al., 2004) method is one of the most commonly used for estimating the magnetic field strength. It is dependent on the molecular hydrogen gas density (n_H), the velocity dispersion (FWHM) from a line tracing the gas motions (δV), and the EVPA dispersion ($\delta\phi$), such that:

$$\mathrm{B_{POS}} \;=\; 9.3\,\frac{\sqrt{n_H}\,\delta V}{\delta\phi}. \tag{1.13}$$

It has been observed that the CF method might overestimate the magnetic field strength at $\sim$1-100 pc scales due to the small angle dispersion approximation (Hull and Zhang, 2019). This has led to modifications of the $\delta\phi$ term in the CF method, by replacing it for $\delta\,\tan\phi$, where $\tan\phi \sim \delta B/B_{sky}$ (Falceta-Gonçalves et al., 2008).

It is also useful to compare the magnetic energy density of a source with other variables, such as gravity or turbulence (Hull and Zhang, 2019). The comparison between gravity, which causes inward motion, and the magnetic field, which resists infall across the field lines, is quantified by the mass-to-flux ratio (M/Φ) (Crutcher et al., 2004; Crutcher, 2012). M/Φ is often used as a metric to assess the importance of the magnetic field relative to gravity. However, a more useful measure is the ratio λ_{BF}, which is the observed mass-to-flux ratio divided by the critical mass-to-flux ratio (the critical mass that can be supported by the magnetic flux), as

$$\lambda_{BF} \;=\; (M/\Phi)/(M_{crit}/\Phi), \tag{1.14}$$

where $M_{crit} = \Phi/(2\pi\sqrt{G})$. Clouds that are supported by the magnetic field and not collapsing are considered *subcritical* ($\lambda_{BF} < 1$), while those where gravity overcomes the magnetic field resistance are *supercritical* ($\lambda_{BF} > 1$) and usually associated to active SFRs (Hull and Zhang, 2019).

ALMA polarimetry

Radio telescopes can also perform polarimetry observations at cm, and (sub-)mm wavelengths (e.g. Cortes and Crutcher, 2006; Hull et al., 2018). These instruments often use specialized antennas, such as feeds with dual linear or circular polarization capabilities. In particular, the ALMA interferometer can determine the polarization state of the observed radio emission and obtain images for each Stokes parameter (e.g. Lopez-Rodriguez et al., 2020; Bacciotti et al., 2019). A wave-splitting instrument splits the incoming radiation into two orthogonal components, X and Y. However, there could be a residual as a result of the projection from one polarization onto the other, known as *instrumental polarization* or D-terms (Cortes et al., 2016). Also, since the frame of the sky rotates with respect to the antennas, the X and Y polarizations experience a relative delay between them, introducing an angular dependence that is represented by the parallactic angle (Cortes et al., 2019).

In interferometric measurements, the absolute phase values are not measured, but rather relative values with respect to a reference target, where both X and Y polarizations have their phases set to zero. As a result, an additional phase band-pass is introduced between the XY and YX cross correlations, so a strong, unresolved, polarized source is sampled over a range of parallactic angles to derive solutions for the polarization delays and the D-terms (Hull and Plambeck, 2015; Cortes et al., 2019). ALMA also employs beam-switching polarimetry to measure the polarization properties of extended sources. In this technique, the interferometer rapidly switches between two or more beams, positioned on and off the target source. By comparing the measurements from the on-source and off-source positions, we can separate the polarization signal from the instrumental effects and background noise (Cortes et al., 2016).

Polarization by self-scattering

Given the high-resolution (au-scales) and sensitivity of interferometers such as ALMA, it has been suggested that polarized dust emission from high density and optically thick environments ($\tau \gtrsim 0.1$) could be dominated by self-scattering of large dust grains (e.g. Girart et al., 2018; Dent et al., 2019). Models of dust polarization, along with analysis of ALMA observations at au-scales (e.g. Lopez-Rodriguez et al., 2020; Lam et al., 2021), suggest that polarization at core-scales is dominated by aligned grains, but at disk-scales the main polarization mechanism is scattering. One of the main issues with polarized self-scattering is depolarization. As the scattered radiation propagates through the disk, it can interact with other dust grains and gas, causing depolarization of the signal (Kataoka et al., 2015; Brunngräber and Wolf, 2020). The extent of depolarization depends on factors such as the density and distribution of dust grains, the size distribution of the grains, and the properties of the disk itself (e.g. Tang et al., 2023). The geometry of the disk plays a crucial role in the produced polarized self-scattering. The distribution of dust grains and their alignment with respect to the disk surface can significantly affect the observed polarization patterns. Different disk geometries, such as flared, inclined, or warped disks, can produce distinct polarization signatures (e.g. Hull et al., 2018). Larger dust grains tend to have stronger scattering signals, while smaller grains may contribute differently to the observed polarization. Furthermore, the alignment of dust grains and the distribution of their minor axes with the gradient in the dust emission can also affect the polarization patterns (e.g. Kataoka et al., 2015). In this context, observing and characterizing polarized self-scattering in protoplanetary disks present technical and observational challenges, as it is necessary to determine the extent of magnetic field contributions to their polarized emission. Future observations with advanced instruments and the development of more sophisticated models will contribute to unraveling the complexities of polarized self-scattering in disks.

1.3 This thesis: dust emission at different size-scales

1.3.1 Main objective

The evolution of cosmic matter is deeply related to the ISM properties. It begins with the diffuse ISM, where densities and temperatures are low. As the ISM evolves, cold and dense interstellar molecular clouds form, which are mainly composed of molecular hydrogen, and as the density increases, these clouds collapse to form progressively denser cores. The related increase in temperatures allows for nuclear fusion and, therefore, for the birth of stars. The newborn stars are surrounded by protostellar gas and dust clouds. These envelopes eventually form protoplanetary disks, which exhibit variable density and temperature gradients, and might eventually evolve into planetary systems. When the central star in a planetary system reaches the end of its evolutionary cycle, it expands and releases its layers into the ISM, thus fueling the diffuse interstellar medium with gas and dust. In this context, the dust grains play a fundamental role in the physical and chemical processes that occur in all of the described evolutionary stages, which comprise size scales ranging from tens of parsecs to a few of astronomical units. The high-angular resolutions and powerful capabilities of radio-observatories such as ALMA and the VLA, give us the opportunity to analyze the ongoing physical processes of dust at different size scales, as well as test our current theoretical models in various astronomical regions. In this thesis, I study dust-related mechanisms at different interstellar size scales, through the analysis of multi-wavelength radio, (sub-)mm and IR observations. The main objective is to gain insights on the properties of the ISM dust and understand its role in the different stages of star and planet formation.

1.3.2 Spinning dust emission in PDRs

Low frequency emission mechanisms in molecular clouds (sizes $\sim$10-100 pc) let us understand the physical processes that are taking place due to the interaction between dust grains and the ambient fields. These are opaque interstellar dust regions composed mainly of molecular hydrogen and helium. The densest regions of these clouds, where we find considerable concentrations of dust gas, host ridges (sizes of $\sim$pc) with clumps and cores that trigger star formation. Within the complex, we also find distinctive regions of ionized hydrogen caused by the radiation field of a massive star, a process known as stellar feedback. This phenomenon results on the formation of an HII region. HII regions can also host photo-dissociation regions (PDRs): predominantly neutral regions, but with such a low column density that it would not prevent the penetration of the ultraviolet radiation field. PDRs ($T \sim 10^2$ K) can be defined as the limit between an HII ($T \sim 10^4$ K) region and the molecular cloud ($T \sim 20$ K). The radio spectral range has been widely used to study the underlying physics of molecular clouds, as radio waves are able to penetrate the dust layers, as opposed to shorter wavelengths. This lets us detect thermal and non-thermal emission of accelerated particles through the conventional radio emission mechanisms: synchrotron, free-free and thermal dust emission. Observations have shown that AME is fit by the spectrum expected from electric dipole emission due to spinning VSGs, in particular, PAHs (e.g. Scaife et al., 2010a; Ysard et al., 2010; Tibbs et al., 2011; Planck Collaboration et al., 2014c; Battistelli et al., 2015). In this sense, arc-minute

and arc-second angular resolution observations would benefit the analysis of the correlation between PAHs and the spinning dust emission.

One of the key characteristics of AME, based on observations, is that it seems to be always connected with PDRs, (Dickinson et al., 2018). PDRs seem to be optimal environments for spinning dust production, as the most significant AME detections can be traced back to PDRs (e.g. Casassus et al., 2008; Planck Collaboration et al., 2011; Vidal et al., 2011; Harper et al., 2015). Given that most of the AME observations have been made on degrees and up to a few arcminute scales, it has been difficult to isolate the precise emitting regions. In this context, resolved radio observations of well known PDRs, that include information about the morphology of the AME, are relevant, as they will allow for a direct comparison between the radio emission and IR maps that trace the dust populations. In chapter 2, I perform an analysis and quantification of the correlation between spinning dust emission and the PAHs column density in the ρ Oph W PDR. To do this, I used cm-wavelength (31 GHz) continuum data from the Cosmic Background Imager 2 at an angular resolution of 4.5 arcmin, as well as ancillary data in the mid and far-IR. These arcminute-resolution AME observations allowed me to estimate the spinning dust emissivity variations throughout the PDR with high precision. The work I present in chapter 2 has been previously published in Arce-Tord et al. (2020b).

1.3.3 Polarized dust emission of pre-stellar cores

At the scales of SFRs (sizes $\sim$0.01-10 pc), theoretical analyses have proposed that magnetic fields might play an important role in the dynamical evolution of star-forming clouds (e.g. Crutcher, 2012; Planck Collaboration et al., 2016a; Beuther et al., 2018). A few observations have suggested that the local magnetic field may have a strong influence in the evolution of stellar cores and circumstellar disks, as described by the core-collapse model (e.g. Chapman et al., 2013; Qiu et al., 2014). However, a higher fraction of consistent data is needed (Hull and Zhang, 2019). In the low-mass regime, single-dish observations provide a broad view of the magnetic field in SFRs, while interferometers like CARMA, SMA, and ALMA offer higher resolution to investigate individual stars and their environments. Key questions addressed in these studies include the role of the magnetic field in regulating the collapse of star-forming cores, the relationship between bipolar outflows and the magnetic field, and the influence of the magnetic field on the launching and collimation of outflows in low-mass protostars (Hull and Zhang, 2019).

In high-mass star formation, which occurs in clustered environments, several questions have emerged. These include understanding the dynamical role of magnetic fields in dense cores, their involvement in disk formation and protostellar outflows, and their impact on the fragmentation of molecular clumps. High-mass star formation differs from low-mass star formation due to greater fragmentation, intense radiation environments, and larger distances from Earth. In some cases, observations of polarized dust emission have revealed that the magnetic field seems to favor the formation of warped disks (e.g. Sridharan et al., 2014; Joos et al., 2012). But there is an issue with the analysis of the magnetic field behavior in the high-mass stars regime: there is a lack of significant results, so a consistent analysis in a large sample of sources is required.

In chapter 3, I analyze polarized dust emission to estimate the core-scale magnetic field orientations in SFR W43-MM1, and their relation to the cores position angle and their outflows orientations. The statistically significant sample of pre-stellar cores allowed me to analyze the local magnetic field main characteristics and its impact on the formation and evolution of the dense cores in W43-MM1. The data-set consists of ALMA Band 6 (sub-mm) polarization observations at an angular resolution of 0.5 arcsec. The work I present in chapter 3 has been previously published in Arce-Tord et al. (2020a).

1.3.4 Dust continuum emission in protoplanetary disks

The high sensitivity and angular resolution provided by ALMA are required to resolve circumstellar disks ($\sim$ 15-100 au in radius) and learn about the dust accretion processes that lead to the formation of a planetary system. In particular, several studies have focused on the physical processes that lead to grain growth and the formation of planetesimals. An interesting feature studied in disk properties are the dips and gaps produced by disk warps: an outer ring shadowed by tilted inner disks. Transition disks (TDs, Espaillat et al., 2010) are good candidates in the study of dips and warps due to their characteristic inner dust cavity, which is thought to be cleared by the orbit of a companion (Price et al., 2018). These warped transitions disks have been confirmed using resolved observations at different wavelengths. For instance, IR and optical scattered light observations of transition disk HD 142527 have reveal the presence of azimuthal dips along the outer rings (Fukagawa et al., 2006; Casassus et al., 2012; Avenhaus et al., 2014). These intensity dips are explained as shadows cast by a central warp onto the outer ring, as seen in polarized-differential imaging (PDI, Marino et al., 2015), and as suggested by the gas kinematics from ALMA observations in CO(6$-$5) (Casassus et al., 2015a).

The warped structure in TDs translates into deep shadows that cool the dust in the outer ring, causing local decrements observed in the continuum. Azimuthal dips, interpreted as narrow shadows, were also identified in HD 100453 using VLT/SPHERE polarized scattered light at optical and near-IR wavelengths (Benisty et al., 2017; Min et al., 2017). In chapter 4, I analyze the deep intensity decrements found in transition disk DoAr 44. To do this, I used ALMA Band 6 (230 GHz) long-baseline (LB) and Band 7 (350 GHz) short-baseline (SB) continuum observations with an angular resolution of $\sim$70 mas, along with follow-up SPHERE/IRDIS VLT polarized intensity data. The ALMA observations confirmed previous findings of decrements in the disk's ring, indicating the presence of a central warp, and the new scattered light image revealed changes in the disk's morphology and a misaligned inner disk. The work I present in chapter 4 has been previously published in Arce-Tord et al. (2023).

Chapter 2

Resolved observations of spinning dust emissivity variations in PDRs

This work has been published in Arce-Tord et al. (2020b)

2.1 AME: brief state of the art

Since 1996, experiments designed to measure CMB anisotropies have found a diffuse foreground in certain regions of our Galaxy in the range of 10-60 GHz. For instance, the *Cosmic Background Explorer* (COBE) satellite measured a statistical correlation between the emission at 31.5 GHz and 140 μm, at high Galactic latitudes and over large angular scales (Kogut et al., 1996). The spectral index of this radio-IR correlated signal was explained by a superposition of dust and free-free emission. Later, Leitch et al. (1997) detected diffuse emission at 14.5 GHz, which was spatially correlated with IRAS 100 μm. This emission was 60 times stronger than the free-free emission and well in excess of the predicted levels from synchrotron and Rayleigh-Jeans dust emission, thus confirming the existence of the AME (see, Dickinson et al., 2018, for a review).

Numerous detections have been made in our Galaxy by separating the AME excess from the other radio components, namely synchrotron, free-free, CMB and thermal dust emission. It has been distinctly measured by CMB experiments and telescopes at angular resolutions of $\sim 1°$; for instance, the WMAP (Bennett et al., 2013) and *Planck* (Planck Collaboration et al., 2013, 2014b) satellites have provided detailed information on diffuse emission mechanisms in the Galaxy through full-sky maps. Based on such surveys, AME accounts for $\approx 30\%$ of the Galactic diffuse emission at 30 GHz (Planck Collaboration et al., 2014b). AME has also been observed in several clouds and HII regions (e.g. Finkbeiner, 2004; Watson et al., 2005; Casassus et al., 2006; Davies et al., 2006; Dickinson et al., 2007, 2009; Ami Consortium et al., 2009; Dickinson et al., 2009; Planck Collaboration et al., 2011; Vidal et al., 2011; Planck Collaboration et al., 2014c; Génova-Santos et al., 2015), some of them being arcminute resolution observations of well known regions (Casassus et al., 2008; Scaife et al., 2010a; Castellanos et al., 2011; Tibbs et al., 2011; Battistelli et al., 2015). There have been a few

extra-galactic AME detections as well, such as in the galaxy NGC 6946 (Murphy et al., 2010a; Scaife et al., 2010b; Hensley et al., 2015; Murphy et al., 2018) and M 31 (Planck Collaboration et al., 2015; Battistelli et al., 2019). Although, extra-galactic studies are still a challenge due to the diffuse nature of the emission.

AME is thought to originate from dust grains rotating at GHz frequencies and emitting as electric dipoles. Long before its detection, Erickson (1957) proposed that electric dipole emission from spinning dust grains could produce non-thermal radio emission. Draine and Lazarian (1998b) calculated that interstellar spinning grains can produce emission in the range from 10 to 100 GHz, at levels that could account for the AME. Since then, additional detailed theoretical models have been constructed to calculate the spinning dust emission, taking into account all the known physical mechanisms that affect the rotation of the grains.

As spinning dust emission depends on the environmental conditions, a quantitative comparison between AME observations and synthetic spectra can give us information on the local physical parameters. However, even when there is a dependence on the environmental parameters, variations over a wide range of environmental conditions (e.g. typical conditions for a dark cloud versus a photo-dissociation region) only produce emissivity changes smaller than an order of magnitude (e.g. Draine and Lazarian, 1998a; Ali-Haïmoud et al., 2009). Although, greater changes in spinning dust emissivity models are observed by varying parameters intrinsic to the grain population, as shown by Hensley and Draine (2017b), where they highlighted the importance of grain size, electric dipole and grain charge distributions. Observationally, Tibbs et al. (2016) and Vidal et al. (2020) reported that they can only explain spinning dust emissivity variations in different clouds by modifying the grain size distribution for the smallest grains.

Within the spinning dust model, the smallest grains are the largest contributors to the emission. These have sub-nanometer sizes and spin at GHz frequencies. PAHs are natural candidates for the AME carriers, as they are a well established nanometric-sized dust population (Tielens, 2008), and correlations between AME and PAHs tracers have been observed (Scaife et al., 2010a; Ysard et al., 2010; Tibbs et al., 2011; Battistelli et al., 2015). However, a full-sky study by Hensley et al. (2016) found a lack of correlation between the *Planck* AME map and a template of PAH emission constructed with 12 µm data. Tibbs et al. (2013) found that in Perseus Very Small Grains (VSGs) emission at 24 µm is more correlated with AME than 5.8 µm and 8 µm PAH templates. Recently, Vidal et al. (2020) confirmed that 30 GHz AME from the translucent cloud LDN 1780 correlates better with a 70 µm map. Rotational nanosilicates have also been considered as the carriers of the AME and they can account for all the emission without the need of PAHs (Hoang et al., 2016; Hensley and Draine, 2017a). These results have raised questions about the PAHs hypothesis as the unique carriers of AME.

2.2 Case of molecular cloud ρ Oph

PDRs are optimal environments for spinning dust production (Dickinson et al., 2018): there is high density gas, presence of charged PAHs and a moderate interstellar radiation field (ISRF) that favors an abundance of small particles due to the destruction of large grains.

For instance, Pilleri et al. (2012) fitted ISO mid-IR spectra and showed that an increasing UV-radiation field in PDRs favors grains destruction. Also, Habart et al. (2003) used ISO observations and concluded that the emission in the ρ Oph W PDR is dominated by the photoelectric heating from PAHs and very small grains. The most significant AME detections have been traced back to PDRs (Casassus et al., 2008; Planck Collaboration et al., 2011; Vidal et al., 2020).

Among the most convincing observations on the spinning dust hypothesis is the ρ Ophiuchi (ρ Oph) molecular cloud, an intermediate-mass star forming region and one of the brightest AME sources in the sky (Casassus et al., 2008; Planck Collaboration et al., 2011). The region of ρ Oph exposed to UV radiation from HD 147889, the earliest-type star in the complex, forms a filamentary PDR whose brightest regions in the IR include the ρ Oph W PDR (Liseau et al., 1999; Habart et al., 2003). ρ Oph W is the nearest example of a PDR, at a distance of 134.3 ± 1.2 pc in the Gould Belt (Gaia Collaboration et al., 2018). In radio-frequencies, observations with the Cosmic Background Imager (CBI) by Casassus et al. (2008) showed that the bright cm-wave continuum from ρ Oph, for a total *WMAP* 33 GHz flux density of $\sim$20 Jy, stems from ρ Oph W and is fitted by spinning dust models. They found that the bulk of the emission does not originate from the most conspicuous IR source, S1. This motivated the study of variations of the spinning dust emissivity per H-nucleus, $j_\nu = I_\nu / N_{\rm H}$, which at the angular resolutions of their observations led to the tentative detection of j_ν.

This chapter reports Cosmic Background Imager 2 (CBI 2) observations of ρ Oph W, at a frequency of 31 GHz and an angular resolution of 4.5 arcmin. In relation to the CBI, this new data-set provides a finer angular resolution by a factor of 1.5 and better surface brightness sensitivity.

2.2.1 The data

Cosmic Background Imager 2 observations

The observations at 31 GHz were carried out with the Cosmic Background Imager 2 (CBI 2), an interferometer composed of 13 Cassegrain antennae (Taylor et al., 2011). The CBI 2 is an upgraded version of the Cosmic Background Imager (CBI, Padin et al., 2002). In 2006, the antennas were upgraded from 0.9 m (CBI) to 1.4 m dishes (CBI 2). As opposed to the CBI, CBI 2 has an increased surface brightness sensitivity at small angular scales due to the incorporation of larger dishes that provide a better filling factor for the array. Technical specifications of the CBI and CBI 2 are presented in Table 2.1.

The observations were spread over 27 days in March of 2008. The data is distributed in 6 pointings: 1 pointing centered at the ρ Oph W PDR, 3 pointings defined around the PDR, and 2 more pointings centered at stars S1 and SR3. Table 2.2 shows the coordinates for each pointing, as well as their respective RMS noise. The data-set was reduced using the standard CBI pipeline (CBICAL) and software (Pearson et al., 2003; Readhead et al., 2004a,b), with Jupiter as the main flux calibrator. As the CBI 2 is a co-mounted interferometer, the pointing error associated with each antenna has to be accounted by the combined pointing error of the baseline pairs of antennas. This yields a residual pointing error of ~ 0.5 arcmin (Taylor

Table 2.1: Technical specifications for the CBI and CBI 2.

	CBI	CBI 2
Years of operation	1999-2006	2006-2008
Observing frequencies (GHz)	26-36	26-36
Number of antennae	13	13
Number of channels (1 GHz)	10	10
Number of baselines	78	78
Antenna size (m)	0.9	1.4
Primary beam FWHM (arcmin)	45	28.2

Table 2.2: Coordinates for the observation of the ρ Oph W PDR and the pointings defined around it. S1 and SR3 are the early-type stars of interest. The angular resolution of the observation is 4.5 arcmin.

	RA[a]	DEC[b]	RMS [mJy beam^{-1}]
ρ Oph W PDR	16:25:57.0	−24:20:48.0	6.7
ρ Oph 1	16:26:06.0	−24:37:51.0	9.3
ρ Oph 2	16:26:00.0	−24:22:32.0	30.2
ρ Oph 3	16:25:14.0	−24:11:39.0	15.0
ρ Oph S1	16:26:34.18	−24:23:28.33	12.7
ρ Oph SR3	16:26:09.32	−24:34:12.18	9.6

[a,b] J2000. Right ascension are in HMS and Declinations are in DMS.

et al., 2011).

Image reconstruction

We considered two approaches to reconstruct an image from the CBI 2 data. One of them is the traditional `clean` algorithm, in which we used a *Briggs* robust 0 weighting scheme to construct a continuum mosaic. Figure 2.1 shows the reconstructed mosaic using the CASA 5.1 `clean` task (McMullin et al., 2007). This mosaic shows the location of the 3 early-type stars in the field - HD 147889, S1 and SR3. It also presents the 31 GHz intensity contours at 3σ, 5σ, 10σ, 15σ and 20σ, for an RMS noise of $\sigma \approx 0.01$ Jy beam^{-1}. The dashed circle represents the 28.2 arcmin primary beam of the central pointing (ρ Oph W PDR in Table 2.2), and the bottom left green ellipse shows the synthesized primary beam, with a size of 4.6×4.0 arcmin.

In a second approach, we used an alternative image reconstruction strategy, based on non-parametric image deconvolution, as in the maximum-entropy method (following the algorithms described in Casassus et al., 2006, 2008). Here, we used the `gpu-uvmem` package (Cárcamo et al., 2018), implemented in GPU architectures. Thanks to entropy regularization and image positivity, the model image can super-resolve the `clean` beam, in the sense that its effective angular resolution is $\sim$1/3 that of the natural-weighted beam (so even finer than uniform weights). To obtain a model sky image that fits the data we need to solve the usual deconvolution problem, i.e. obtain the model image I^m that minimize a merit function L:

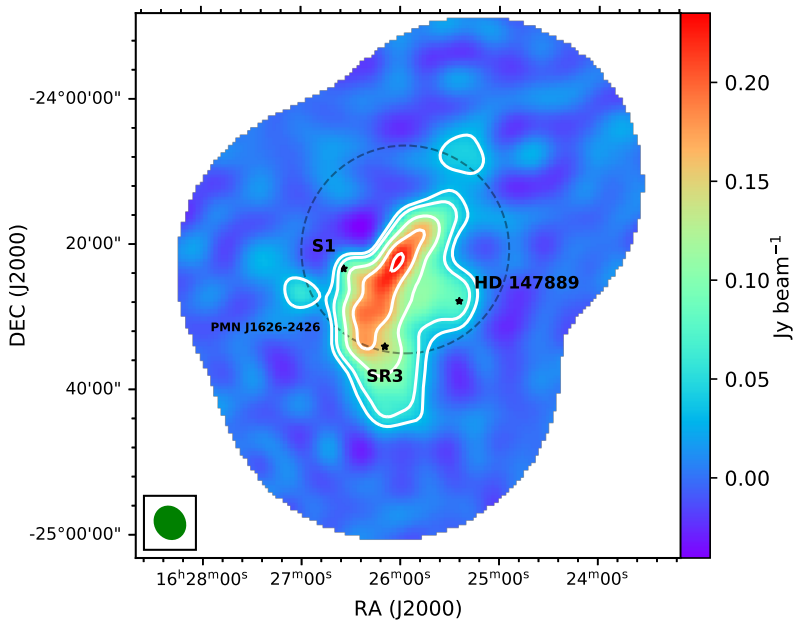

Figure 2.1: Mosaic of the 31 GHz continuum measured by CBI 2 in units of Jy beam^{-1}. This image was reconstructed using the CASA `clean` task. The RMS noise is $\sigma \approx 0.01$ Jy beam^{-1} and intensity contours for 3σ, 5σ, 10σ, 15σ and 20σ are shown. The star markers indicate the three early-type stars in the field: S1, SR3 and HD 147889. We also detected radio galaxy PMN J1626-2426 (labeled in the figure). The CBI 2 synthesized beam (4.6×4.0 arcmin) is shown as a green ellipse on the bottom left and the primary beam for the main pointing (28.2 arcmin FWHM) is shown as a dashed circle.

$$L = \chi^2 - \lambda \sum_i p_i \ln(p_i/M), \tag{2.1}$$

where

$$\chi^2 = \frac{1}{2} \sum_{k=0}^{N} \omega_k ||V_k^\circ - V_k^m||^2. \tag{2.2}$$

Here, V_k° are the observed visibilities, each with weight ω_k, and V_k^m are the model visibilities calculated on the model images. The optimization is carried out by introducing the dimensionless free parameters $p_i = I_i/\sigma_D$, and M is the minimum value for the free parameters. In this case, we set $M = 10^{-3}$ and $\lambda = 2 \times 10^{-2}$. The `gpu-uvmem` algorithm also estimates a theoretical noise map as

$$\sigma = \sqrt{\frac{1}{\sum_{p=1}^{P} \overline{A}_p^2/\hat{\sigma}^2}}, \tag{2.3}$$

where P is the number of pointings, $\overline{A}_p = \sum_{f=1}^{F} A_{\nu_f}/F$ is the mean of the primary beams over all frequencies $\{\nu_f\}_{f=1}^{F}$ available in pointing p, and $\hat{\sigma}$ is the noise on the dirty map using natural weights. Error propagation in the dirty map yields:

$$\hat{\sigma} = \sqrt{\frac{1}{\sum_k \omega_k}}. \tag{2.4}$$

Table 2.3: Flux densities and spectral indexes for source PMN J1626-2426, detected at RA 16:27:01.8, DEC -24:26:33.7 (J2000). The spectral index follows the convention $S_\nu \propto \nu^\alpha$ and it was calculated between the 31 GHz flux from the `clean` map and the catalogued fluxes. The reported fluxes correspond to different epochs, indicating variability in the spectrum.

Observing Frequency [GHz]	Flux Density [mJy]	$\alpha_{(\nu/31\,\mathrm{GHz})}$
1.4	57.2 ± 1.8 [a]	0.01 ± 0.03
4.8	132 ± 13 [b]	-0.43 ± 0.07
8.4	77.9 [c]	-0.21
20	78 ± 5 [d]	-0.61 ± 0.25
31	59.6 ± 5.3 [e]	-

[a] Reported in Condon et al. (1998).
[b] Reported in Griffith et al. (1994).
[c] Reported in Sowards-Emmerd et al. (2004). Error not reported.
[d] Reported in Murphy et al. (2010b).
[e] Reported in this work.

In order to avoid an under-estimation of errors, we scaled the noise map so that its minimum value would match the RMS noise of the natural-weighted `clean` map. In increasing the noise level, we also included a correction for the number of correlated pixels in both maps, i.e. the noise in the `gpu-uvem` model image is increased by $\sqrt{N_{\mathrm{clean}}/N_{\mathrm{uvmem}}} \sim 3$, where N_{clean} and N_{uvmem} are the number of pixels in each `clean` beam, and that of `gpu-uvmem` being $\sim$3 times smaller than the natural-weight beam.

In this analysis, we used both the `clean` and `gpu-uvmem` maps. The `clean` map was used to measure the correlation of the 31 GHz emission with the IR templates and the proxies for PAHs. We did not use the `gpu-uvmem` map to perform the correlations as it has a variable angular resolution. Instead, as the `gpu-uvmem` map recovers the morphology of the 31 GHz emission in detail, we used it to construct an emissivity proxy to analyze the emissivity variations throughout the PDR.

In the reconstructed `clean` mosaic, we detected a point source located at RA 16:27:01.8, DEC -24:26:33.7 (J2000) that corresponds to the radio galaxy PMN J1626-2426 (labeled in Figure 2.1). This source is described in the PMN catalogue as a Flat Spectrum Radio Source, located at RA 16:27:00.01, DEC -24:26:40.50 (J2000) (Healey et al., 2007). In Table 2.3 we report the flux and spectral index ($S_\nu \propto \nu^\alpha$) of this point source at 31 GHz, along with catalog measurements at other frequencies. We measured the flux at 31 GHz using aperture photometry with a circular aperture of radius 2.5 arcmin. It is interesting to point out that this source has a *Fermi* detection of 0.35 ± 0.04 pJy at 50 GeV (Nolan et al., 2012), observed during 2008 and 2010. Its radio spectrum shows variability, especially considering the flux difference between the 1.4 GHz data, observed during 1993, and the 4.8 GHz data, observed during 1990 (see Table 2.3). The 8.4 GHz and 20 GHz data were taken during 2003 and 2006, respectively.

Ancillary data

The Wide-Field Infrared Survey Explorer (WISE) has surveyed the entire sky in four near-IR and mid-IR band-passes (Wright et al., 2010). Its near-IR survey at 3.4, 4.6 and 12 µm gives information on the emission from VSGs and PAHs in the interstellar medium. We worked with the 3.4 µm map, and the 12 µm processed map by (Meisner and Finkbeiner, 2014), who smoothed the data-set to an angular resolution of 15 arcsec and removed the compact sources and optical artifacts from the image. We also used their map at 22 µm for comparison purposes.

Dust grain tracers were also obtained from the InfraRed Array Camera (IRAC) maps from the *Spitzer* Space Telescope survey. IRAC is a mid-IR camera with four channels at 3.6, 4.5, 5.8, and 8 µm (Fazio et al., 2004). In this case, we used the 8 µm template. The original data-set is presented in units of MJy sr^{-1} and at an angular resolution of $\sim$2 arcsec. We also used the 24 µm data-set from the *Spitzer* Multiband Imaging Photometer (MIPS) (Rieke et al., 2004). This photometer works at 24, 70 and 160 µm, producing maps with a native angular resolution between 6 and 40 arcsec.

Table 2.4: Summary of the ancillary data.

Instrument	Wavelength [µm]	Description
Spitzer-IRAC	8	Tracer for PAHs.[a]
WISE	3.4, 12	Tracer for PAHs.[a]
WISE	22	Tracer for VSGs.
Spitzer-MIPS	24	Tracer for VSGs.
Herschel-SPIRE	250	Tracer for big classical grains [b]

[a] In ρ Oph W, this bands are dominated by PAHs. The 3.4µm map is a better tracer for the smallest PAHs.
[b] Grains with sizes of $\sim$ hundreds of nm in thermal equilibrium.

In the particular case of ρ Oph W, both 8 µm and 12 µm bands are dominated by PAHs. Given the radiation field in HD 147889 ($\chi \sim 400$, Habart et al. (2003)) and for typical dust models (Draine and Li, 2007; Compiègne et al., 2011), we expect both bands to be tracing primarily PAHs.

To study the thermal dust emission we used data from the *Herschel* Gould Belt survey, which provides an extensive mapping of nearby molecular clouds, including detailed templates of ρ Oph (André et al., 2010; Pilbratt et al., 2010). Specifically, we used data from the Spectral Photometric Imaging Receiver (SPIRE), a three-band camera and spectrometer that works at 250, 350 and 500 µm (Griffin et al., 2010). We also worked with the dust temperature data-set from the Photodetector Array Camera and Spectrometer (SPIRE – PACS), that has a native angular resolution of 36.3 arcsec (Ladjelate et al., 2020). A summary of the ancillary data is presented in Table 2.4.

2.2.2 Qualitative Radio/IR comparisons

In Figure 2.2 we compare the CBI 2 31 GHz emission reconstructed with the `gpu-uvmem` algorithm (Sect. 2.2.1) shown in contours, with the IRAC 8 µm in blue colour stretch, MIPS 24 µm in green, and SPIRE 250 µm in red. The 8 and 24 µm templates trace the emission of small hot grains (sub-nm and nm-sizes), while the 250 µm template traces thermal dust emission, mainly from big classical grains (size of hundreds of nm). In particular, the IRAC 8 µm template is a main tracer of PAHs in this region.

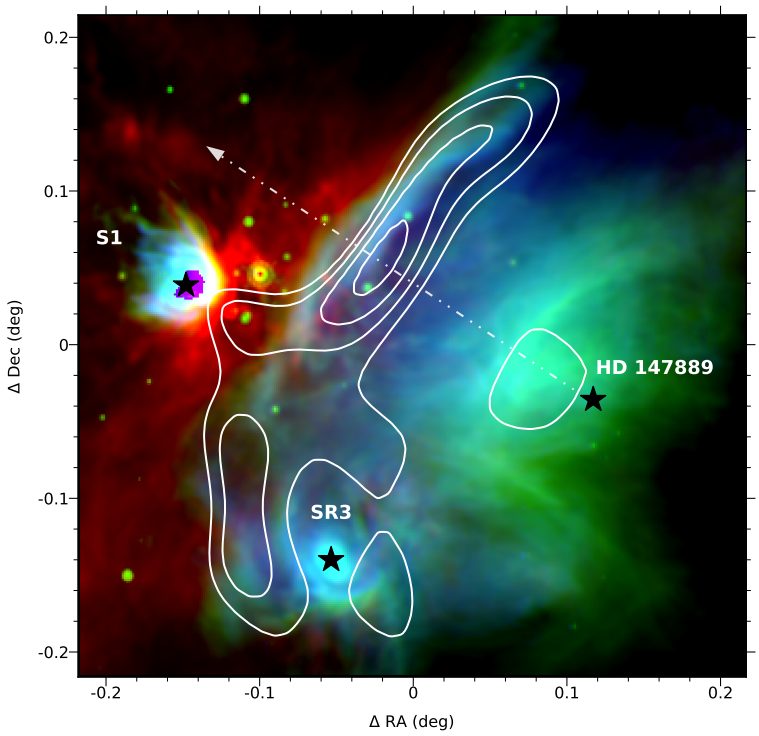

Figure 2.2: Overview of ρ Oph. Red: SPIRE 250 µm, green: MIPS 24 µm, blue: IRAC 8 µm (PDR). The center of the image is at RA 16:25:55.20, DEC -24:25:48.0 (J2000). The markers indicate the locations of the 3 early-type stars in the field. Contours follow a `gpu-uvmem` model of the 31 GHz continuum measured by the CBI 2, at 30%, 50%, 70% and 90% of the emission peak at 0.51 Jy beam^{-1}. The white dashed arrow indicates the direction of the cut used to construct the emission profiles of the templates.

The black markers in Fig. 2.2 show the position of the three early-type stars in ρ Oph. S1 is a binary system composed of a B4V star and a K-type companion, with an effective temperature of $T_{\rm eff} \approx 15800$ K. SR3, also known as Elia 2-16, is a B6V star with an effective temperature of $T_{\rm eff} \approx 14000$ K. HD 147889, the main ionizing star of ρ Oph, is catalogued as a single B2III/B2IV star (C-ionizing, Houk and Smith-Moore (1988)), with $T_{\rm eff} \approx 23000$ K (Bondar, 2012). This star is heating and dissociating gas layers creating an HII region of $\sim$6 arcmin towards the PDR traced by the free-free continuum in the PMN (Parkes-MIT-NRAO) 4.85 GHz map, and by the Hα emission in SHASSA (Casassus et al., 2008). Figure 2.3a shows normalized emission profiles for the IR templates and the 31 GHz data, for a cut starting from HD 147889 and passing through the 31 GHz emission peak, as shown by the dashed arrow in Fig. 2.2. We also plot the emission profile from the PMN 4.85 GHz map

as a tracer of the free-free emission throughout the region. We find that, indeed, most of the 4.85 GHz emission comes from the vicinity of HD 147889. The 24 μm map in Fig. 2.2 also shows thermal emission from hot grains near HD 147889. Towards the PDR (at ∼6 arcmin in Figure 2.3) and through the peak of the 31 GHz emission, the 4.85 GHz emission decreases, reaching the noise level of the original map. This lack of free-free emission at the location of the PDR can also be seen in the 1.4 GHz and Hα maps of ρ Oph presented in Planck Collaboration et al. (2011).

An interesting aspect of Fig. 2.2 is that the 31 GHz contours fall in the transition between small hot grains and bigger colder grains (reflected in the layered structure of the IR tracers, as also seen in Fig. 2.3a). This transition occurs at the PDR, where neutral Hydrogen becomes molecular. Deeper into the molecular core, away from HD 147889 in Fig. 2.2, the UV radiation field is attenuated, and the emergent emission progressively shifts towards 250 μm.

Figure 2.3a shows that IRAC 8 μm and WISE 12 μm have a wider radial profile than that at 31 GHz, ranging from their peak at ∼5 arcmin distance from HD 147789 up to ∼15 arcmin. Note that around 5 arcmin there is a slight hump on the 31 GHz profile that matches the peak of IRAC 8 μm. Also, at ∼10 arcmin, the WISE 12 μm profile shows a hump at the position of the 31 GHz peak. This correlations might imply a relation between the rotational excitement of dust grains that originate the spinning dust emission and the vibrational states of the small grains seen in the 8 μm and 12 μm profiles.

We note that the most conspicuous feature in the IR-map in Fig. 2.2, the circumstellar nebula around S1, shows a very faint 31 GHz counterpart. This is particularly interesting as *Spitzer* IRS spectroscopy shows very bright PAHs bands in the nebulae around S1 and SR3, as well as in the ρ Oph W PDR (Habart et al., 2003; Casassus et al., 2008). This means that PAHs are not depleted around S1 and SR3, thus making the faint 31 GHz emission intriguing. Motivated by this, we performed a correlation analysis in order to quantify the best tracer of the 31 GHz emission throughout the region.

2.2.3 Correlation analysis

We study the morphological correlation between the 31 GHz data and different IR maps that trace PAHs and VSGs. In order to avoid biases due to image reconstruction, we also performed the correlations in the visibility (uv) plane. To transform the data-set to the uv-plane we used the `MOCKCBI` software from the CBI software tools. This program calculates the visibilities by Fourier-transforming a supplied map of the sky emission, in this case, various IR templates. To do this, all templates were reprojected to a 1024×1024 grid. In case that any of the original templates were of a smaller size, a noise gradient, calculated with the RMS noise limits of each map, was added to the borders. This is an important step to consider, otherwise, the resulting visibility maps would show an abrupt step towards its borders, producing artefacts in the mock visibilities. To visualize and compare the trend of the results we also calculated the correlations in the plane of the sky. We smoothed all the templates to 4.5 arcmin in order to fit CBI 2's angular resolution. All templates were re-gridded to ∼3 pixels per beam to avoid correlated pixels.

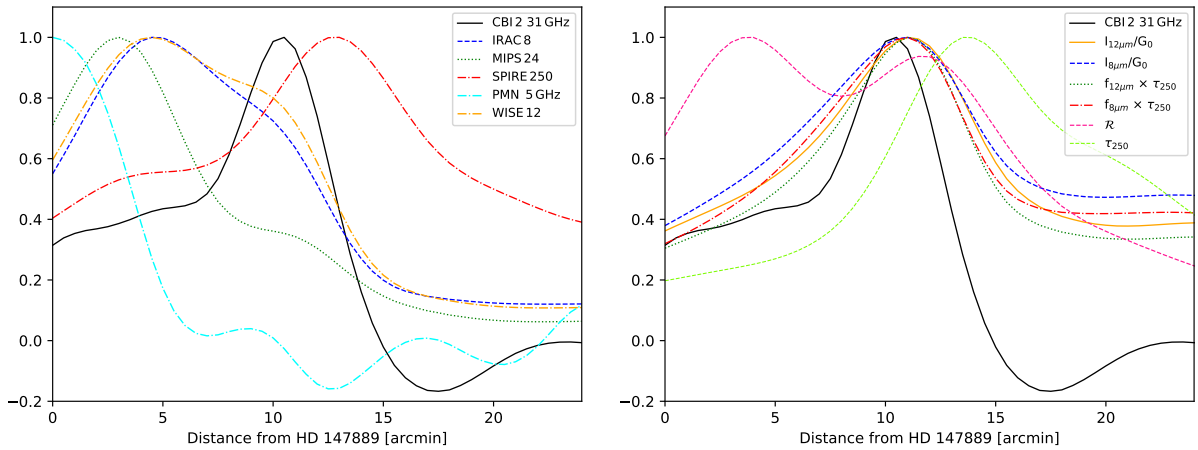

(a) (b)

Figure 2.3: Normalized emission profiles vs. distance to ionizing star HD 147889. The emission profiles in 2.3a correspond to the 31 GHz and IR maps, and the ones in 2.3b correspond to the 31 GHz and proxy maps. The profile cut, as shown by the dashed arrow in Fig. 2.2, was extracted starting from star HD 147889 and crossing the 31 GHz emission peak.

PAH column density proxies

For the correlation analysis, we constructed proxies for the column density of PAHs. The mid-IR dust emission, due to PAHs, depends on the column density of the emitters and on the intensity of the local UV radiation, which can be quantified in units of the ISRF in the solar neighbourhood as the dimensionless parameter G_0 (Sellgren et al., 1985; Draine and Li, 2007). If the observed 31 GHz emission corresponds to spinning dust emission, a stronger correlation is expected with the mid-IR emission when divided by G_0, as this will trace the column density of PAHs.

The radiation field intensity was estimated using the equation given by Ysard et al. (2010):

$$G_0 \; = \; (T_{\rm dust}/17.5K)^{\;\beta_{\rm dust}+\;4}. \tag{2.5}$$

This method derives from radiative equilibrium with a single grain size of 0.1 µm and an emissivity index[1] $\beta_{\rm dust} = 2$, which is constant across the field. As $\beta_{\rm dust}$ may vary throughout the PDR, a constant β might not be a good approximation for G_0. We estimated the impact of variable $\beta_{\rm dust}$ in Eq. 2.5. We created a map of $\beta_{\rm dust}$ and $T_{\rm dust}$ by fitting a Modified Black Body to the far-IR data. For this, we used Herschel data at 100, 160, 250, 350 and 500 µm. This fit results in $\beta_{\rm dust}$, τ and $T_{\rm dust}$ maps that would let us identify variations in the PDR at 4.5 arcmin. The resulting G_0 map, calculated with the variable $\beta_{\rm dust}$ and $T_{\rm dust}$ maps from the fit, is morphologically equivalent to the G_0 estimation using a constant $\beta_{\rm dust}$ and Herschel's $T_{\rm dust}$ map. The Pearson correlation coefficient is $r = 0.95 \pm 0.02$ between both G_0 estimations. In this work, we are interested in comparing the morphology of the cm-wavelength (31 GHz) signal with that of the average radiation field along the line of sight. A 3D radiative transfer model that accounts for the IR spectral variations would provide an accurate estimation of

[1]This is the spectral index of the grain opacity.

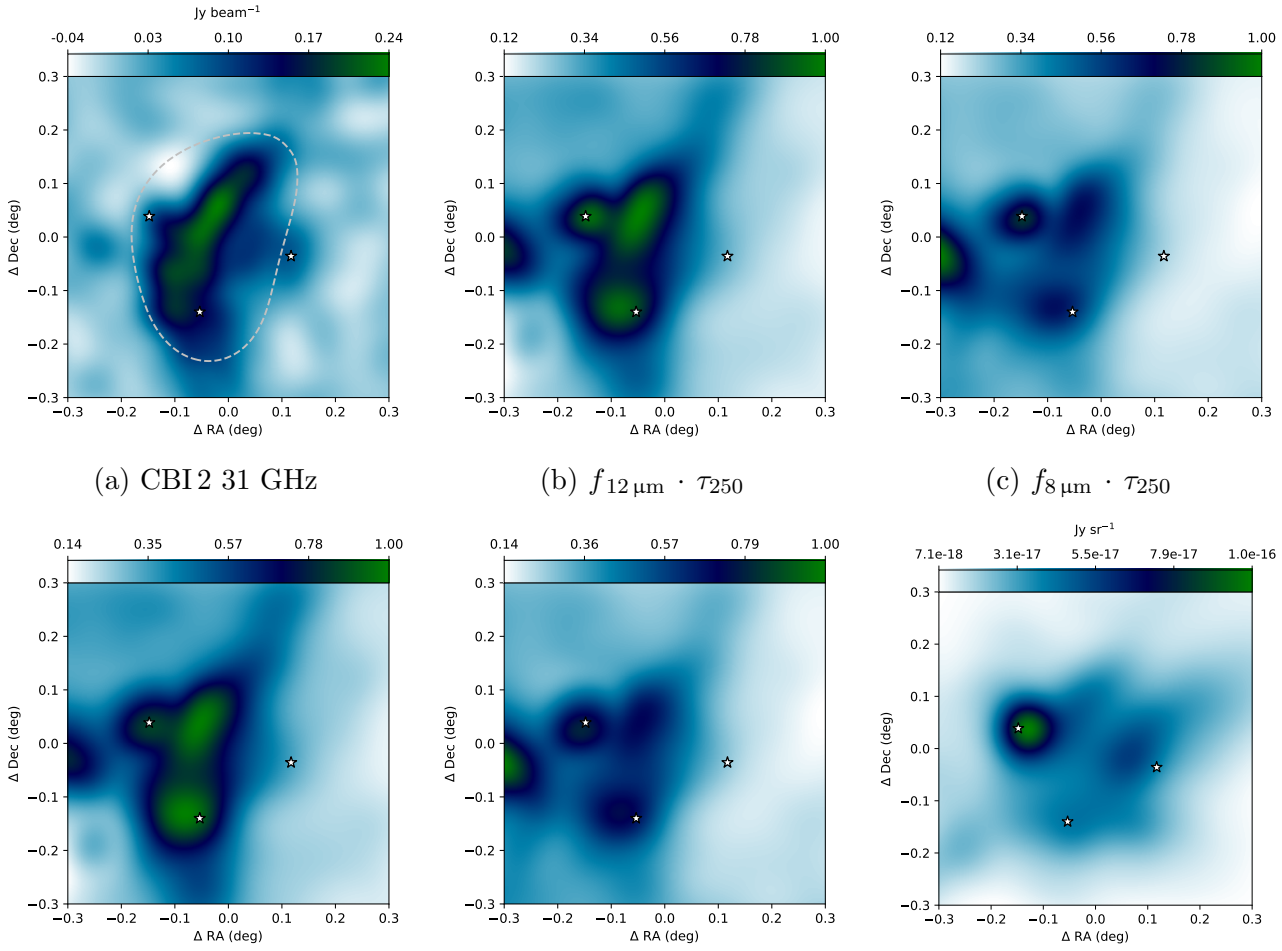

(a) CBI 2 31 GHz (b) $f_{12\,\mu\mathrm{m}} \cdot \tau_{250}$ (c) $f_{8\,\mu\mathrm{m}} \cdot \tau_{250}$

(d) $\mathrm{I}_{12\,\mu\mathrm{m}}/G_0$ (e) $\mathrm{I}_{8\,\mu\mathrm{m}}/G_0$ (f) $\mathcal{R}/\nu$

Figure 2.4: `clean` 31 GHz map (2.4a, close-up from Fig. 2.1), normalized proxies for PAHs column densities (2.4b-2.4e) and radiance map (2.4f). The proxies for column densities correlate better with the 31 GHz data, and the morphology between them is very similar. In 2.4a, the dashed region shows the area within which we calculated the plane of the sky correlations; it corresponds to 50% of the mosaic's primary beam. The position for the three early-type stars are also marked in each map.

the 3D UV radiation field ($G_0(\vec{x})$) and of the dust abundances (e.g. as in Galliano, 2018). Such modeling is beyond the scope of this work.

In stochastic heating, we expect the intensity of the IR bands due to PAHs to be approximately proportional to both the UV field intensity and the PAH column, so that (as in Casassus et al., 2008):

$$\frac{I_{\nu\,\mathrm{PAH}}}{G_0} \propto N_{\mathrm{PAH}}. \tag{2.6}$$

As templates for the PAHs emission, $I_{\nu\,\mathrm{PAH}}$, we used the WISE 12 µm and IRAC 8 µm intensity maps.

Another way to obtain a proxy for the column of PAHs, proposed by Hensley et al. (2016), is to correct $I_{\nu\,\mathrm{PAH}}$ by the dust radiance ($\mathcal{R}$) as a method to quantify the fraction of dust in PAHs (f_{PAH}). The dust radiance corresponds to the integrated intensity, $\mathcal{R} = \int_\nu I_\nu$. We calculated this expression by considering a modified blackbody as in Planck Collaboration et al. (2014a) (equation 10):

$$\mathcal{R} = \tau_{250}\frac{\sigma_S}{\pi}\,T_{\mathrm{dust}}^4\left(\frac{kT_{\mathrm{dust}}}{h\nu_0}\right)^{\beta_{\mathrm{dust}}}\frac{C(4+\beta_{\mathrm{dust}})\,\zeta(4+\beta_{\mathrm{dust}})}{\Gamma(4)\,\zeta(4)}, \tag{2.7}$$

where τ_{250} is the optical depth at 250 µm, calculated using $\tau_{250} = I_{250\,\mu\mathrm{m}}/B_{250\,\mu\mathrm{m}}(T)$ by assuming an optically-thin environment. Also, ν_0 is the frequency for 250 µm, σ_S is the Stefan-Boltzmann constant, k is the Boltzmann constant, h is the Planck constant and Γ and ζ are the Gamma and Riemann-zeta functions, respectively. To recover the intensity units of the radiance map, we divide it by ν_0, getting as a result $\mathcal{R}/\nu$. Hence, the PAH fraction can be calculated as:

$$\frac{\nu\,I_{\nu\,\mathrm{PAH}}}{\mathcal{R}} \propto f_{\mathrm{PAH}}. \tag{2.8}$$

Thus, the product of the PAH fraction times the optical depth will be proportional to the PAH column density:

$$f_{\mathrm{PAH}} \times \tau_{250} \propto N_{\mathrm{PAH}}. \tag{2.9}$$

We note that Hensley et al. (2016) stress the need of a good correlation between the mid-IR map and $\mathcal{R}$, which is the case of the 4.5 arcmin $I_{\nu\,\mathrm{PAH}}$ and $\mathcal{R}$ maps, with correlation coefficients $r > 0.6$. Figure 2.4 shows a close-up of the 31 GHz `clean` mosaic, along with the column density proxies constructed with WISE 12 µm and IRAC 8 µm, and the radiance map.

Pearson correlation analysis

Figure 2.5 shows the scatter plots using the 31 GHz data and column density proxies $I_{12\,\mu\mathrm{m}}/G_0$ and $f_{12\,\mu\mathrm{m}} \cdot \tau_{250}$ in the plane of the sky. These scatter plots suggest a linear dependence between the CBI 2 data and each template, which justifies the use of the Pearson coefficient as a statistical measurement of the correlation. The Pearson correlation coefficient, r, provides

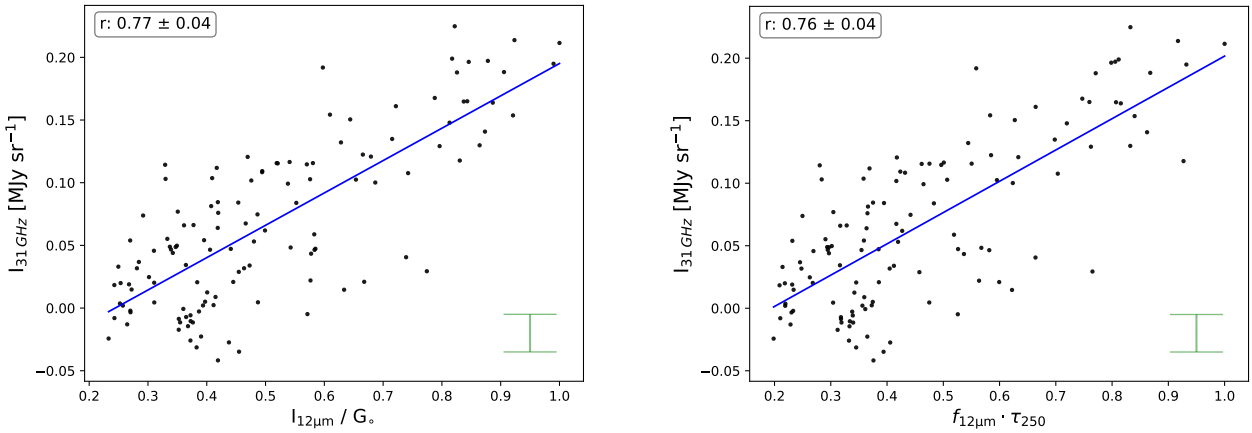

(a) (b)

Figure 2.5: Linear correlations between the 31 GHz data and the column density proxies $I_{12\,\mu m}/G_\circ$ (2.5a) and $f_{12\,\mu m} \cdot \tau_{250}$ (2.5b), in the plane of the sky. RMS error bars (~ 0.03 MJy sr^{-1}) are shown for the 31 GHz data. The column density proxies axis (x-axis) are normalized in both cases and their errors are negligible.

a way to quantify and compare the degree of correlation between the 31 GHz signal and different templates, both in the *uv*-domain,

$$r_{uv} = \frac{\sum_k \omega_k \left(Vx_k - \overline{V}x\right)\left(Vy_k - \overline{V}y\right)}{\sqrt{\sum_k \omega_k \left(Vx_k - \overline{V}x\right)^2 \sum_k \omega_k \left(Vy_k - \overline{V}y\right)^2}}, \tag{2.10}$$

where ω_k is the weight for visibility datum V_k, and $\overline{V}x = \sum_k \omega_k Vx_k / \sum_k \omega_k$ and $\overline{V}y = \sum_k \omega_k Vy_k / \sum_k \omega_k$ are the weighted means of visibility data-sets Vx and Vy, respectively; and in the sky-plane

$$r_{\rm sky} = \frac{\sum_i (x_i - \overline{x})(y_i - \overline{y})}{\sqrt{\sum_i (x_i - \overline{x})^2 \sum_i (y_i - \overline{y})^2}}, \tag{2.11}$$

where $\overline{x}$ and $\overline{y}$ are the mean values of data-sets x and y, respectively.

The correlations in the *uv*-plane ($r_{\rm uv}$) are calculated for the entire visibility data-set. On the other hand, the sky-plane cross-correlations are taken inside an area equivalent to half the mosaic's primary beam FWHM, shown as a dashed region in Figure 2.4a. This helps us avoid noisy outliers and measure the correlation within the area of interest, which is the PDR. We also masked the PMN galaxy identified in Figure 2.1.

The uncertainties in $r_{\rm sky}$ were estimated with a Monte Carlo simulation. We added random Gaussian noise to the 31 GHz `clean` mosaic, before dividing by the mosaic attenuation map, with a dispersion given by the RMS noise of the 31 GHz `clean` mosaic. In each run of the simulations, the resulting 31 GHz intensity map is correlated with the corresponding template, and the final error in $r_{\rm sky}$ is the standard deviation of all the correlation coefficients. In the *uv*-plane, the $r_{\rm uv}$ errors are calculated under the same logic, but instead, we add random Gaussian noise to each visibility datum V_k using a dispersion given by its weight

$\omega_k = 1/\sigma_k^2$, common to both the real and imaginary parts. We are interested in the relative variations of the Pearson coefficients between the templates, so any bias due to systematic errors will be the same for all the maps.

Table 2.5: Pearson correlations between the 31 GHz data and different templates, for the plane of the sky ($r_{\rm sky}$) and the *uv*-plane ($r_{\rm uv}$).

Template	$r_{\rm uv}$	$r_{\rm sky}$
WISE 3	0.25 ± 0.01	0.61 ± 0.04
IRAC 8	0.26 ± 0.01	0.68 ± 0.04
WISE 12	0.29 ± 0.01	0.72 ± 0.04
WISE 22	0.15 ± 0.01	0.52 ± 0.04
MIPS 24	0.15 ± 0.01	0.51 ± 0.04
SPIRE 250	0.08 ± 0.01	0.40 ± 0.04
τ_{250}	-0.04 ± 0.01	0.11 ± 0.04
$\mathcal{R}/\nu$	0.13 ± 0.01	0.51 ± 0.04
$f_{3\,\mu\rm m}$	0.17 ± 0.01	0.23 ± 0.04
$f_{8\,\mu\rm m}$	0.23 ± 0.01	0.32 ± 0.02
$f_{12\,\mu\rm m}$	0.25 ± 0.01	0.37 ± 0.02
$f_{3\,\mu\rm m} \cdot \tau_{250}$	0.27 ± 0.01	0.70 ± 0.04
$f_{8\,\mu\rm m} \cdot \tau_{250}$	0.28 ± 0.01	0.59 ± 0.04
$f_{12\,\mu\rm m} \cdot \tau_{250}$	0.34 ± 0.01	0.76 ± 0.04
$\rm I_{3\,\mu m}/G_0$	0.29 ± 0.01	0.71 ± 0.04
$\rm I_{8\,\mu m}/G_0$	0.26 ± 0.01	0.60 ± 0.04
$\rm I_{12\,\mu m}/G_0$	0.34 ± 0.01	0.77 ± 0.04

The resulting values for the correlation coefficients are listed in Table 2.5. We observe the same trends in both $r_{\rm sky}$ and $r_{\rm uv}$, although the sky-plane results show higher correlations. This difference is expected, as the sky correlations were extracted within 50 % of the primary beam area, while the *uv*-plane correlations used all of the visibilities, which are integrated quantities over the whole primary beams.

Figure 2.3b shows the cuts for the normalized radiance, τ_{250}, and column density proxies, starting from star HD 147889 and passing through the 31 GHz emission peak (as shown by the arrow in Figure 2.2). Here, we see that the column density proxies of the small grains peak around the same location as the 31 GHz data. Note the shift of the IRAC 8µm and WISE 12µm profiles between Fig. 2.3a and their column density proxies in Fig. 2.3b. It is also interesting to highlight that the location of the bump in the WISE 12µm profile (at around 10 arcmin in Fig. 2.3a) matches the 31 GHz peak. This leads to a stronger correlation between both templates, which is also reflected in Fig. 2.3b, where $\rm I_{12\,\mu m}/G_0$ and $f_{12\,\mu\rm m} \cdot \tau_{250}$ are narrower and show a more similar profile to the 31 GHz data. As shown in Table 2.5, the best correlation is indeed with PAH column density proxy $\rm I_{12\,\mu m}/G_0$. The role of the WISE 3µm map as a tracer for smaller PAHs will be discussed in Sec. 2.2.4.

Note that, in Figure 2.3b, the radiance profile shows two peaks: one around 5 arcmin from HD 147889, which is related to hotter dust grains nearby the star, and a second one along the PDR but shifted ∼2 arcmin from the 31 GHz profile, which is related to a larger optical depth (τ_{250}). The τ_{250} peak, which traces the concentration of big grains, is shifted towards the

molecular cloud, matching the peak of SPIRE 250 µm (Fig. 2.3a) at ∼13 arcmin. Table 2.5 shows that the τ_{250} map does not correlate with the 31 GHz map, while the correlation coefficient for the radiance template ($\mathcal{R}$) is moderate. Historically, sub-mm templates have been used to trace dust emission (Dickinson et al., 2018), but, in this case, the quantification of the sub-mm emission is better traced by the radiance in comparison with τ_{250} or the intensity at any given sub-mm frequency. This is consistent with the result by Hensley et al. (2016) where the radiance template is the best tracer for the AME.

Correlation analysis as a function of angular resolution

The cross-correlations also depend on angular resolution. We repeated the correlations in the *uv*-plane for an equivalent angular resolution of 13.5 arcmin, closer to the approximate maximum recoverable scale (∼ three times the CBI 2 synthesized beam). To do this, we applied a *uv*-taper by multiplying the visibility weights with a Gaussian, $W = \exp\left(-(u^2+v^2)/t^2\right)$. The results are presented in Table 2.6, which also shows the ratio between the Pearson coefficients of the original and the tapered data-set. These correlations show the highest increase for $\mathcal{R}/\nu$ and τ_{250}, but note that the correlation for τ_{250} is very close to zero. We also calculated the correlations in the sky plane by smoothing the templates to angular resolutions of 9 and 13.5 arcmin and observed the same tendency: the Pearson coefficient of the dust radiance maps increases the most at lower angular resolutions, while the column density proxies tend to remain equal.

Table 2.6: Pearson coefficients for the original visibility data-set and the visibility data-set using uv-tapering for an equivalent angular resolution of 13.5 arcmin (∼ 3 times the original CBI 2 angular resolution). The ratio between the Pearson coefficients of the two data-sets are shown. In particular, we see that the dust radiance coefficient tends to increase the most at a lower equivalent angular resolution.

Template	$r_{\rm uv}$	$r_{\rm uv-13.5'}$	Ratio
WISE 3	0.25 ± 0.01	0.32 ± 0.02	1.3 ± 0.1
IRAC 8	0.26 ± 0.01	0.35 ± 0.02	1.3 ± 0.1
WISE 12	0.29 ± 0.01	0.37 ± 0.02	1.3 ± 0.1
WISE 22	0.15 ± 0.01	0.20 ± 0.01	1.4 ± 0.1
MIPS 24	0.15 ± 0.01	0.20 ± 0.02	1.3 ± 0.2
SPIRE 250	0.08 ± 0.01	0.09 ± 0.01	1.1 ± 0.2
τ_{250}	-0.04 ± 0.01	-0.06 ± 0.01	1.5 ± 0.4
$\mathcal{R}/\nu$	0.13 ± 0.01	0.20 ± 0.02	1.5 ± 0.2
$f_{3\,\mu\rm m}$	0.17 ± 0.01	0.21 ± 0.02	1.2 ± 0.1
$f_{8\,\mu\rm m}$	0.23 ± 0.01	0.29 ± 0.02	1.3 ± 0.1
$f_{12\,\mu\rm m}$	0.25 ± 0.01	0.31 ± 0.02	1.2 ± 0.1
$f_{3\,\mu\rm m} \cdot \tau_{250}$	0.27 ± 0.01	0.34 ± 0.01	1.3 ± 0.1
$f_{8\,\mu\rm m} \cdot \tau_{250}$	0.28 ± 0.01	0.37 ± 0.03	1.3 ± 0.1
$f_{12\,\mu\rm m} \cdot \tau_{250}$	0.34 ± 0.01	0.42 ± 0.03	1.2 ± 0.1
$\rm I_{3\,\mu m}/G_0$	0.29 ± 0.01	0.37 ± 0.03	1.3 ± 0.1
$\rm I_{8\,\mu m}/G_0$	0.26 ± 0.01	0.34 ± 0.03	1.3 ± 0.1
$\rm I_{12\,\mu m}/G_0$	0.34 ± 0.01	0.42 ± 0.03	1.2 ± 0.1

The fact that the radiance template shows the highest relative increase in its Pearson coefficient could explain the results obtained by Hensley et al. (2016), where their dust radiance template correlated the best with their AME template at an angular resolution of 1°. Based on their correlation results, they concluded that PAHs might not be responsible for the AME. This is not the case for the 4.5 arcmin maps, so PAHs cannot be ruled out as possible spinning dust carriers. In this PDR, the 8 µm and 12 µm bands are dominated by PAHs (see, e.g. Habart et al., 2003; Draine and Li, 2007; Compiègne et al., 2011), so the fact that we found a good correlation between these bands and the 31 GHz emission indicates that the PAHs might be important AME emitters.

AME correlation slopes

Table 2.7: AME correlation slopes for ρ Oph W between typical AME frequencies and dust templates. The τ_{353} map can be considered a better dust template as it traces the dust column density. We find that most of the ρ Oph 31 GHz flux must be coming from ρ Oph W.

Frequency [GHz]	Angular Resolution	Correlation slope	Units	Template	Reference
31	4.5 arcmin	15.5 ± 0.2	10^6µK	τ_{353}	This work.
22.8	1°	23.9 ± 2.3	10^6µK	τ_{353}	Dickinson et al. (2018)
31	4.5 arcmin	2.18 ± 0.04	µK / (MJy sr^{-1})	100 µm (IRIS)	This work.
22.8	1°	8.3 ± 1.1	µK / (MJy sr^{-1})	100 µm (IRIS)	Dickinson et al. (2018)

Typically, AME emissivities have been quantified with correlation slopes in terms of IR emission (e.g. $I_{30\,GHz}$ / $I_{100\,\mu m}$) or using an optical depth map ($I_{30\,GHz}$ / $\tau_{353\,GHz}$) (see Dickinson et al. (2018)). We calculated the correlation slope between the 31 GHz data, and τ_{353} and IRIS 100 µm. For this, we measured the mean emission within the PDR filament using intensities larger than 15σ (as the contour defined in Fig.2.1) in the primary beam corrected `clean` map. The original angular resolutions for the τ_{353} and IRIS 100 µm maps (5 and 4.3 arcmin, respectively) are very similar to CBI 2's angular resolution of 4.5 arcmin. Table 2.7 lists the values for the AME correlation slopes. We also show the correlation slopes measured with the same templates by Dickinson et al. (2018), at an angular resolution of 1°. We find that a large fraction of the AME correlation slope measured in ρ Oph on scales of 1° must be coming from the ρ Oph W PDR. This is especially evident when using the τ_{353} map, where the AME correlation slope of the 4.5 arcmin ρ Oph W PDR observations is ∼65% of the AME correlation slope of the 1 ° ρ Oph observations. ρ Oph W shows the highest AME emissivity in terms of the τ_{353} map, which is considered as a very reliable dust template as it traces the dust column density (Dickinson et al., 2018). These emissivities are about a factor 2-3 higher than other values measured at high Galactic latitudes and also in Perseus, the brightest AME source in the sky according to Planck Collaboration et al. (2011). A possible explanation for the larger slope in ρ Oph W could be found in the finer linear resolution in this work, of ∼0.2 pc, compared to ∼2.3 pc in Planck Collaboration et al. (2011). The fact that ρ Oph is closer to us means that we can resolve the AME from the PDR. When integrated in the telescope beam (e.g. Planck analysis over 1° scales), there is proportionally a larger amount of AME coming from the high density and excited PDR compared to the emission from the regions that have lower emissivities, i.e. AME from the denser cores, or from the more diffuse gas.

Spectral index

The wide frequency coverage of the CBI 2 correlator, between 26 GHz and 36 GHz, may place constraints on the spectral properties of the 31 GHz signal. We split the visibilities (V) in two sub-sets: one for the low frequency channels (6-10) centered at 28.5 GHz, and one for the high frequency channels (1-5) centered at 33.5 GHz. We then calculated the correlation slopes (a^{High}, a^{Low}) between the two sub-sets and the mock visibilities for $I_{12\,\mu m}/G_0$ (the best correlated proxy), following:

$$V_{31\,\mathrm{GHz}}^{\mathrm{High/Low}} = a^{\mathrm{High/Low}}\, V_{12\,\mu m/G_0}. \tag{2.12}$$

Note that $\log(a^{High}/a^{Low})$ is proportional to the spectral index α. We obtained a spectral index of $\alpha = 0.05 \pm 0.08$, which indicates a flat spectrum. However, we must also take into account the difficulty of obtaining a reliable spectral index due to any possible calibration and systematic errors. The spectral index measured between the low and high frequency channel is nonetheless consistent with the shape of the ρ Oph spectrum in Planck Collaboration et al. (2011).

2.2.4 Qualitative analysis of the PAH sizes

The results in Table 2.5 show that column density proxies of PAH tracers at 3 µm, 8 µm and 12 µm correlate the best with the 31 GHz emission. Note that, in particular, the 3 µm band is dominated by the smallest PAHs (sizes ∼0.4 nm), which are the most prone to destruction by UV radiation, while the 8 µm and 12 µm bands, in comparison, are dominated by bigger PAHs. Given this, a good tracer of the PAH sizes is the 12 µm / 3 µm ratio map (Allamandola et al., 1985; Ricca et al., 2012; Croiset et al., 2016). To construct it, we removed the point sources in the WISE 3 µm map, and smoothed both the WISE 12 µm and 3 µm maps to CBI 2's angular resolution. Figure 2.6a shows the 4.5 arcmin map for the 12 µm / 3 µm ratio, along with the 31 GHz contours (same contours as in Fig. 2.1). At this angular resolution, it is interesting to note the increment of the ratio in the transition between the PDR and the molecular cloud to the East in Fig. 2.6a. This is also seen in Fig. 2.6b, where we see the normalized emission profiles for the cut in Fig. 2.2 vs. the distance to the ionizing star HD 147889. Here, the minimum of the 12 µm / 3 µm ratio is aligned with the PDR surface (defined by the first black vertical line, ∼6 arcmin in Fig. 2.6b), while the peak of the ratio occurs at the transition between the PDR and the molecular cloud (defined by the second black vertical line, ∼14 arcmin in Fig. 2.6b). This peak might be an indication that the PAHs size increases in the PDR towards the molecular cloud.

The 3 µm / 8 µm ratio map can also give us an indication of the contribution of the smallest PAHs. We calculated the plane of the sky correlation between the 3 µm / 8 µm ratio and the 31 GHz emission, and obtained a Pearson coefficient of $r_{\mathrm{sky}} = -0.21 \pm 0.03$. The low value of the anti-correlation indicates that the smallest grains do not necessarily correlate better with the 31 GHz map, as it can also be seen in Table 2.5, where the correlation in WISE 3 is not better than with IRAC 8. Fig. 2.6b also shows the normalized profile for the 3 µm / 8 µm ratio. The behaviour of this template is similar to the 12 µm / 3 µm map, but shifted towards the interior of the molecular cloud. Overall, these ratios reveal a factor of ∼1.5 variation in the size of the emitting PAHs throughout the ρ Oph W PDR.

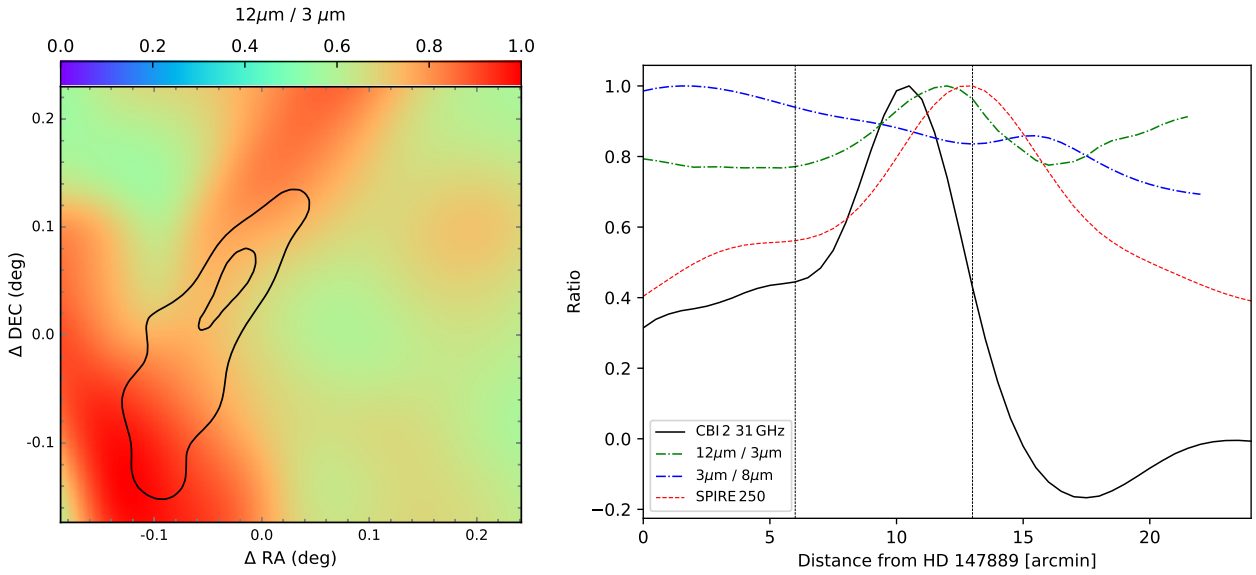

(a) (b)

Figure 2.6: 2.6a: Normalized 12 µm / 3 µm ratio in the ρ Oph W PDR. 2.6b: normalized emission profiles vs. distance to ionizing star HD 147889 for the 12 µm / 3 µm and 3 µm / 8 µm ratios in comparison to the 31 GHz and 250 µm emission. The profile cut corresponds to the dashed arrow in Fig. 2.2 and the black vertical lines define the PDR.

2.2.5 Spinning dust emissivity variations

In the correlation analysis (Sec. 2.2.3) we found that the 31 GHz map correlates best with $I_{12\,\mu m}/G_0$, a template for the PAH column density. Also, we note that there is significant scatter about the linear cross-correlations between the 31 GHz emission and the PAH column density proxies, as shown in Fig. 2.5. Motivated by this, we study the possibility that this scatter is produced by spinning dust emissivity variations along the PDR.

In order to assess the extent to which the physical mechanisms leading to the 31 GHz emission depend on the local environment, we tested for the hypothesis that the emergent 31 GHz intensity is *only* proportional to the column of the emitters, i.e. $N_{\rm PAH}$. We construct a proxy that will let us measure any emissivity variation in the PDR as in Casassus et al. (2008), and define the 31 GHz emissivity per spinning dust emitter (i.e. PAHs in the hypothesis for this thesis), $\hat{j}_\nu$, which should be proportional to the spinning dust emissivity per H-nucleus for a fixed grain population:

$$\hat{j_\nu} \equiv \frac{I_\nu(31\mathrm{GHz})}{N_{\rm PAH}} \propto j_\nu \equiv \frac{I_\nu}{N_H}. \tag{2.13}$$

Using Eq. 2.6 we can propose a proxy for $\hat{j_\nu}$:

$$\hat{j}_{\nu\,\mathrm{proxy}} \equiv \frac{I_\nu(31\mathrm{GHz})}{I_{12\,\mu m}/G_0}. \tag{2.14}$$

The `gpu-uvmem` model images for $I_\nu^{\rm uvmem}(31\mathrm{GHz})$ and $I_{12\,\mu m}^{\rm uvmem}/G_0$ provide a finer angular resolution than the `clean` mosaic, and may pick up larger variations in emissivity. Figure 2.7

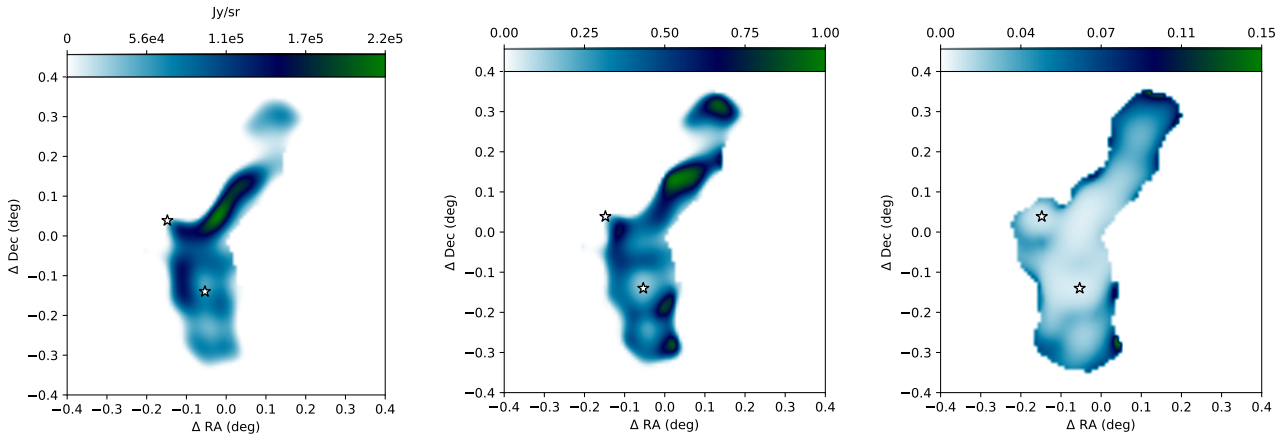

(a) `gpu-uvmem` model map (b) `gpu-uvmem` $\hat{j}_{\nu\,\mathrm{proxy}}$ map (c) $\hat{j}_{\nu\,\mathrm{proxy}}$ noise map

Figure 2.7: 2.7a: CBI 2 31 GHz `gpu-uvmem` model image. 2.7b: normalized $\hat{j}_{\nu\,\mathrm{proxy}}$ map (with a peak of 2.19 ± 0.04, in arbitrary units) and 2.7c: $\hat{j}_{\nu\,\mathrm{proxy}}$ - normalized noise map (the scale corresponds to that of Fig. 2.7b). We used a mask around HD 147889 in order to avoid the bulk of the free-free emission. The observed blob towards the northern part of the filament is detected at 3σ over the noise in the CBI 2 `clean` map and could be the continuation of the PDR emission (no catalogued source was identified in that position).

shows $I_{\nu}^{\mathrm{uvmem}}(31\mathrm{GHz})$ (Fig. 2.7a), as well as the normalized $\hat{j}_{\nu\,\mathrm{proxy}}$ map defined in Eq. 2.14 (Fig. 2.7b), along with its noise map (Fig. 2.7c). As explained in Section 2.2.2, the bulk of the free-free emission is located around HD 147889. Given this, we masked a region with a radius of 6 arcmin around HD 147889 in the `gpu-uvmem` maps, in order to quantify only the spinning dust component using $\hat{j}_{\nu\,\mathrm{proxy}}$. Note that the $\hat{j}_{\nu\,\mathrm{proxy}}$ map (Fig. 2.7b) shows variations throughout the region, with a peak that matches the peak at 31 GHz in the ρ Oph W PDR.

Table 2.8 lists $\hat{j}_{\nu\,\mathrm{proxy}}$ variations for different locations in the region. We see that the $\hat{j}_{\nu\,\mathrm{proxy}}$ map has a peak that is 25 times higher than the 3σ noise. We repeated this calculation on a `clean` $\hat{j}_{\nu\,\mathrm{proxy}}$ map and found an emissivity peak 10 times stronger than its 3σ noise. This difference is expected, as the `gpu-uvmem` map resolves much better the CBI 2 morphology. Interestingly, the emissivity variation between the $\hat{j}_{\nu\,\mathrm{proxy}}$ peak and the location of S1 is 22.8, very close to the strongest variation in ρ Oph W at 3σ. The fact that there is no significant 31 GHz emission originating at S1 (as seen in Figures 2.1 and 2.2) implies that the radio-emission mechanism is enhanced by the local conditions in the PDR, otherwise, we would see higher levels of 31 GHz emission near S1, given its large column of small grains (i.e. PAHs Casassus et al., 2008).

The nature of the spinning dust emissivity variations in ρ Oph may rely on various scenarios. Spinning dust models predict peak frequencies in the range 50-90 GHz for the typical environmental conditions of a PDR (e.g. Draine and Lazarian, 1998b; Ysard et al., 2011; Hensley and Draine, 2017b). However, only one reported observation of the California nebula is consistent with a spinning dust spectrum with a (50 ± 17) GHz peak (Planck Collaboration et al., 2014c). It is clear that the frequency of the spinning dust spectrum must be changing due to environmental conditions across the PDR. In this case, the observed emissivity variations could be associated with a shift in the peak frequency. Nevertheless, the analysis in

Table 2.8: Emissivities variations in ρ Oph measured with the $\hat{j}_{\nu\,\mathrm{proxy}}$ map.

Ratio	R
$\mathrm{S/N}_{\mathrm{Peak\,at\,}3\sigma}$ [a]	25.6
$\hat{j}_{\nu\mathrm{proxy-Peak}}$ / $\hat{j}_{\nu\mathrm{proxy-S1}}$ [b]	22.8 ± 5.2
$\hat{j}_{\nu\mathrm{proxy-Peak}}$ / $\hat{j}_{\nu\mathrm{proxy-SR3}}$ [c]	6.2 ± 0.3

[a] Ratio between the emissivity peak and its 3σ noise.
[b] Ratio between the peak and at the location of S1.
[c] Ratio between the peak and at the location of SR3.

this work is based on the assumption that the 31 GHz emission maps the AME.

A tentative explanation for the local emissivity boost, in the spinning dust paradigm, could be that the main spin-up mechanism in ρ Oph W are ion collisions (Draine and Lazarian, 1998a). The electromagnetic coupling between passing C^+ ions and the grain dipole moment impart torques on the grain. As the rotational excitation by ions is more effective for charged grains (Hensley and Draine, 2017b), a possible explanation could be that the PDR is hosting preferentially charged PAHs spun-up by C^+. As observed in Fig. 2.7, the fainter signal from S1 and SR3 in the radio maps of ρ Oph could then be naturally explained by the fact that these stars are too cold to create conspicuous CII regions (Casassus et al., 2008). In addition to the rotational excitation of charged grains, we could also add the effect of a possible changing penetration of the ISRF through the PDR due to the morphology of the cloud. The variations in the ISRF intensity affect the grain size distribution and, most likely, their dipole moment, and these factors can produce considerable changes in the spinning dust emissivity (Hoang et al., 2011). Thus, further analysis of the PDR spectrum at different radio-frequencies is required to calculate its physical parameters and understand the causes of the detected spinning dust emissivity variations.

2.3 Summary

The ρ Oph molecular cloud is one of the best examples of spinning dust emission, first detected by the CBI. Here we present 4.5 arcmin observations with CBI 2 that confirm 31 GHz emission from ρ Oph W, the PDR exposed to B-type star HD 147889, and highlight the absence of signal from S1, the brightest IR nebula in the complex. In order to quantify an association with dust-related emission mechanisms, we calculated correlations at different angular resolutions between the 31 GHz map and proxies for the column density of IR emitters, dust radiance and optical depth templates. We found that the 31 GHz emission correlates best with the PAH column density tracers, while the correlation with the dust radiance improves when considering emission that is more extended (from the shorter baselines), suggesting that the angular resolution of the observations affects the correlation results. A proxy for the spinning dust emissivity reveals large variations within the complex, with a dynamic range of 25 at 3σ and a variation by a factor of at least 23, at 3σ, between the peak in ρ Oph W and the location of S1, which means that environmental factors are responsible for boosting spinning dust emissivities locally.

Chapter 3

ALMA observations of polarized dust emission at pre-stellar core-scales

This work has been published in Arce-Tord et al. (2020a)

3.1 Magnetic fields in star-forming regions

It has been proposed that the magnetic field, pervasive in the ISM, might play an important role in the dynamical evolution of star-forming clouds (e.g. Shu et al., 1987; Hennebelle et al., 2011; Commerçon et al., 2011; Crutcher, 2012; Planck Collaboration et al., 2016a,b; Matsushita et al., 2018; Beuther et al., 2018). Large-scale observation ($\sim$1 pc) of the magnetic field revealed a well-ordered structure in the low-density envelopes of molecular clouds, suggesting that parsec-scale envelopes are magnetically supported against gravitational collapse (e.g. Franco et al., 2010). Besides their possible role in supporting clouds against gravity, magnetic fields may also strongly affect the formation and evolution of substructure within the clouds. Indeed the magnetic fields sometimes have a consistent morphology throughout scales, as reported by the TADPOL survey (Hull et al., 2014) that compared the orientation of the magnetic field at 20$''$ and 2.5$''$ in 30 low-mass star-forming regions distant of 125 to 2650 pc. At core scales ($\sim$ 0.1 pc), the magnetically-regulated core-collapse models presume a dominant role of the magnetic field (Shu et al., 1987; Shu et al., 2004; Galli and Shu, 1993a; Tomisaka, 1998; Allen et al., 2003a,b). These models are consistent with a handful of observations (e.g. Chapman et al., 2013; Qiu et al., 2014), but due to a small fraction of consistent data, the magnetically dominant core-collapse does not seem to be the predominant mode of low- or high-mass star formation (Hull and Zhang, 2019). At the circumstellar disk scales, $\sim$ 200 au, it is predicted that the magnetic fields have a perpendicular component to the disks, thus having a leading role for the triggering of outflows (Blandford and Payne, 1982; Camenzind, 1990; Konigl and Pudritz, 2000; Shu et al., 2000). No systematic relation, however, has yet been observed between the magnetic field direction and the outflow orientation when these are probed in the low-mass regime at $\sim$1000 au scales (Hull et al., 2013; Hull and Zhang, 2019). Nevertheless, one low-mass study toward 12 Class 0 protostars by Galametz et al. (2018) showed that at the envelope scale (600-1500 au) the magnetic field is

preferentially oriented either parallel or perpendicular to the direction of the outflows.

A few interferometric studies, such as, e.g. Girart et al. (2009); Beuther et al. (2010); Sridharan et al. (2014), have probed the high-mass star-forming regime. In particular, Zhang et al. (2014b) performed multi-scale observations of the magnetic field orientation in 14 high-mass star-forming regions. They showed that the magnetic field at core scales is either perpendicular or parallel to the magnetic field orientation at clump scales. Similar results were also reported by Koch et al. (2014) toward 50 star-forming regions, and by Ching et al. (2017) toward six massive dense cores located in DR21. One issue in determining the importance of magnetic fields for high-mass star formation is the lack of consistent analysis, in a large sample of sources, of the magnetic field morphology with respect to the density structure and gas dynamics. We collected all this information in the high-mass star-forming region (HMSFR) W43-MM1. W43-MM1, at a distance of 5.5 kpc from the Sun (Zhang et al., 2014a), has been reported as a mini-starburst cluster due to its high star formation rate of ∼6000 $M_\odot$/Myr (Louvet et al., 2014). W43-MM1 has been observed in polarized dust emission at 1.3 mm by Cortes and Crutcher (2006) with BIMA. They reported an ordered polarization pattern at ∼4.5″ angular resolution and derived an on-the-plane of the sky magnetic field strength of 1.7 mG. Later, Sridharan et al. (2014) observed W43-MM1 in polarized dust emission at 345 GHz and an angular resolution of ∼2.3″ with the SMA, and reported a pinched morphology of the magnetic field with a field strength of ∼6 mG. More recently, Cortes et al. (2016) conducted the first ALMA high-angular resolution map at 0.5″ of the magnetic fields in W43-MM1, performed using a single pointing, and also reported an organized magnetic field morphology with field strengths ranging from 0.2 to 9 mG.

3.2 Case of high-mass-SFR W43-MM1

This chapter presents observations of the polarized dust emission toward W43-MM1 in five pointings with the ALMA interferometer, to compare the orientation of the plane-of-the-sky magnetic field with the orientation of the cores and outflows identified in W43-MM1. Motte et al. (2018) reported that about 130 dense cores were forming stars in this region. From this sample of cores, 27 are driving 46 outflow lobes, whose orientations have been traced by Nony et al. (2020) using CO(2-1) and SiO(5-4) emission lines with ALMA. Here, we describe the observations, calibration and imaging of the data. We then calculate the angle differences among the magnetic field, the outflows orientations, and the position angle (PA) of the cores; and build their statistical distributions in the form of cumulative distribution functions (CDFs) that are further compared with synthetic populations of angle distributions.

3.2.1 Polarimetric observations

We present five pointings with ALMA in full polarization targeting the most massive dense cores in W43-MM1, previously identified by Louvet et al. (2014) based on IRAM/Plateau de Bure data. The ALMA observations were obtained between April and May 2016 using an array with 35 antennas, and used the standard frequency setup for continuum polarization in Band 6 (i.e. 4 spectral windows centred at 224.984, 226.984, 239.015, and 241.015 GHz).

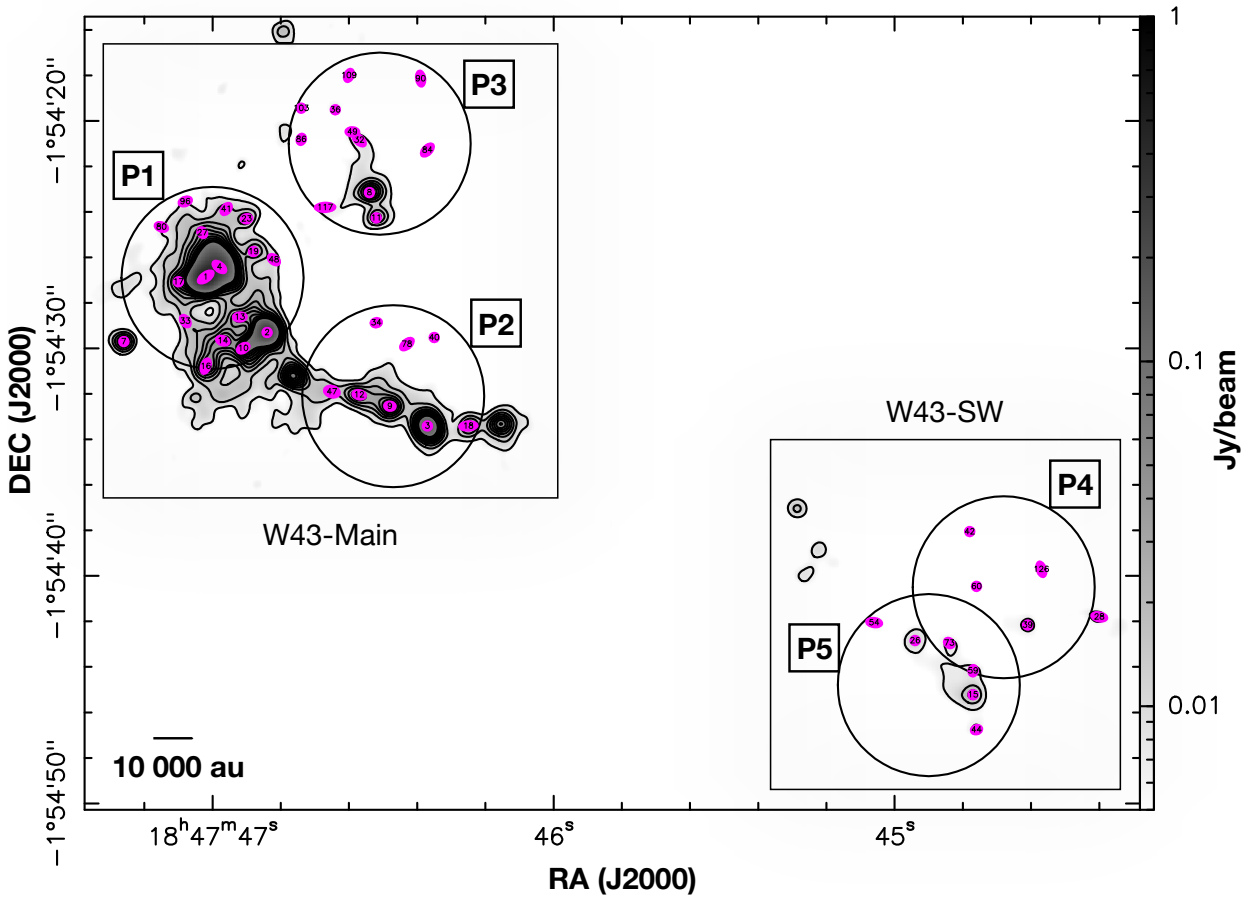

Figure 3.1: The map displays the continuum emission at 1.3 mm of the W43-MM1 HMSFR. Contours start at 3σ with steps of 3σ, where σ=2.4 mJy/beam. Black circles illustrate 1/3 of the primary beam for each of the 5 pointings, which are further presented in Figs. 3.2 and 3.3. The magenta ellipses indicate the cores presented by Motte et al. (2018).

Each spectral window has 64 channels of 31.250 MHz each, corresponding to a total bandwidth of 1.875 GHz per spectral window. The maximum recoverable scale is $\sim$10.6″. The resulting continuum images have an equivalent frequency of 233 GHz (or 1.3 mm) with an angular resolution of $0.55'' \times 0.49''$ (or $\sim$2700 au, considering the distance of the target). The calibration, the imaging, and the analysis were done using version 5.1.2. of the Common Astronomical Software Applications (CASA, McMullin et al. (2007)).

To improve the signal-to-noise ratio (SNR) of the images, we performed a phase self-calibration on each of the five calibrated data-sets. The images were improved iteratively through four rounds of phase-only self-calibration using the Stokes I image as a model. The final imaging was performed with the `tclean` task from CASA using a Hogbom deconvolver and a Briggs weighting scheme with a robust parameter of 0.5. The Stokes U and Q maps were imaged individually for each of the five fields with the `tclean` task using the same parameters as above. After the cleaning, a primary beam correction was applied to each map. Table 3.1 shows the coordinates for each pointing and the RMS noise level for each Stokes parameter. To provide an overview of the region, we present in Figure 3.1 a mosaic of

Table 3.1: Central coordinates in J2000 and noise values for each pointing. We also show the noise values of the linear polarization maps ($\sigma_{\rm P}$), that we used to define the $3\sigma_{\rm P}$ and $5\sigma_{\rm P}$ thresholds to plot the polarization vectors for the individual pointings. Since we did not analyze the polarized emission in the mosaic, we only present its Stokes I noise level. The noise values are in units of mJy/beam.

Pointing	RA	Dec	$\sigma_{\rm I}$	$\sigma_{\rm Q}$	$\sigma_{\rm U}$	$\sigma_{\rm P}$
1	18:47:47.00	-1:54:26.90	3.42	0.12	0.11	0.12
2	18:47:46.47	-1:54:32.10	2.51	0.11	0.10	0.11
3	18:47:46.51	-1:54:21.00	2.37	0.12	0.11	0.11
4	18:47:44.68	-1:54:40.50	0.47	0.04	0.05	0.05
5	18:47:44.90	-1:54:44.80	0.50	0.05	0.05	0.05
Mosaic	-	-	2.39	-	-	

the Stokes I image[1].

The magnetic field maps were computed using the Stokes Q and U intensity maps for each pointing. For this, we created the linear polarized intensity map, $P = \sqrt{Q^2 + U^2}$. However, even when the Stokes Q and U maps could have negative values, P will always be positive. In order to correct for this, we applied the debiasing method proposed by Vaillancourt (2006), which employs a Bayesian approach instead of the classical frequentist method, and gives a better estimation of the polarized emission for low signal-to-noise measurements, $\lesssim 3\sigma_{\rm P}$, where $\sigma_{\rm P}$ is the RMS noise level in the polarization maps. We wielded the $3\sigma_{\rm P}$ debiased intensity value as a threshold to select the pixels used to derive the polarization angle maps, computed as $\chi = 0.5 \arctan(U/Q)$. Finally, we assumed alignment of the grains with respect to the magnetic field due to the 'Radiative Alignment Torques' mechanism (RATs), through which external radiation field causes the dust grain to spin-up, contributing to an efficient alignment between its angular momentum and the magnetic field line (Lazarian, 2007; Hoang and Lazarian, 2009; Andersson et al., 2015). As a consequence, the aligned grains will emit thermal radiation that is polarized perpendicular to the magnetic field, letting us infer the magnetic field morphology onto the plane of the sky by rotating the polarization angle by 90°.

3.2.2 Outflows, cores and magnetic field orientations

Figure 3.1 shows the 1.3 mm continuum emission of W43-MM1, which hosts two clusters of protostars separated by ∼0.9 pc: the Main region (pointings 1, 2, and 3) and the South-West (SW) region (pointings 4 and 5). The continuum emission shown here recovers an ordered magnetic field in the Main region, very similar to that previously presented by Cortes et al. (2016) and Motte et al. (2018). The latter identified 131 cores in the two clusters. Those falling within the one-third area of the primary beams of the five pointings are superposed over Fig. 3.1. Figures 3.2 and 3.3 display the morphology of the magnetic field in each of the 5 pointings, which were imaged independently. In the Main region, the large-scale magnetic field (∼1 pc) shows a smooth and ordered morphology. In the SW region, the information

[1]The mosaic was produced with data that were not self-calibrated.

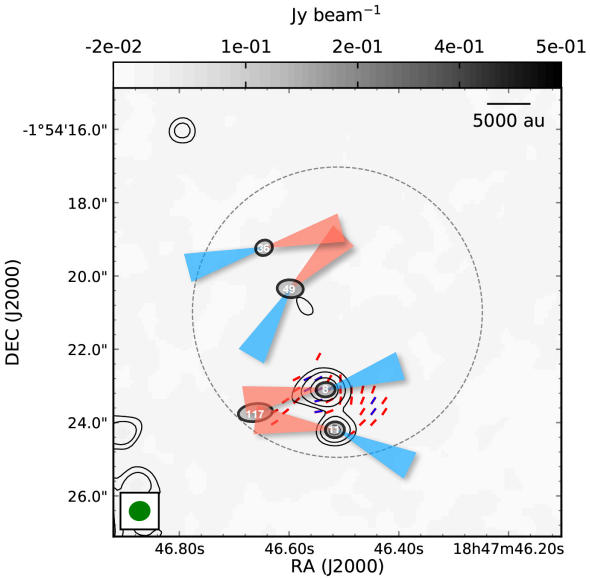

(a) Pointing 3

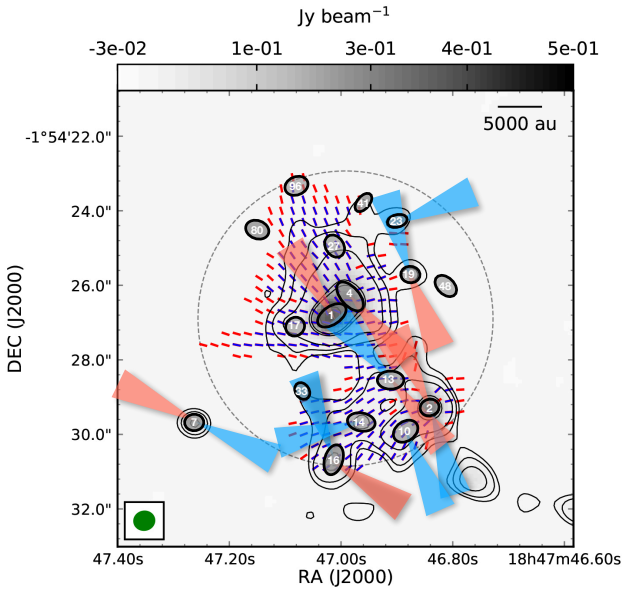

(b) Pointing 1

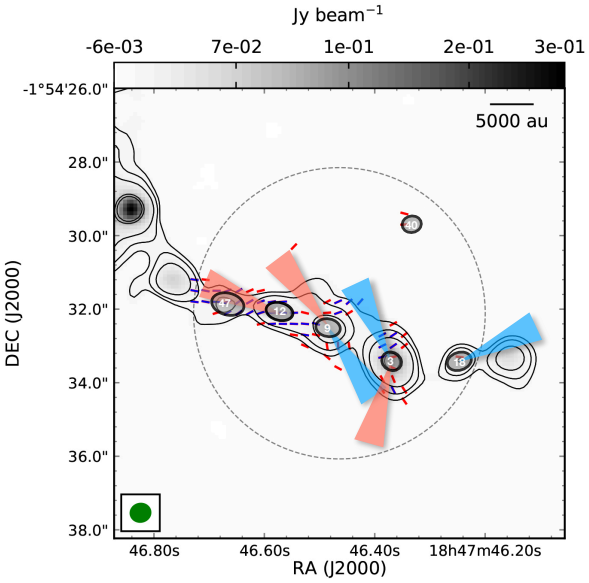

(c) Pointing 2

Figure 3.2: Dust polarization semi-vectors (rotated by 90° to show the inferred magnetic field orientation) over the continuum emission at 1.3 mm for pointings 1, 2 and 3 toward W43-MM1. Continuum contours levels are at 3, 5, 10, 50, and 100 $\sigma_{\rm I}$ ($\sigma_{\rm I}$ levels in Table 3.1). The semi vectors in red and blue show the magnetic field orientation where the polarized intensity exceeds a noise level of $3\sigma_{\rm P}$ and $5\sigma_{\rm P}$, respectively; see Table 3.1. The semi-vectors are plotted every 3 pixels, which correspond to a Nyquist spatial frequency of four vectors per synthesized beam (two in each dimension). The red and blue cones represent the red-shifted and blue-shifted outflow lobes, respectively. Circles in dashed grey represent 1/3 of the $\sim 24''$ primary beam, within which we performed the analysis. The solid green ellipse shows the synthesized beam of $0.55'' \times 0.49''$, PA = -79.4°.

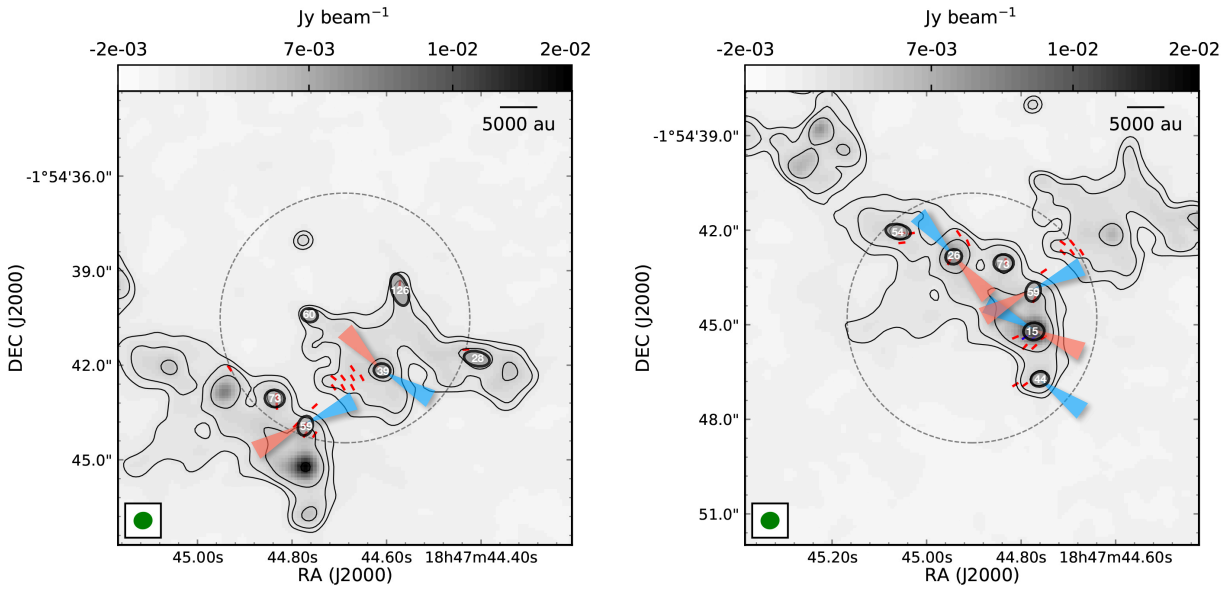

(a) Pointing 4

(b) Pointing 5

Figure 3.3: Following Fig. 3.2: Dust polarization semi-vectors (rotated by 90° to show the inferred magnetic field orientation) over the continuum emission at 1.3 mm for pointings 4 and 5. Continuum contours levels are at 3, 5, 10, 40 $\sigma_{\rm I}$ for ($\sigma_{\rm I}$ levels in Table 3.1).

about the magnetic field orientation is coarser: there are only eight independent locations where the magnetic field orientation could be derived. Linking the large-scale morphology of the magnetic field to its small-scale features goes beyond the scope of this work, and is the subject of a forthcoming publication (Louvet et al. in prep).

We measured the position angle (PA) of the magnetic field at the location of the cores identified by Motte et al. (2018). To ensure reliable linear polarization measurements, and following ALMA recommendations, we restrained this analysis to within one-third of the primary beam for each pointing. In total, 52 cores out of the 130 cores of Motte et al. (2018) fall into these trusted areas. Of these 52 cores, 29 display polarized thermal dust emission. We computed the magnetic field orientation for each core as $BF = 0.5 \arctan(U/Q) + \pi/2$ (see Sect. 3.2.1), where Q and U are the mean Stokes Q and U intensities averaged within each core, whose area is defined by a 2D Gaussian fit of its Stokes I emission. The polarization angle uncertainties were estimated through error propagation as $\sigma_\chi = 0.5 \times (\sigma_P/P)$, where P is the mean polarized intensity within the corresponding core and $\sigma_{\rm P} = \sqrt{(< Q > \times \sigma_{\rm Q})^2 + (< U > \times \sigma_{\rm U})^2}/P$ is the RMS of the linearly polarized emission.

We compare the magnetic field orientation at the scale of the cores with archival data that provide the orientation of the outflows driven by the cores (Nony et al., 2020), and the PA of the major axis of the cores (Motte et al., 2018). The absolute values of these three sets of angle orientation, together with the relative orientations among the magnetic field lines at the location of the cores, the outflow orientations, and the PA of the cores are presented in Table 3.3. These differences are represented in the form of CDFs and compared with Monte Carlo simulations to see whether there is a favored orientation. These simulations select 100,000 pairs of random 3D vectors with an angle difference within a

given range. These vectors are then projected onto the plane of the sky to measure their apparent angle difference. We considered the following five ranges of 3D angle differences: $0° - 20°$ (parallel); $20° - 50°$; $50° - 70°$; $70° - 90°$ (perpendicular), and $0° - 90°$(random). To further investigate the distributions' tendencies, we performed Kolmogorov-Smirnov (KS) tests between the observed and the simulated populations. The KS-test is a non-parametric test that quantitatively evaluates the difference between the cumulative distributions of two data sets. We chose the KS-test over the *chi-squared* test as the former is preferable to compare non-equally sampled data. Thus, we computed the p-value (p) that evaluates if the data and a given synthetic population are drawn from the same parent distribution, with low values of p corresponding to different populations. Following a conservative rule of thumb, we rejected the hypothesis that the two populations are drawn from the same distribution when $p < 0.05$.

3.2.3 Orientation between the magnetic field and the cores major axes

We compared the PA of the 29 cores falling within the one-third region of the primary beams of the five pointings with the mean PA of the magnetic field inside the cores. The CDF of these angle differences is presented in Fig. 3.4, together with the CDFs arising from the five different synthetic angle simulations. The CDF of the data clearly shows that the orientation of the cores with respect to the magnetic field orientation is only reproduced by the 20-50° population. The results of the KS-tests, which compare the observations with the synthetic populations, are reported in Table 3.2. Here, we confirm that the magnetic field orientation with respect to the cores PA in the data is not random: all the synthetic populations (including the random distribution) except for the 20-50° distribution are rejected by the KS test.

In the so-called magnetically regulated core-collapse models (e.g. Galli and Shu, 1993a,b; Allen et al., 2003a,b) magnetic fields are dynamically important and dominate the dynamics of the core-collapse by deflecting the infalling gas toward the equatorial plane to form a flattened structure, known as pseudodisk, around the central protostar. The pseudodisks are not supported by rotation, but by magnetic pressure, and they develop orthogonally to the magnetic field direction. They have sizes of a few thousands of au, on the order of the angular scales probed in this thesis. Therefore, if magnetically regulated core-collapse were at work, one would expect to observe flattened central regions – the pseudodisks – (generically called cores in this thesis), oriented perpendicular to the magnetic field lines. The very few existing observational studies, that did report such behavior, had very limited samples: Davidson et al. (2011) studied 350 µm polarization observations taken at the CSO toward three low-mass Class 0 protostars, and reported a magnetic field orientation in loose agreement with the magnetically-controlled core-collapse predictions; Chapman et al. (2013) found the magnetic field orientation to be perpendicular to the pseudodisks in four low-mass cores, using 350 µm polarization observations taken at the CSO; Qiu et al. (2014) reported a similar result toward the G240.31+0.07 high-mass core using the SMA at 0.88 mm. In contrast, the results presented in this thesis, obtained with a sample of 29 cores, are not consistent with the prediction of the magnetically-regulated core-collapse models. Instead,

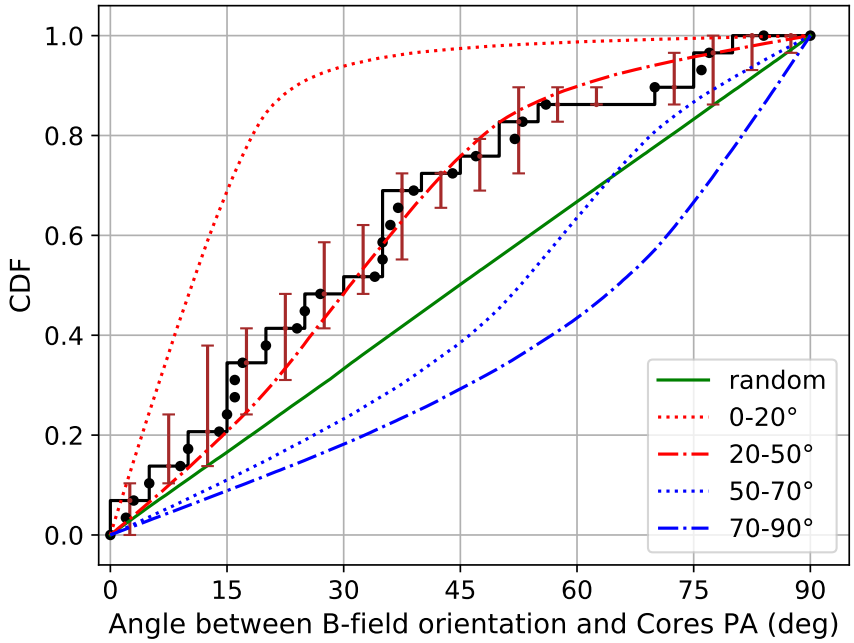

Figure 3.4: Cumulative distribution function (CDF, black points) of the angle difference between the magnetic field orientation and the PA of the cores in W43-MM1. The black histogram shows the CDF with 5° bin-widths. The brown bars show the errors on the CDF for each bin. Curves in color are the CDFs resulting from Monte Carlo simulations of different 3D angles projected onto the plane of the sky. The different intervals of angles considered for the synthetic populations are indicated on the bottom right of the plots.

as shown in Fig. 3.4, the major axes of the cores are not preferentially oriented orthogonal to the magnetic field, but rather tend to be oriented 20-50° with respect to the field. Having a non-random orientation of the cores with respect to the magnetic field orientation suggests that the magnetic field and the dense material are well coupled.

3.2.4 Orientation between the magnetic field and the outflows axes

Nony et al. (2020) studied the outflows associated with the cores of W43-MM1 by observing the ^{12}CO(2-1) and the SiO(5-4) molecular emission lines with an ALMA plus ACA mosaic at an angular resolution of $\sim$0.45″ (similar to that of the present study). In total, they reported 46 individual outflow lobes associated with 27 cores. On one hand, about one-fourth of these outflows are monopolar. They could be truly monopolar, as observed in some nearby objects (e.g. HH30, Louvet et al., 2018), or the emission arising from the companion outflow could be absorbed by the surrounding medium. On the other hand, most of the bipolar outflows are not straight, meaning that there is a shift between the PA of the red-shifted lobe with respect to the PA of the blue-shifted lobe (see Figs. 3.2 and 3.3). This could be due to sub-fragmentation within the cores and/or deflection of the outflows. For this reason, we will consider each outflow lobe independently[2]. Eighteen of the 27 cores that have one or more outflows are detected in polarization. In Table 3.3, we report the orientation of the outflows

[2]We also performed the analysis treating bipolar outflows as single data points and obtained similar results

associated with these 18 cores. The orientation of one outflow is defined as the angle of the line linking the core location (defined as the continuum peak) and the furthest knot of the outflow (see Nony et al. (2020) for more details about the outflow characteristics).

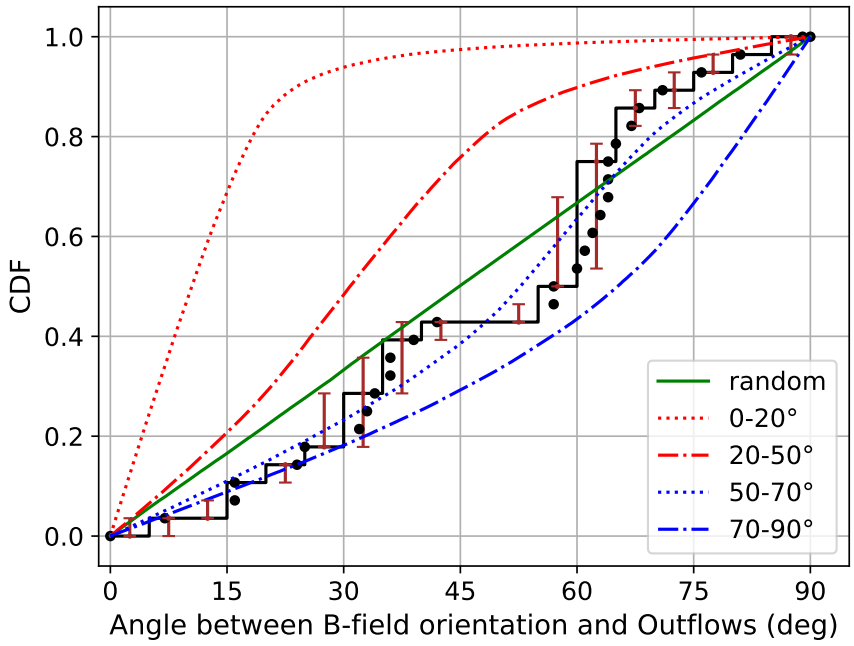

Figure 3.5: Cumulative distribution function (CDF, black points) of the angle difference between the magnetic field orientation and the PA of the outflows in W43-MM1. The black histogram shows the CDF with 5° bin-widths. The brown bars show the errors on the CDF for each bin. Curves in color are the CDFs resulting from Monte Carlo simulations of different 3D angles projected onto the plane of the sky. The different intervals of angles considered for the synthetic populations are indicated on the bottom right of the plots.

One common feature of the two families of models explaining the presence of outflows – the disk-wind models (see, e.g. Ferreira, 1997) and the entrainment models (see, e.g. Blandford and Payne, 1982) – is that they both need the circumstellar disk to be orthogonal to the magnetic field lines, causing the ejection of matter along the magnetic field lines. Hence, if the models are valid, one expects to see alignment between the outflows and the magnetic field near the disks. Carrasco-González et al. (2010) first found an alignment between the outflow-lobe associated to the massive YSO HH 80/81 and the magnetic field in its jet, inferred from polarized synchrotron emission measured with the VLA, up to ∼0.5 pc from the driving source. Beuther et al. (2010) studied the high-mass disk-outflow system IRAS18089-1732 and found that the magnetic field, measured from CO(3-2) polarized emission, is aligned with the outflow orientation from small core scales (∼7000 au) to larger outflow scales of ∼36000 au. Sridharan et al. (2014) also reported alignment between the magnetic field, measured from dust polarized emission, and one outflow in W43-MM1 using SMA observations at an angular resolution of ∼3″. However, this interpretation was disproved by a more recent study using ALMA at ∼0.5″, which revealed that the outflow seen with the SMA toward W34-MM1 was the sum of 12 outflow lobes with different orientations (Nony et al., 2020). Also, Zhang et al.

like the ones presented in Sect. 3.2.4 and Sect. 3.2.5.

(2014b) studied a sample of 14 clumps located in different regions where they could compare the orientation of the magnetic field lines with respect to the axes of the outflows. While they refrained from interpreting the detailed structure of the obtained distribution, they reported no strong correlation between the outflow and the magnetic field orientations. The lack of alignment between outflows and the magnetic field is also observed in low-mass star-forming regions at ∼1000 au scale (see the recent review by Hull and Zhang (2019)). At the envelope scale (∼600-1500 au), Galametz et al. (2018) reported that the magnetic field is preferentially observed either aligned or perpendicular to the outflow direction when studying a sample of 12 Class 0 envelopes in nearby clouds. They interpret this bi-modality by considering that the cases that showed an alignment between the magnetic field and the rotation axis might be the result of a strong magnetic field. They also attribute this bi-modality to the fact that most of the cores with a magnetic field perpendicular to the outflows are binaries.

The CDF of the orientation differences between the magnetic field and the outflows is presented in Fig. 3.5. In Table 3.2 we show the results of the KS-tests, which compare the observations with the synthetic populations. Based on these tests, we can reject the hypothesis that the outflows are oriented parallel or perpendicular to the magnetic field. Instead, the KS-tests favor either a random orientation of the outflows with respect to the magnetic field lines or that the outflows are oriented 50-70° with respect to the magnetic field lines. These two configurations can be explained by two main scenarios:

(i) The outflows could be randomly oriented to the magnetic field lines, in line with the observations toward low-mass star-forming regions (Hull and Zhang, 2019). Assuming that the models for outflow launching are accurate, where gas from the accretion disk should be ejected along magnetic field lines, this finding would imply that most of these (high-mass) proto-stars form in an environment where the magnetic field is too weak to maintain a consistent orientation from the ∼2700 au scales that we are probing, down to the 0.1-10 au scales where outflows are launched (Louvet et al., 2018). It would also imply that the orientation of the disks is not controlled by the magnetic field, but by another mechanism provoking angular momentum redistribution such as interactions in multiple systems, or randomization of the disk orientation by accretion during the early phases of protostellar evolution (Lee et al., 2017).

(ii) The outflows could be oriented 50-70° to the magnetic field lines. It is striking to note that if the elongation of the cores correspond to the major axes of the underlying disks, and considering that outflows propagate orthogonally to their hosting disk, a population of cores being oriented 20-50°, as reported in the previous independent correlation, would translate into a population of outflows oriented 40-70° with respect to the magnetic field lines, in excellent agreement with the outflow being preferentially oriented 50-70° to the magnetic field. Nevertheless, there is a better match of the CDF presenting the 20-50° angle differences between the PA of the cores and the magnetic field orientations than the CFD presenting the 50-70° angle differences between the outflow orientations and the magnetic field. Such a loss of statistical significance is expected if, in some cores, the magnetic field is not strong enough to govern the angular momentum from the core scale down to the outflow ejection location at 0.1-10 au.

3.2.5 Orientation between the outflows and the cores

The comparison between the PA of the outflows and the PA of the cores is presented in the CDF in Fig. 3.6. Based on visual inspection, the observational CDF seems to be consistent with the random synthetic population, suggesting that there is no specific orientation of the outflows with respect to the elongation of the cores. However, when comparing the observations with the synthetic populations through the KS tests, while the random population obtains the highest statistical weight with p ∼0.5, the 50-70° population cannot be discarded (p∼0.2).

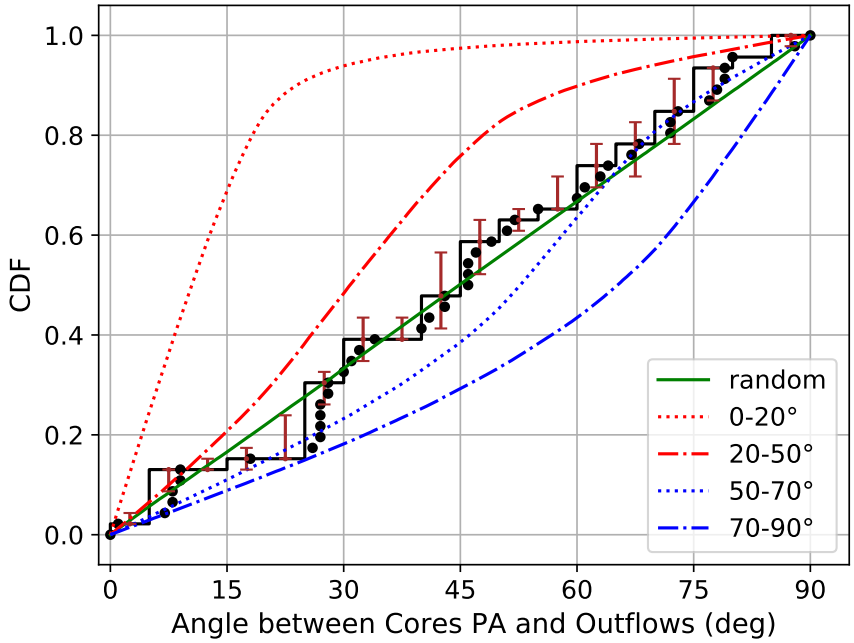

Figure 3.6: Cumulative distribution function (CDF, black points) of the angle difference between the outflows and the PA of the cores in W43-MM1. The black histogram shows the CDF with 5° bin-widths. The brown bars show the errors on the CDF for each bin. Curves in color are the CDFs resulting from Monte Carlo simulations of different 3D angles projected onto the plane of the sky. The different intervals of angles considered for the synthetic populations are indicated on the bottom right of the plots.

These two possibilities result in the following interpretations:

(i) Random orientation of the outflows with respect to their hosting cores: recent studies of protostellar objects forming low-mass stars have shown that outflows are usually observed perpendicular to their underlying disks at small scales (<200 au, see e.g. Louvet et al., 2016). Building on the hypothesis that this also happens for high-mass proto-stars, there are two ways of interpreting this result. If the core elongations are representative of the major axes of underlying disks, the random orientation of the outflows to the cores would indicate that the outflows get randomly deflected at scales below our angular resolution (∼2700 au). Such deflections have been observed in a few outflows in W43-MM1 at a larger scale by Nony et al. (2020) and, therefore, could also occur below our resolution. Nevertheless, it is reasonable to argue that a deflection is more likely to occur with a small angle and that the statistical

Table 3.2: Kolmogorov-Smirnov tests for the observed and simulated angle distributions.

Test case	Synthetic population	KS p-value	Sample size
B-field vs. Cores PA	0-20°	7×10^{-8}	29
	20-50°	0.76	
	50-70°	6×10^{-3}	
	70-90°	6×10^{-6}	
	Random	4×10^{-2}	
B-field vs. Outflows	0-20°	2×10^{-100}	28
	20-50°	8×10^{-6}	
	50-70°	0.51	
	70-90°	1×10^{-2}	
	Random	0.16	
Cores PA vs. Outflows	0-20°	1×10^{-15}	46
	20-50°	1×10^{-3}	
	50-70°	0.16	
	70-90°	1×10^{-3}	
	Random	0.53	

impact of deflections should be minimal. Therefore, deflections are unlikely to result in a random orientation of the outflows with respect to their hosting cores. If outflows are indeed randomly oriented with respect to the core PA, a more likely explanation is that the elongation of the cores is not representative of the PA of underlying disks.

(ii) Outflows oriented 50-70° to their hosting cores: such a configuration does not match any expectations from the models of launching and/or propagation of outflows. In order to come up with a more physical explanation, we tested bi-modal synthetic populations. The fiducial synthetic distributions of angles originally presented only contain single populations, meaning (e.g.) that in the "50°-70°" distribution all the angle differences are between 50° and 70° in the 3D space. Instead, the bi-modal synthetic populations have a percentage $n_{\%}$ of 3D vector pairs with angle differences within a certain angle range and the complementary fraction of vector pairs, $1 - n_{\%}$, within another angle range. A good correlation was found between the observations with a bi-modal population where 85% of the outflows are randomly oriented and 15% are orthogonally oriented to their respective core, in line with the original assumption. However, given the size of the sample, it is statistically not possible to discriminate between the 50-70°, a random, or an 85% random plus 15% orthogonal populations.

3.3 Summary

Polarimetric observations have suggested that the ISM magnetic field plays an important role in the process of massive star formation. To better understand the impact of the magnetic field at the pre and proto-stellar stages, high-angular resolution observations of polarized dust emission toward a large sample of massive dense cores are needed. This work aims at revealing any correlation between the magnetic field orientation and the orientation of the cores and outflows in a sample of protostellar dense cores in the W43-MM1 high-mass

star-forming region. We used Band 6 (1.3 mm) ALMA observations in full polarization mode to map the polarized emission from dust grains at a physical scale of ∼2700 au. With these data, we measured the orientation of the magnetic field at the core scale, and examined the relative orientations of the core-scale magnetic field, of the protostellar outflows, and of the major axis of the dense cores determined from 2D Gaussian fit in the continuum emission.

The results suggests that orientation of the dense cores is not random with respect to the magnetic field. Instead, the dense cores are compatible with being oriented 20-50° with respect to the magnetic field. As for the outflows, they could be oriented 50-70° with respect to the magnetic field, or randomly oriented with respect to the magnetic field, similar to current results in low-mass star-forming regions. The observed alignment of the position angle of the cores with respect to the magnetic field lines shows that the magnetic field is well coupled with the dense material; however, the 20-50° preferential orientation contradicts the predictions of the magnetically-controlled core-collapse models. The potential correlation of the outflow directions with respect to the magnetic field suggests that, in some cases, the magnetic field is strong enough to control the angular momentum distribution from the core scale down to the inner part of the circumstellar disks where outflows are triggered.

Table 3.3: PA_{core} is the cores (major axis) position angle. θ_{blue} and θ_{red} are the blue and red-shifted outflow position angles, respectively. BF is the magnetic field orientation at the location of the cores. The five last columns show the angle differences between the orientations given in column two, three, four, and five.

Core	$PA_{core}^{1,2,3}$	θ_{red}^{1}	θ_{blue}^{1}	$BF^{1,4}$	$\lvert BF - PA_{core}\rvert^{5}$	$\lvert BF - \theta_{red}\rvert^{5}$	$\lvert BF - \theta_{blue}\rvert^{5}$	$\lvert PA_{core} - \theta_{red}\rvert^{5}$	$\lvert PA_{core} - \theta_{blue}\rvert^{5}$
1	-56 ± 4	32 ± 0.5		71 ± 4	53 ± 4	39 ± 3		88 ± 3	
2	-75 ± 8	25 ± 0.9	-165 ± 0.8	-66 ± 4	9 ± 6	89 ± 3	81 ± 3	80 ± 6	90 ± 6
3	57 ± 6	164 ± 0.9	25 ± 0.5	-84 ± 8	39 ± 7	68 ± 6	71 ± 6	73 ± 4	32 ± 4
4	41 ± 6	-140 ± 1		-83 ± 2	56 ± 4	57 ± 2		1 ± 4	
7	-88 ± 8	64 ± 1	-115 ± 0.5					28 ± 6	27 ± 6
8	-90 ± 9	99 ± 2	-72 ± 3.0	-65 ± 4	25 ± 7	16 ± 3	7 ± 4	9 ± 7	18 ± 7
9	80 ± 11	37 ± 0.5	-146 ± 1.0	70 ± 7	10 ± 9	33 ± 5	36 ± 5	43 ± 8	46 ± 8
10	-54 ± 12		-156 ± 0.5	-40 ± 3	14 ± 9		64 ± 2		78 ± 8
11	-89 ± 13	83 ± 4	-116 ± 0.5	-55 ± 9	34 ± 11	42 ± 7	61 ± 6	8 ± 10	27 ± 9
12	76 ± 9	68 ± 0.5		-88 ± 3	16 ± 7	24 ± 2		8 ± 6	
13	-87 ± 31	-142 ± 3	41 ± 4.0	-82 ± 2	5 ± 21	60 ± 3	57 ± 3	55 ± 21	52 ± 22
14	73 ± 31		104 ± 0.5	-60 ± 2	47 ± 21		16 ± 1		31 ± 21
15	-88 ± 12	-115 ± 0.5	62 ± 2.0	-53 ± 6	35 ± 9	62 ± 4	65 ± 4	27 ± 8	30 ± 9
16	-20 ± 12	-123 ± 1	20 ± 0.5	-56 ± 2	36 ± 9	67 ± 2	76 ± 1	77 ± 8	40 ± 8
17	72 ± 34			74 ± 3	2 ± 23				
18	-72 ± 5		-65 ± 0.5	81 ± 8	27 ± 7		34 ± 6		7 ± 4
19	85 ± 17	-158 ± 1	17 ± 4.0					63 ± 12	68 ± 12
22a	-84 ± 23	69 ± 2	-125 ± 0.5					27 ± 16	41 ± 16
22b	-84 ± 23	142 ± 0.5						46 ± 16	
23	-77 ± 25		-68 ± 1.0	87 ± 7	16 ± 18		25 ± 5		9 ± 17
26	-67 ± 16	-139 ± 0.5	41 ± 0.5	-23 ± 8	44 ± 13	64 ± 6	64 ± 6	72 ± 11	72 ± 11
27	72 ± 41			37 ± 2	35 ± 28				
28	65 ± 11			89 ± 8	24 ± 10				
29	-58 ± 17		-12 ± 1.0						46 ± 12
31	40 ± 22	101 ± 1	-73 ± 1.0					61 ± 15	67 ± 15
33	33 ± 24			-70 ± 9	77 ± 18				
36	26 ± 16	-75 ± 0.6	105 ± 2.0					79 ± 11	79 ± 11
39	86 ± 27	43 ± 4	-120 ± 0.9					43 ± 19	26 ± 19
40	-79 ± 23			84 ± 7	17 ± 17				
41	-40 ± 32			12 ± 7	52 ± 23				
44	-66 ± 19		-126 ± 0.5	-63 ± 9	3 ± 15		63 ± 6		60 ± 13
47	-96 ± 30			-59 ± 3	37 ± 21				
48	46 ± 26								
49	86 ± 17	-45 ± 0.5	150 ± 0.5					49 ± 12	64 ± 12
54	81 ± 12			-79 ± 7	20 ± 10				
59	-14 ± 33	119 ± 0.5	-65 ± 0.5	-29 ± 9	15 ± 24	32 ± 6	36 ± 6	47 ± 23	51 ± 23
60	81 ± 28								
67	40 ± 16	12 ± 1.5	-174 ± 0.5					28 ± 11	34 ± 11
73	81 ± 25			11 ± 8	70 ± 18				
80	70 ± 23								
96	-62 ± 21			14 ± 5	76 ± 15				
117	-83 ± 12								
126	-81 ± 14			3 ± 8	84 ± 11				

[1] All the angles are measured counterclockwise from north.

[2] The PAs (major axis) come from the GETSOURCES catalogue and complete Table 1 of Motte et al. (2018).

[3] To account for the ellipticity of cores, the error of the PA is computed as $180° \times (1-e) \times (\ln[F_{core}/\sigma_f])^{-2}$ where e is the ellipticity of the core, σ_f the uncertainty on the flux measurement, and F_{core} the integrated flux of the core (S. Mensh'chikov, private communication).

[4] The magnetic field PA indicates the mean magnetic field orientation inside the cores (see Sect. 3.2.2 for details).

[5] The uncertainty for the angle difference (col. 6, 7, 8, 9, and 10) is $\sigma = \arctan\left(\sqrt{\frac{\sin\delta^2 + \sin\phi^2}{\cos\delta^2 + \cos\phi^2}}\right)$, where δ and ϕ correspond to the errors associated with the measurement uncertainties (col. 2, 3, 4, and 5).

Chapter 4

Dust continuum observations of transition disks at au-scales

This work has been published in Arce-Tord et al. (2023).

4.1 Warps in transition disks

Transition disks (Espaillat et al., 2010) are useful sources for the study of circumstellar disk warps. This is due to their characteristic inner dust cavity, which may have been cleared by the orbit of young planets (e.g. Dong et al., 2015). Resolved observations in scattered light have revealed azimuthal dips along the outer rings. For instance, infrared (IR) and optical scattered light observations in HD 142527 (Fukagawa et al., 2006; Casassus et al., 2012; Avenhaus et al., 2014) revealed dips in the outer disk thought to be shadows due to a central warp (Marino et al., 2015). The shadows in this disk, seen in polarized-differential imaging (PDI), are explained by a tilted inner disk, 70° relative to the outer disk.

Analysis of gas kinematics traced by ALMA observations of HD 142527 in CO(6−5) showed that the intra-cavity gas is close to free-fall through the central warp (Casassus et al., 2015a). This warped structure is most likely caused by the inclined orbit of the low mass companion HD 142527B (Biller et al., 2012; Price et al., 2018), which translates into shadows deep enough to cool the dust in the outer ring and cause the local decrements in the ALMA continuum (Casassus et al., 2015b).

Observations with the Spectro Polarimetric High-contrast Exoplanet REsearch (SPHERE; Beuzit et al., 2019) instrument at the Very Large Telescope (VLT) have confirmed and revealed more detailed information on the azimuthal dips in TDs. For instance, another example of a warp related to a tilted inner disk is HD 100453. Benisty et al. (2017) observed polarized scattered light using VLT/SPHERE at optical and near-IR wavelengths, and found azimuthal dips interpreted as narrow shadows by Min et al. (2017). However, scattered light observations of shadowed outer rings often do not have radio counterparts. This is the case for HD 100453 (van der Plas et al., 2019), and also for warped disk HD 143006 (Pérez et al.,

2018), both of which show shadows in SPHERE polarized intensity with no radio counterparts in ALMA Band 6. The absence of radio decrements under the shadows may be due to disk thermal radiation, which if optically thin [1], can smooth out the temperature decrement (Casassus et al., 2019b). Thus, for a fixed dust population, such temperature decrements would be more conspicuous in massive disks.

4.2 Case study of T-Tauri DoAr 44

An example of smoothed radio decrements due to radiative diffusion can be observed in DoAr 44. DoAr 44 (also known as WSB 72, HBC 268 or ROXs 44) is a T-Tauri young stellar object (YSO) located in the L1689 region of the Ophiuchus dark cloud (Padgett et al., 2008; Andrews et al., 2011) at a distance of 145.9 ± 1.0 pc (Gaia Collaboration et al., 2018). It is catalogued as a pre-transition disk (PTD) as represented by its spectral energy distribution (SED) in Cieza et al. (2021), with a SED slope $\alpha_{\rm IR} >= -0.61$. Here, PTDs are defined as Class II sources ($-0.3 > \alpha_{\rm IR} > -1.6$) with an IR bright inner disk and a mid-IR SED decrement that indicates the existence of a gap. Also, DoAr 44 is included in the multiplicity survey by Zurlo et al. (2020), but no companion was detected.

Previous works on DoAr 44, using SMA (Submillimeter Array) 340 GHz continuum observations at an angular resolution of 0.3 arcsecond (Andrews et al., 2009; Andrews et al., 2011) and ALMA 335 GHz continuum with spectral observations (van der Marel et al., 2016) have detected a moderate ~ 30 au cavity in the disk. Casassus et al. (2018, hereafter, paper I) proposed a warped geometry inside the cavity by studying azimuthal decrements using ALMA 336 GHz continuum observations, complemented with SPHERE/IRDIS (Infrared Dual-band Imager and Spectrograph) differential polarized imaging (DPI) and radiative transfer (RT) parametric models. A comparison with RT predictions suggests that the inner disk is tilted by $\xi \sim 30$ deg relative to the plane of the outer disk. However, the IRDIS data are affected by the coronograph, which borders the edge of the cavity. Paper I used aggressive deconvolution in order to improve the resolution of the ALMA data available at the time for their analysis, which suggested the presence of a radio dip associated to the northern shadow.

This chapter reports new short and long-baseline (SB+LB) ALMA observations and a 3-year time difference follow-up SPHERE/IRDIS VLT observations of DoAr 44. We aimed to analyze the variability of the shadows generated by the warped inner disk over the outer disk, using multi-epoch ALMA Band 6 and Band 7 data and comparing follow-up SPHERE polarized intensity observations to the previous published epoch.

[1] In the Planck or Rosseland sense.

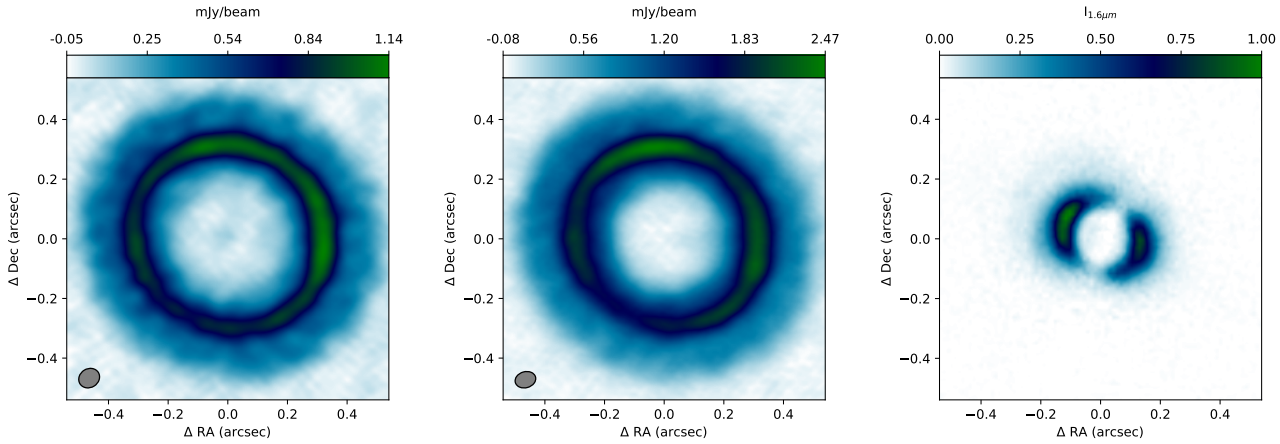

(a) (b) (c)

Figure 4.1: 4.1a: 230 GHz continuum restored image. The grey ellipse shows the synthesized beam (72.4 mas × 62.7 mas for Briggs 1.0). 4.1b: the 350 GHz continuum restored image. The grey ellipse shows the synthesized beam (70.2 mas × 53.8 mas for Briggs 1.0). 4.1c: H-band polarized intensity image, $Q_\phi(H)$.

4.2.1 Observations and data reduction

ALMA observations

The Ophiuchus DIsc Survey Employing ALMA (ODISEA, Cieza et al., 2019) LB survey was carried out during ALMA Cycle 6 in Band 6 (230 GHz), reaching resolutions of ∼3-5 au (PID = 2018.1.00028.S). The aim of this survey is to study the dust and gas components of a flux-limited population of disks, in a wide range of evolutionary stages, located in the Ophiuchus star-forming region at a distance of ∼ 200 pc (Evans et al., 2009; Williams et al., 2019). These Band 6 continuum observations of DoAr 44 (bandwidth of 7.5 GHz) were acquired in two epochs during July of 2019, and the data were calibrated using the ALMA Calibration Pipeline in CASA (see Cieza et al., 2021, for details). The continuum Band 7 observations of DoAr 44 (PID = 2019.1.00532.S) were carried during May of 2021, in Cycle 7, with an on-source integration time of 43 minutes and a bandwidth of 4.688 GHz.

Self-calibration of the continuum data-sets was performed with the `SNOW` package (as in Casassus and Cárcamo, 2022), which uses the `uvmem` package (Casassus and Cárcamo, 2022; Casassus et al., 2021a, 2018) to replace the `tclean` model in the CASA selfcal iterations (McMullin et al., 2007). The resulting peak signal to noise ratios (PSNR) in the restored images are ∼60 for Band 6 and PSNR ∼ 100 for Band 7, for Briggs weights with robustness parameter of 1.0. For comparison, the standard `tclean` selfcal resulted in PSNR ∼ 49 in Band 6 and PSNR ∼ 90 in Band 7. Finally, the Band 6 data-set was aligned to the Band 7 data-set using the `VisAlign` package (Casassus and Cárcamo, 2022), but without scaling in flux.

Figure 4.1a shows the reconstructed image for ALMA Band 6, with an RMS noise of $\sigma_{230\,\mathrm{GHz}}$ ∼0.019 mJy beam^{-1} and a synthesized `tclean` beam of 72.4 mas × 62.7 mas. Figure 4.1b shows the reconstructed image for ALMA Band 7, with an rms noise of $\sigma_{350\,\mathrm{GHz}}$ ∼

0.025 mJy beam^{-1} and a synthesized `tclean` beam of 70.2 mas × 53.8 mas.

For the position of the star, we used *Gaia* coordinates (Gaia Collaboration et al., 2018) of RA 16:31:33.4638 (± 0.0534 mas), DEC −24:27:37.1582 (± 0.0404 mas), which were extrapolated to RA 16:31:33.454 , DEC −24:27:37.682 by using a proper motion of (−6.101 ± 0.128, −24.212 ± 0.098) mas yr^{-1}. The center of the cavity (as calculated with `MPolarMaps` in Sec. 4.2.2), is shifted, with respect to the *Gaia* coordinates by ΔRA = 1 mas, ΔDEC = 6 mas in Band 6, and by ΔRA = 6 mas, ΔDEC = 7 mas in Band 7, as presented in Table 4.1. Given this, we can safely discard that this shift is due to a *Gaia* pointing error (∼0.15 mas at 3σ). On the other hand, the accuracy of the ALMA data astrometry is regularly taken as ∼1/10 of the synthetic beam (Remjian et al., 2019), which translates into ∼7 mas for both Band 6 and Band 7. This implies an ALMA pointing error of 21 mas at 3σ, so the shifted cavity coordinates for both bands are within the errors.

SPHERE observations

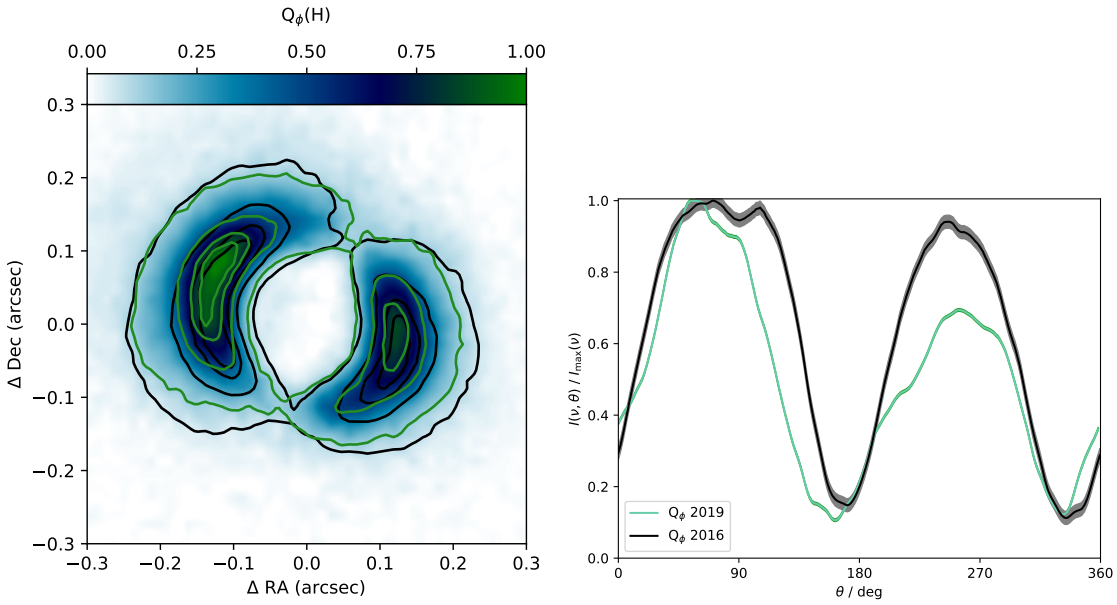

(a) (b)

Figure 4.2: 4.2a: H-band polarized intensity image, $Q_\phi(H)$, after unresolved polarization subtraction. The green referential contours correspond to our $Q_\phi(H)$ intensity image, while the black contours correspond to the 2016 $Q_\phi(H)$ polarized intensity observations presented by paper I, both after unresolved polarization subtraction. Both intensity contours are spaced at fractions of 0.13, 0.48, 0.74 and 0.87 times the peak intensity. 4.2b: Ring intensity profiles extracted along constant radii (east of north): the green line corresponds to our $Q_\phi(H)$ observations after unresolved polarization subtraction and the black line corresponds to the previous $Q_\phi(H)$ observations, from 2016, analyzed in Avenhaus et al. (2018) and in paper I. The total height of the shaded areas correspond to ±1σ.

We also used data from follow-up observations with SPHERE, the planet finder of the VLT. In this work, we use the 2019 data (preceded by 2016 096.C-0523(A) data, PI Avenhaus)

from IRDIS (Dohlen et al., 2008), a differential imaging NIR camera (working in a range from 900 nm to 2.3 μm), in the DPI mode, (see, e.g., de Boer et al., 2020). The DoAr 44 data were acquired with the IRDIS instrument on September 22 of 2019, and consisted of 60 frames in total. The observation was done in coronagraphic polarimetry mode. The 56 science frames (14 polarimetric cycles) were flanked with 'flux' and 'centering' frames. The flux frames are taken with the star displaced from the coronagraph and allow to estimate the flux of the star. Then, with the 'N_ALC_YJH_S' coronagraph (with a radius of 92.5 mas and an inner working angle, IWA, of ∼0.15 arcsec) in place, the acquired star center frames allow a precise determination of the position of the star behind the coronagraph. There were no unexpected artifacts in the science frames and all the polarimetric cycles were successfully completed with a closed adaptive optics loop, thus, no data were discarded to produce the final images. As a result, these scattered light observations were conducted with a better seeing in comparison to the observations presented in Avenhaus et al. (2018) and in paper I. The seeing varied from 0.41" at the beginning of the observations, had a peak at around 0.8" and went down to ∼ 0.6" at the end of the run. We also acquired data of DoAr 44 using the Zurich Imaging Polarimeter (ZIMPOL), however, these observations were designed without considering a coronograph, resulting in lower quality images that were not considered for this work.

The SPHERE data reduction was performed with the publicly available pipeline IRDAP (IRDIS Data reduction for Accurate Polarimetry, van Holstein et al., 2020) version 1.3.3. IRDAP extracts the images of the left and right optical channels and performs the centering using the star center frames. For each measurement taken at half wave plate (HWP) angles (0, 45, 22.5, and 67.5) the left beam is subtracted from the right beam producing the Q+, Q-, U+ and U- (double difference) images. The single sum of these left and right images (double sum) is used to produce the total intensity images. The double difference images are used to obtain the Stokes Q, U and I images. Subsequently, IRDAP corrects the Stokes images for instrumental polarization using a detailed model of the instrument's optical path. Here we performed the analysis using the H-band polarized intensity image, $Q_\phi(H)$, as shown in Fig. 4.1c.

A crucial step in the reduction is the subtraction of the halo of polarized signal associated with the unresolved signal within the central PSF, the so-called "unresolved" polarization. To remove this component we selected an annular region devoid of disk signal centered on the star with a radius of 40 to 90 pixels. The degree of linear polarization measured from the unresolved central source in DoAr 44 is 1.6±0.4%, the polarization angle (AoLP) of the central source is $\mathrm{AoLP}_{\mathrm{central}} = 19.97 \pm 7.25$ deg, and the uncertainty is the standard deviation of the unresolved polarization signal during the polarimetric cycles. This uncertainty is caused by variations in the atmospheric conditions and is higher than the statistical uncertainty and the accuracy of the Mueller matrix model used to correct the instrumental polarization.

An interesting feature to point out is that the locations of the intensity decrements change after the unresolved polarization subtraction. This effect was seen for different locations of the signal-devoided annular region. The polarized light halo that is associated to the unresolved signal most likely has an asymmetric pattern due to unresolved tilted inner disk around the star. This pattern contributes to a variability in the contrast of the intensity distribution (as also observed by Keppler et al., 2020, using SPHERE/IRDIS data of GG Tauri A), so, when subtracted, the location of the decrements are slightly affected. This is expected as a result

of correcting for the shadowing produced by the inner interstellar (IS) polarization.

Figure 4.2a compares the SPHERE/IRDIS $Q_\phi(H)$ observations with the SPHERE/ IRDIS 2016 $Q_\phi(H)$ observations described by Avenhaus et al. (2018) (project 0.96.C-0523(A)) and presented in paper I. Note that we subtracted the unresolved polarization from both data-sets using IRDAP and considering the parameters described above. As confirmed by the profiles in Figure 4.2b, the location of the north-western dip varies slightly between both data-sets, however, they show different locations for the south-eastern decrement. There are also variations in the peak intensities between epochs. These discrepancies will be further addressed in Section 4.2.4.

4.2.2 Azimuthal profiles

The location of the decrements in the ring around DoAr 44 are traced with the `MPolarMaps` package, described in Casassus et al. (2021a). This allows us to extract the ring intensity profile $I^\circ(\theta)$ as a function of azimuth θ along a circle that best approximates the disk ring, by minimizing the dispersion in the radial profile of the continuum and under the assumption of axial symmetry. As a result, we get the best fits values for the position angle (PA), the inclination (i) and the stellar offsets.

Table 4.1: Position angle and ring inclination values for DoAr44 from the polar optimization.

	230 GHz	350 GHz	$Q_\phi(H)$ fit[a]
Position Angle (PA)[b]	59.2 ± 0.8	61.6 ± 0.5	49.7 ± 1.9
Inclination (i)	21.7 ± 0.3	21.9 ± 0.2	24.4 ± 0.8
RA offset (mas)	1 ± 0.1	6 ± 0.1	2 ± 0.1
DEC offset (mas)	6 ± 0.1	7 ± 0.1	2 ± 0.1

[a] $Q_\phi(H)$ observations do not show a continuous disk, which is required for a correct polar optimization, thus, we performed a Gaussian fit along the emission peak in order to calculate the disk PA and inclination.
[b] East of North.

As shown in Table 4.1, the 230 GHz ALMA data gives an inclination $i = 21.7 \pm 0.3$ deg and a PA $= 59.9 \pm 0.8$ deg, and the offsets from the nominal stellar position are ΔRA $= 1$ mas and ΔDEC $= 6$ mas. Similarly, the optimization for the 350 GHz ALMA data gives an $i = 21.9 \pm 0.2$ deg and a PA $= 61{,}6 \pm 0.5$ deg, with offsets from the nominal stellar position as ΔRA $= 6$ mas and ΔDEC $= 7$ mas. Since the $Q_\phi(H)$ continuum does not show a continuous disk geometry due to its pronounced decrements, we fitted a continuous ellipse to the emission and used the result to run the `MPolarMaps` optimization. This gives an $i = 24.4$ deg and a PA $= 49.7$ deg for the $Q_\phi(H)$ data, with offsets from the nominal stellar position as ΔRA $= 2$ mas and ΔDEC $= 2$ mas. Note that the measurement of $I^\circ(\theta)$ depends on the choice of origin, but, as explained in Section 4.2.1, the offset between the stellar position and the center of the cavity is within the ALMA and *Gaia* pointing errors. Given this, we can safely center the cavity to *Gaia* coordinates, as presented in Figure 4.3a.

The `MPolarMaps` also records the intensity profiles as a function of azimuth for the radial

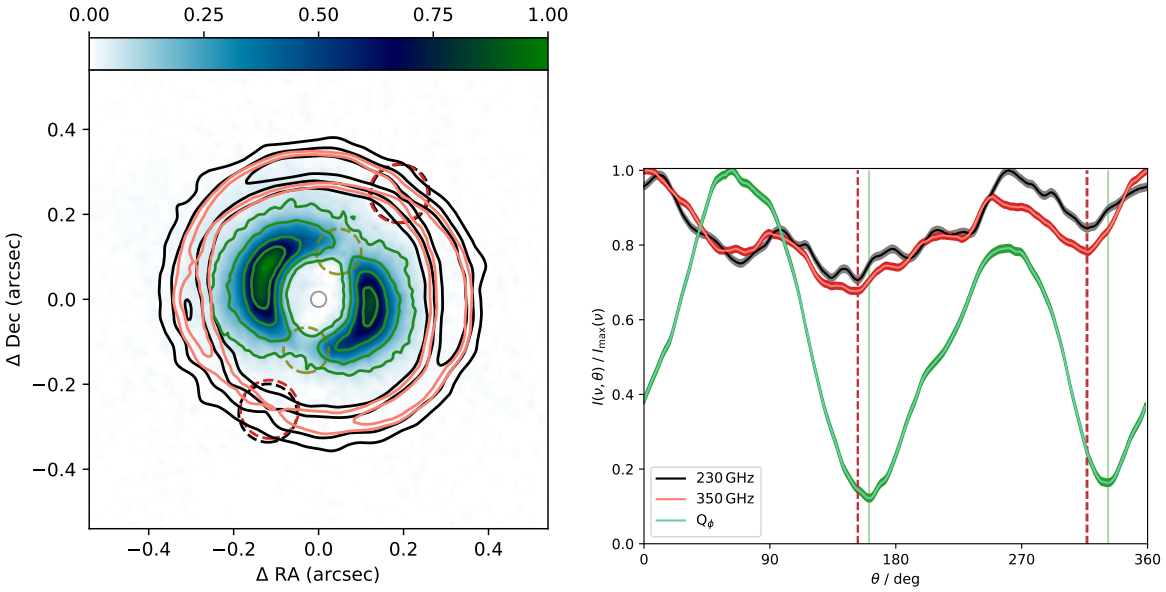

(a) (b)

Figure 4.3: 4.3a: the 230 GHz and the 350 GHz restored `uvmem` continuum in black and red contours, respectively, overlaid on the $Q_\phi(H)$-band image. The 230 GHz intensity contours are spaced at fractions of 0.5, 0.6, 0.7, 0.8 and 0.9 times the peak intensity and the 350 GHz contours are spaced at fractions of 0.68, 0.82 and 0.94 times the peak intensity. The contours for $Q_\phi(H)$ at 0.1, 0.5, 0.7 and 0.9 times the peak are shown in green. The grey circular marker at the center of the image indicates the position of the star (Sec. 4.2.2). The dashed circular markers indicate the location of the decrements along projected circles: black for 230 GHz and 350 GHz, and green for $Q_\phi(H)$. 4.3b: Ring intensity profiles extracted along constant radii. The green line corresponds to $I_H(\theta)$, the red line corresponds to $I_{350\ \mathrm{GHz}}(\theta)$ and the grey line corresponds to $I_{230\ \mathrm{GHz}}(\theta)$. The dashed grey and red lines mark the location of the decrements for 230 GHz and 350 GHz, respectively, and the solid green lines mark the location of the decrements for $Q_\phi(H)$. Note that the angle θ in 4.3b increases in the east of north direction. Also note that the $I_H(\theta)$ profile was integrated along a range of radii ($0.08\,\mathrm{arcsec} < r < 0.22\,\mathrm{arcsec}$) in order to obtain a better signal. The total height of the shaded areas correspond to 1σ.

maxima along the ring, which lets us estimate the location of the intensity decrements. Figure 4.3b shows the ring intensity profiles for all data-sets and the positions of the radio/IR intensity decrements along the projected circles. These positions, indicated by thin lines, correspond to the minima in $I^\circ(\theta)$. Table 4.2 shows the results for the optimization: the PA of the decrement (East of North) as viewed on the sky (θ_{sky}) and the stellocentric distance to the decrements on the sky ($\mathrm{r_{star}}$).

Table 4.2 shows that the PAs for both decrements at 230 GHz, 350 GHz and $Q_\phi(H)$ are closely coincident. Also, it is interesting to note that the mm-continuum, towards the north-east in Figure 4.3a, is nearly coincident with the maximum in the $Q_\phi(H)$ emission, as also seen in Figure 4.3b. We find similar results in paper I, where they tested parametric models in order to analyze the characteristics of the disk. Their results suggested that a tilted inner

Table 4.2: Summary of results from the optimization for the intensity decrements in the 230 GHz and 350 GHz continuum and $Q_\phi(H)$.

	Decrement 1 (south)			Decrement 2 (north)		
	230 GHz	350 GHz	$Q_\phi(H)$	230 GHz	350 GHz	$Q_\phi(H)$
I_D/I^a_{Peak}	98±1%	81±1%	11±0.1%	83±1%	89±1%	13±0.1%
$\theta_{sky}[\circ]^b$	152.9	152.9	160.9	316.3	316.9	331.8
r_{star}[arcsec]^c	0.29	0.28	0.12	0.32	0.31	0.12

[a,b a] Minimum intensity over peak along the ring.
[a,b b] Position Angle (location) of the decrement on the plane of the sky East of North. The errors for these values are calculated as 1/10 of the resolutions, which are in the order of 10^{-6}.
[a,b c] Stellocentric separation of the decrements on the sky.

disk provided the simplest explanation for the presence of the decrements in DoAr 44. An inner disk has been detected with ALMA in ^{12}CO emission by Antilen et al. (2023).

4.2.3 Radio/IR intensity decrements

The $Q_\phi(H)$ image (Fig. 4.1c) shows a ring divided into bipolar arcs separated by deep intensity decrements, while the 230 GHz and 350 GHz continuum images (Figs. 4.1a and 4.1b) show a smoother and approximately face-on projected circle. However, it is interesting to note the contrast between the mm-continuum and the IR in Fig. 4.3b, which shows that the decrements are much more prominent in the IR data. Also, the radio decrements of the disk appear to be shifted ahead of the IR decrements in the direction West of North (clockwise). The angular separations between the radio and IR dips on the plane of the disk (η_{shift}) are $\eta_{shift} = 14.95$ deg for the northern decrements, and $\eta_{shift} = 7.92$ deg for the southern decrements. As the dust and gas enter the shadows, we would expect to see the dust temperature decrements shifted with respect to the IR scattered light shadows (Casassus et al., 2019b). Provided a clockwise direction of rotation, the observed offset between the radio and IR shadows could be attributed to a thermal lag, and it is interesting to point out that this clockwise offset, where the radio decrements lead, is observed in different epochs (in paper I and in this work). However, a more detailed analysis with simultaneous multi-frequency imaging could provide a better grip on such thermal lag. We also note that the radio decrements in the south of the disk cannot be defined with high precision compared to the northern decrements: the disk appears to be less massive and narrower in the location of the southern decrements (as also proposed by Casassus et al. (2019b)), hence with a lower optical depth to radiation diffusion, which smooths the temperature decrements. This will be further analyzed in Sections 4.2.4 and 4.2.6.

4.2.4 Warped inner disk

Shadows in a transition disk can be interpreted as caused by a misaligned inner disk with respect to the outer disk (e.g. Marino et al., 2015; Benisty et al., 2017). The scattered light $Q_\phi(H)$ image of DoAr 44 clearly reveals the location of two shadows on the outer ring (Figs. 4.1c and 4.3). Also, Figure 4.2 shows a difference between the Avenhaus et al. (2018) $Q_\phi(H)$ observations and our $Q_\phi(H)$ observations. Note that the unresolved polarized emission was subtracted from both data-sets using the same parameters in IRDAP (Sec. 4.2.1), but the observing conditions in each epoch could have an effect on the applied correction. However, the unmatched locations of the dips between the two infrared profiles would point toward a morphological change in the location of the dips between epochs, which appears to be more significant for the southern dip. Changes in the location and morphology of intensity dips have been previously identified in other disks, for instance, in J1604, using multi-epoch scattered light observations (Pinilla et al., 2018). In the case of DoAr 44, the variability in the morphology and the location of the dips is most likely related to an illumination effect due to a shift in the orientation of the tilted inner disk. We analyze this interpretation by using two approaches: an idealized geometrical model for the location of the shadows and a qualitative analysis with radiative transfer (RT) predictions.

Idealized geometrical model

Table 4.3: Observed and calculated values for the orientation of the inner disk in DoAr44 using the idealized geometrical argument.

Observed parameters in $Q_\phi(H)$	
PA	161.7 deg
Angular separation (ω)	170.9 deg
Stellar offset (b)	0.14
Calculated parameters for the inner disk	
Inclination (i_1)	$26.4^{+5.6}_{-3.5}$ deg
PA (ϕ_1)	$110.7^{+12.7}_{-13.9}$ deg
Scale Height (h)	$0.014^{+0.006}_{-0.004}$
Relative Inclination (ξ)	$21.4^{+6.7}_{-8.3}$ deg

Min et al. (2017) propose an algorithm that considers the location of the observed shadows as the intersection of the inner disk midplane with a perfectly circular outer disk. This scheme relates the inner disk orientation (this is, inclination (i_1) and PA (ϕ_1) on the sky), to the scale height (h) of the outer disk, the PA of the observed shadows (PA) and their subtended angle relative to the star (ω), and the stellar offset (b, the intercept of the inner disk PA with the North). In practice, however, some uncertainties arise: the fact that the observed $Q_\phi(H)$ cavity is not perfectly circular makes it difficult to determine its center with precision. Also, the exact locations of the center of the shadows, this is, the decrement minimum, might not necessarily be in the midplane of the inner disk. Taking these caveats into consideration, we calculated the inner disk orientation by considering the observed values presented in Table 4.3. These give us an inner disk orientation of $i_1 = 26.4^{+5.6}_{-3.5}$ deg, $\phi_1 = 110.7^{+12.7}_{-13.9}$ deg

and $h = 0.014^{+0.006}_{-0.004}$, with uncertainties corresponding to the 1σ confidence intervals. We find that the PA value for $Q_\phi(H)$ (Table 4.2) is significantly different than that of the inner disk. These results provide support to the interpretation of the shadows being caused by a misalignment between the inner and outer disks. Bouvier et al. (2020) derived similar results for the orientation of DoAr 44's inner disk: they fitted the continuum visibilities of 2019 VLT/GRAVITY observations and calculated an inclination of $i_1 = 34 \pm 2$ deg and a PA of $\phi_1 = 140 \pm 3$ deg. Since polarization vectors are azimuthally oriented in disks, the AoLP can be either parallel or perpendicular to the direction of the disk PA (e.g., Stolker, T. et al., 2017). It is interesting to note that the polarization angle of the central source, $\mathrm{AoLP}_{\mathrm{central}} = 19.97 \pm 7.25$ deg, is perpendicular to the inner disk PA, $\phi_1 = 110.7^{+12.7}_{-13.9}$ deg. Also, in Fig. 4.3 we see that the radio intensity decrements lead in the direction west of north, both in the northern and southern regions. Considering the geometrical approach shown in Min et al. (2017, Fig. 1), if the azimuthal shift was only related to projection effects due to the emission heights, we would see the northern and southern decrements shifted opposite relative to rotation.

The orientation values we calculated from the idealized geometrical method for DoAr 44's warped inner disk correspond to a relative orientation of $\xi = 21.4^{+6.7}_{-8.3}$ deg with respect to the outer disk. We can compare this orientation of the inner disk with the results of Bohn et al. (2022), who fit parametric models to the 2019 VLT/GRAVITY visibilities in order to derive the geometry of the inner disk, while the geometry of the outer disk was derived from fitting ALMA velocity maps. They estimated two misalignment angles between the inner and outer disks, considering that, in the GRAVITY data, it is not possible to distinguish which side of the inner disk is closer to the observer: $\xi_1 = 27 \pm 9$ deg, which is consistent with our result, and $\xi_2 = 39 \pm 9$ deg. It is interesting to note that their PA and i values, both for the outer and inner disk, are also in agreement with our PA and i results.

Radiative transfer predictions

Our relative orientation of $\xi = 21.4^{+6.7}_{-8.3}$ deg can be compared with the RT predictions for inner disk tilts presented in paper I. If we examine Figure 4 in paper I, we find that our 2019 $Q_\phi(H)$ observations are better reproduced by a misalignment of $\xi \sim 20$ deg, which is in excellent agreement with $\xi = 21.4^{+6.7}_{-8.3}$. On the other hand, a relative inclination of $\xi \sim 30$ deg better accounts for $Q_\phi(H)$ images from the 2016 data. Also, the azimuthal profiles for both epochs (Figure 4.2b) are consistent with the RT predicted profiles in paper I (Fig. 7), for the aforementioned ξ values. It is interesting to note that the difference in the relative inclinations between epochs also translates into variations in the location of the shadows and in the relative brightness of the arcs between the shadows. The RT predictions for $\xi = 20$ deg result in broader decrements compared to the predictions for $\xi = 30$ deg. These effects are also observed comparing the azimuthal profiles for both $Q_\phi(H)$ epochs in Fig. 4.2b, which implies a morphological variation, particularly, in the locations of the southern decrement and the western arc.

4.2.5 Spectral index map

If due to shadowing, we would expect a drop in the dust temperature and optical depth in the location of the intensity decrements. In order to analyze this, we compute the spectral index map between 230 GHz and 350 GHz, as

$$\alpha = \frac{\log(I_{230\,\mathrm{GHz}}/I_{350\,\mathrm{GHz}})}{\log(230\,\mathrm{GHz}/350\,\mathrm{GHz})}, \tag{4.1}$$

and the error map as

$$\sigma_\alpha = \frac{\sqrt{(\sigma_{230\,\mathrm{GHz}}/I_{230\,\mathrm{GHz}})^2 + (\sigma_{350\,\mathrm{GHz}}/I_{350\,\mathrm{GHz}})^2}}{\log(230\,\mathrm{GHz}/350\,\mathrm{GHz})}. \tag{4.2}$$

We smoothed the 230 GHz image to obtain the same synthesized (elongated) beam as that of a Briggs 2.0 weighting scheme for 350 GHz (84.9 mas × 69.9 mas), using the previously aligned images (Sec. 4.2.1). It is interesting to note that the smoothed 230 GHz emission does not show dips as clear as the 350 GHz emission (Fig. 4.1b). This could be due to the fact that the 350 GHz emission is more optically thick than the 230 GHz emission, thus, being sensitive to temperature only.

The α map was computed for intensities with errors $\sigma_\alpha < 0.7$, which translates into intensities greater than 0.27 mJy in Band 6 (14σ) and 0.67 mJy in Band 7 (26σ). Note that a calibration uncertainty of 2.5 % for Band 6 and 5 % for Band 7 (Remjian et al., 2019) translates into a ± 0.13 uncertainty in the absolute value of α (using error propagation, such that $\sigma_\alpha = 0.056 \,/\, \ln(350\,\mathrm{GHz}\,/\,230\,\mathrm{GHz})$), but the values in the error map in Fig. 4.4b do not consider these systematic errors since these are uniform across the map and we are mostly interested in relative changes.

In Fig. 4.4, we find spectral index values $\alpha \sim 2$. The inner cavity (0.13 arcsec $< r <$ 0.25 arcsec, within the black intensity profiles in Fig. 4.4) shows α values much higher than ~ 2, as also seen in Fig. 4.5. This suggests an optically thin emission due to the presence of very small grains, most likely as a consequence of grain destruction by stellar radiation. The $\alpha \sim 2$ values along the rest of the disk could either correspond to an optically thick emission, or suggest a shallow dust opacity index due to larger grains ($\beta \sim 0$, e.g. Testi et al., 2014). Furthermore, this is similar to the structure of HD 142527 in Casassus et al. (2015b) who reported a drop in the intensity of the outer disk using ATCA and ALMA observations from 34 GHz to 700 GHz. We do not find distinct azimuthal spectral variations in the location of the decrements, where $\alpha \sim 2$ suggests optically thick emission (Fig. 4.4), however, the dips in the infrared profile (Fig. 4.3) point towards temperature decrements due to shadowing. We also calculated $\alpha > -2$ to be the lower limit for the star's spectral index at 1σ intensities for Bands 6 and 7.

It is particularly interesting that the spectral index values at 0.13 arcsec $< r <$ 0.25 arcsec are $\alpha \sim 3.3$, as seen in Fig. 4.5. This radial range corresponds to the inner cavity in Bands 6 and 7, where a faint dust pedestal can be observed at the edge of the inner cavity (Figs. 4.1a

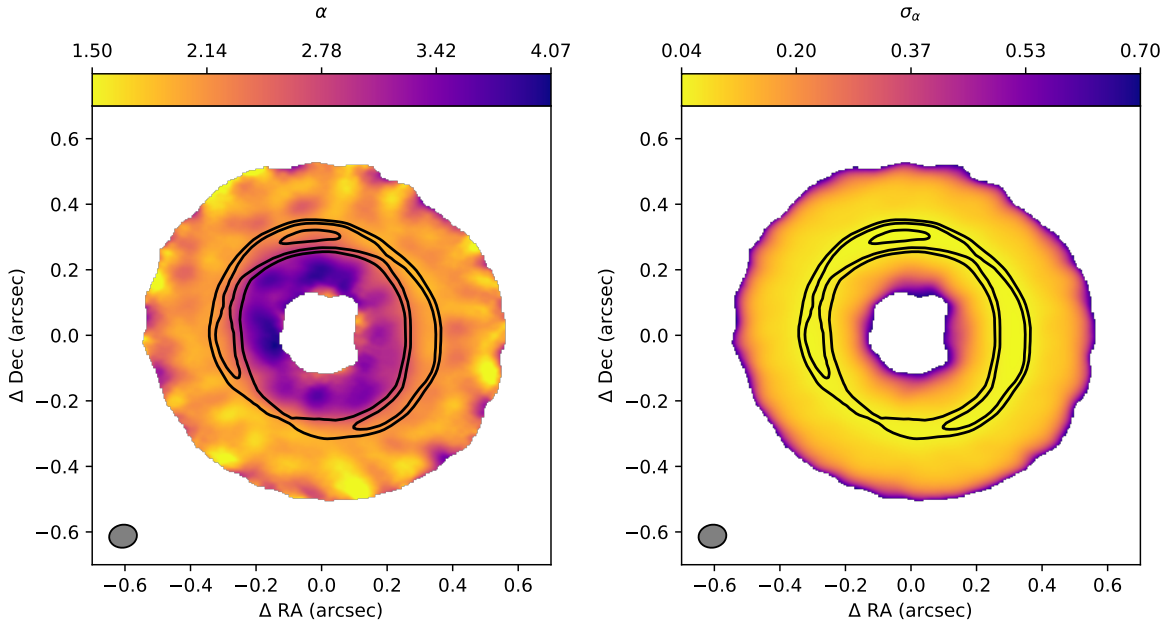

(a) (b)

Figure 4.4: 4.4a: Spectral index map of DoAr 44, computed between 230 GHz and 350 GHz. The 350 GHz intensity profiles are shown in black contours, at 0.67, 0.77 and 0.95 times the peak, in order to highlight the location of the decrement. The grey ellipse shows the synthesized beam (84.9 mas × 69.9 mas). 4.4b: Spectral index error map with 350 GHz intensity profiles in black contours, at 0.67, 0.77 and 0.95 times the peak.

and 4.1b). The spectral index values in the inner cavity are typical for the interstellar medium (ISM), therefore, considering a dust opacity index $\beta = 1.7$ (the ISM value, Draine, 2006), this can be interpreted as optically thin emission and a population of small dust grains ($a_{\rm max} << 100\,\mu$m, Sierra and Lizano, 2020) filling the cavity. This is consistent with the absence of intensity decrements in the inner cavity, which are smoothed out by optically thin thermal radiation from the dust pedestal. Also, it is intriguing that this high spectral index values are not seen towards $r = 0.5$ arcsec (Fig. 4.5), where we observe an extended dust halo outside of the radial dust trap in both Bands 6 and 7 (Figs. 4.1a and 4.1b). The $\alpha \sim$2-2.5 along the dust halo implies the presence of larger dust grains compared to the inner cavity. However, further multi-wavelength data and modelling is required to resolve these ambiguities in DoAr 44.

4.2.6 Disk gas mass estimation

The gas mass in disks is an important condition for the formation of planets, and in the case of shadowed transition disks, the cooling of the gas as it crosses the shadows can result on constraints on its mass. In this sense, Casassus et al. (2019b) presented a 1D model that relates the outer disk surface density (Σ_g) to the depth of the temperature profiles ($T(\phi)$) due to radiation stemming from the central star and the inner disk. The model considers a shadow moving relative to the gas at a retrograde Keplerian speed, a fixed disk structure described

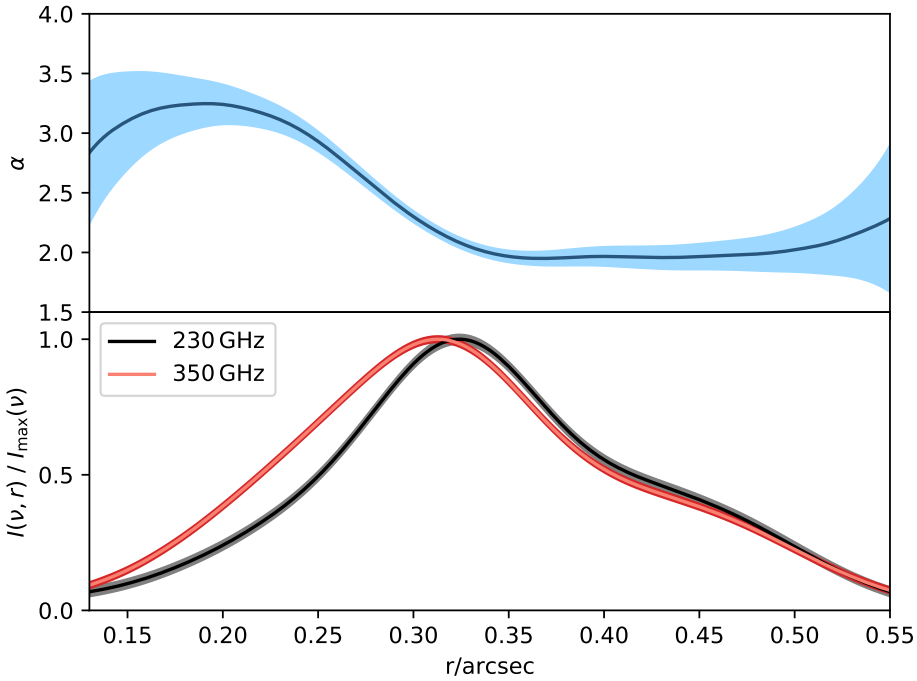

Figure 4.5: Radial profile of the spectral index derived from the radial profiles of the 230 GHz and 350 GHz continuum following Eq. 4.1. The shaded regions trace the radial profile errors. The profile is derived following the radial range that corresponds to the values presented in Fig. 4.4a ($0.13\,\mathrm{arcsec} < r < 0.55\,\mathrm{arcsec}$).

by its radius (R) and thickness (H), and a standard dust population, with a maximum grain size (a_{max}), the gas-to-dust mass ratio (f_{gd}) and the grain filling factor (f). Hence, the free parameters governing the gas temperature are the observed angular shifts between the radio and IR decrements, η_{shift}, and the gas surface density, Σ_g. Note that here we define η_{shift} on the plane of the disk, as opposed to paper I that defined η_{shift} on the plane of the sky.

In the case of DoAr 44, the observed angular shifts between the radio and IR decrements, described in Section 4.2.3, can be explained by a thermal lag between the shadowed dust and gas, provided that the outer disk has a retrograde direction of rotation. The $T(\phi)$ profiles were computed considering a maximum grain size of $a_{\mathrm{max}} = 1\,\mathrm{cm}$, which is consistent with the optically thick $\alpha \sim 2$ values found for the outer disk (Figs. 4.4 and 4.5). We also use the established gas-to-dust mass gas ratio for the diffuse ISM, $f_{\mathrm{gd}} = 100$, and a filling factor for compact grains $f = 1$. These parameters are presented in Table 4.4.

Table 4.4: Parameters for the disk mass calculation.

Parameter	Value
Angular shift between radio and IR dips (η_{shift})	north: 14.95 deg south: 7.92 deg
Maximum grain size (a_{max})	1 cm
Gas-to-dust mass ratio (f_{gd})	100
Filling factor (f)	1

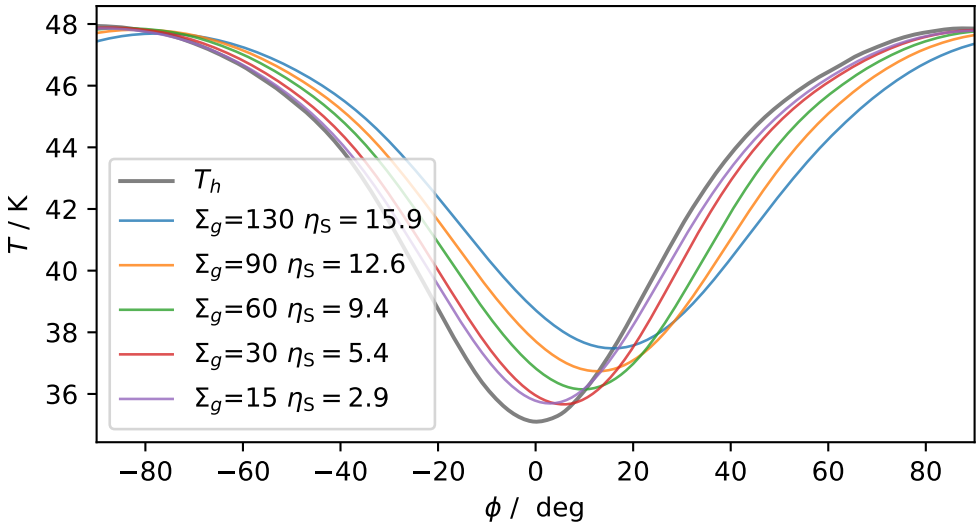

Figure 4.6: Profiles $T(\phi)$ that approximate DoAr 44. The curves were computed for $a_{\rm max} = 1$ cm, $f_{\rm gd} = 100$ and $f = 1$. The direction of the gas Keplerian rotation is towards $+\phi$

Figure 4.6 shows the resulting $T(\phi)$ profiles for different values of $\eta_{\rm shift}$ and Σ_g. The angular shift between the northern decrements is $\eta_{\rm shift} = 14.95$ deg, which corresponds to an interpolated surface density of $\Sigma_g = 117 \pm 10$ g/cm^2, and the southern decrements have an angular shift of $\eta_{\rm shift} = 7.92$ deg, which corresponds to an interpolated surface density of $\Sigma_g = 48 \pm 10$ g/cm^2. A lower value of Σ_g means that the location of the southern dip is optically thinner to thermal radiation, which is consistent with the southern decrement being smoother and broader (as seen in Figure 4.3b), as a result of thermal diffusion for the considered disk rotation. The contrast ratio between the estimated intensity decrements along the outer ring gas surface density is $f_r = 2.4 \pm 0.5$, a value that is consistent with the presence of a large crescent of continuum sub-mm emission in the disk (Zhu and Baruteau, 2016), as in, e.g., LkHα330 (Isella et al., 2013), HD 135344B (van der Marel et al., 2015) and MWC 758 (Casassus et al., 2019a). Also, it is interesting to note that, in the context of a lopsided vortex, the southern decrement may correspond to significantly lower optical depths in the ALMA continuum. Yet the spectral index in the location of both decrements remains $\alpha \sim 2$ (Fig. 4.4). If the southern decrement is optically thin, perhaps dust trapping in DoAr 44 is efficient only for the denser large grains, while a population of fluffy large grains would account for spectral index of the continuum halo and the southern decrement.

4.3 Summary

Warps have often been used to explain disk properties, but well characterized examples are important due to their role in disk evolution. Scattered light images of disks with central gaps have revealed sharp warps, such that the outer rings are shadowed by tilted inner disks. The near-IR intensity drops along the ring around TTauri star DoAr 44 have been interpreted in terms of a central warp. We report new ALMA observations of DoAr 44 in the continuum at

230 GHz and 350 GHz (at $\sim$10 au), along with a new epoch of SPHERE/IRDIS differential polarized imaging taken during excellent weather conditions. The ALMA observations resolve the ring and confirm the decrements proposed from deconvolution of coarse 336 GHz data. The scattered light image constrains the dips, which correspond to a misaligned inner disk with a relative inclination $\xi = 21.4^{+6.7}_{-8.3}$ deg. The SPHERE intensity profile shows a morphological change compared to a previous epoch that may be interpreted as a variable orientation of the inner disk, from $\xi \sim 30$ deg to $\xi \sim 20$ deg. The intensity dips probably correspond to temperature decrements, as their mm-spectral index, $\alpha^{230\mathrm{GHz}}_{350\mathrm{GHz}} \sim 2.0 \pm 0.1$, is indicative of optically thick emission. The azimuth of the two temperature decrements are leading clockwise relative to the IR-dips, by $\eta = 14.95$ deg and $\eta = 7.92$ deg. For a retrograde disk, such shifts are expected from a thermal lag and imply gas surface densities of $\Sigma_g = 117 \pm 10$ g/cm^2 and $\Sigma_g = 48 \pm 10$ g/cm^2. A lopsided disk, with contrast ratio f_r=2.4 ± 0.5, is also consistent with the large continuum crescent.

Chapter 5

Conclusions and future prospects

This thesis studied the characteristics of dust-related emission mechanisms observed at different interstellar size-scales. The main objective was to gain insights on the properties of the ISM dust and understand its role in the different stages of star and planet formation. To do this, I interpreted multi-frequency radio-interferometric and IR continuum observations in terms of the most relevant dust emission mechanisms: electric dipole radiation of spinning very small grains, polarized dust emission, scattered light and thermal emission from larger grains. This thesis was conducted through three projects on the topic of radio continuum observations of circum- and interstellar dust.

First, on molecular cloud scales ($\sim$ 10-100 pc) I focused on the analysis of resolved spinning dust emissivity variations observed in the ρ Oph W PDR. The main objective was to study the correlations between the 31 GHz emission peak and dust tracers in order to better understand the nature of the AME carriers and quantify its local variations. Second, on star-forming-region scales, ($\sim$ 0.1-10 pc) I studied the impact of the interstellar magnetic field at core-scale in high-mass star-forming region W43-MM1. The comparison between the orientation of the magnetic field and the position angle of a statistically significant number of pre-stellar cores, allowed for a detailed analysis of the role of the magnetic field in the formation of massive stars and their circumstellar disks in this region. Finally, on protoplanetary disks scales ($\sim$10-100 au), I analyzed the possibilities of a warped geometry in transition disk DoAr 44 by characterizing sub-mm and IR continuum dust emission. The constraints on the dust grain population is crucial to understand the processes that lead to the presence of the observed lopsided rings and their association with planetesimal formation.

The work presented in this thesis has been published in the Monthly Notices of the Royal Astronomical Society (MNRAS, chapters 2 and 4) and in Astronomy & Astrophysics (A&A, chapter 3). The whole data-set, available and provided by the author of this thesis, consists of multi-frequency cm, (sub-)mm and IR observations at arc-minute and (sub-)arc-second angular resolutions.

5.1 Emissivity variations of PAHs: radiative torques or environmental factors?

Chapter 2 presents 31 GHz observations from the CBI 2 of the ρ Oph W PDR, at an angular resolution of 4.5 arcmin. The spinning dust emission runs along the PDR exposed to the ionizing star HD 147889. Interestingly, there is no significant 31 GHz emission from S1, the brightest IR nebula in the complex, suggesting that the AME is not directly correlated with the sole presence of PAHs.

To understand the nature of the 31 GHz emission, we calculated the correlations of the CBI 2 data with different IR templates, with PAHs column density proxies, and with dust radiance and optical depth templates. These estimations showed that the 31 GHz emission is related to the local PAH column density: the best correlation was found when using the 12 µm PAH column density proxy and it is significantly better than when using the 8 µm and 3 µm PAH column density proxies. We also measured the correlations at different angular resolutions and found that the dust radiance correlation is better at a lower angular resolution. This shows that the effect of angular resolution must be considered when interpreting morphological correlations, implying in this case that PAHs cannot be ruled out as spinning dust carriers, as previous studies at lower angular resolutions have suggested. Additionally, we calculated a spectral index of $\alpha = 0.05 \pm 0.08$, between 28.5 GHz and 33.5 GHz, that is consistent with the flat spectrum previously reported on this region.

By using a 12 µm / 3 µm ratio map, we measured an increase of the PAH size in the transition between the PDR and the molecular cloud. Motivated by the intrinsic scatter in the correlation plots, we constructed a proxy for the 31 GHz emissivity per spinning dust emitter so as to quantify its variations. Using a `gpu-uvmem` model of the 31 GHz emission, we found that the spinning dust emissivity peak over the PDR is, at least, 25 times greater over the noise, at 3σ, and 23 times greater than at the location of star S1, also at 3σ.

These results suggest that the spinning dust emissivity boost in ρ Oph W appears to be dominated by local conditions in the PDR. In the framework of the spinning dust interpretation, these emissivity variations may hold the key to identify the dominant grain spin-up mechanisms. Considering the fainter, almost negligible, 31 GHz signal from stars S1 and SR3, possible explanations for the observed local AME variations are environmental ions or a changing grain population. To further analyze these possibilities, I co-authored a second study on the ρ Oph W PDR using multi-frequency observations from the Australian Telescope Compact Array (ATCA) and the Compact Array Band (CABB), at an angular resolution of ~ 30 arcseconds (Casassus et al., 2021b). The $17 - 39$ GHz observations resolve the PDR and reveal spectral variations that confirm the morphological changes of the continuum dust emission throughout the ρ Oph complex. The radio emission appears to be shifted towards the UV ionizing star HD 147889 at higher frequencies, and the 20 GHz map correlates the best with the 8µm mid-IR emission. This seems to be related to the size distribution of the dust grains across the PDR, so physical conditions for the SED were estimated using an optimization of the dust parameters (including grain sizes) with the `SPDUST` package. The estimations resulted in a minimum PAH size cutoff of $a_{\rm cutoff} \sim 6$ nm. This result suggests that the observed morphological spectral differences can be explained by the presence of a larger

number of the smallest PAHs towards the ionizing star, due to the fragmentation of larger PAHs by the UV radiation.

The results obtained by Casassus et al. (2021b) agree with the conclusions presented in this thesis. The confirmation of the negligible radio emission from the IR circumstellar nebulae around stars S1 and SR3, safely rules out the hypothesis of *radiative torques* as an explanation for the strong radio signals observed in the PDR. The radiation field from these stars does not seem to be the main cause for the torques that produce the spinning dust emission at the observed frequencies. *Plasma drag* could also be considered as the source of the PAHs rotational excitation, but in order to trace the presence of ions throughout ρ Oph W (C^+ or H^+), resolved observations of carbon recombination lines are needed.

The conclusions presented for this section provide evidence that the physical characteristics of the spinning PAHs, which are determined by the environmental factors (e.g., their size distribution), are, most likely, one of the main causes of the emissivity variations in ρ Oph W. The dipole moment of the PAHs may considerably change as a function of their size, causing the spinning dust emissivity to vary. Further multi-frequency and spectral radio analysis of this PDR are needed in order to better understand the local conditions that affect the VSGs and that give rise to the observed spinning dust emissivity variations.

Another important conclusion presented in this section is that PAHs are the most probable carriers of AME. This becomes particularly interesting if considering that AME can be used as a proxy to trace the presence of VSGs at smaller size scales, such as in protoplanetary disks. AME has been tentatively detected in protoplanetary disks, e.g., HD 97048, MWC 297, V 892 Tau (Greaves et al., 2018), or in MWC 758 (Casassus et al., 2019a). Also, protoplanetary disks have shown well constrained PAHs and nanosilicates (both VSGs) features, usually around Herbig Ae/Be stars and TTauri stars (e.g., Seok and Li (2017)). In general, the layers of a protoplanetary disk are exposed to the UV radiation of the young central star, favoring the presence of VSGs towards the surface, and the presence of larger grains in clumps towards the disk interior. The re-emission of the VSGs will heat the larger grains and produce thermal emission, while the spinning VSGs in the surface will produce AME, which is thought to dominate over thermal emission at frequencies $\nu < 60$ GHz (considering only PAHs, Hoang et al. (2018)). Vertical mixing in protoplanetary disks can cause the constant circulation of VSGs from the surface to the interior of the disk (Siebenmorgen and Heymann, 2012). In this sense, high-angular resolution radio observations of protoplanetary disks, for instance, with ALMA Band 1, will improve our ability to trace spinning dust emission from protoplanetary disks. The improved dynamic range of the ALMA Band 1 observations will allow to better constrain any VSGs spinning dust emission apart from the free-free emission caused by the stellar radiation. This new window will offer important insights on the presence of specific nanoparticles, both in the surface and interior of a protoplanetary disk.

The work presented in chapter 2 and its conclusions have been published in Arce-Tord et al. (2020b), and a continuation of this work has been published in Casassus et al. (2021b).

5.2 The impact of the core-scale magnetic field in W43-MM1

Magnetic fields may contribute to support clouds against gravity, thus indirectly affecting the evolution of individual pre-stellar cores. In this sense, magnetic fields would also directly affect the evolution of pre-stellar cores and the subsequent formation of their circumstellar disks. Chapter 3 presents ALMA Band 6 polarized thermal dust emission toward a sample of dense cores in the high-mass protostellar cluster W43-MM1, at an angular resolution of $\sim$0.50″ ($\sim$ 0.01 pc, or 2700 au). The observations recover an ordered magnetic field pattern in the Main protocluster of the W43-MM1 HMSFR (see Fig. 3.2), plus a few detections in its SW protocluster (see Fig. 3.3). This is in agreement with previous observations of polarized dust emission toward the W43-MM1 HMSFR (Cortes and Crutcher, 2006; Sridharan et al., 2014; Cortes et al., 2016). This thesis also compares the orientation of the magnetic field with new data of the orientation of 29 dense stellar cores and archival data of 28 outflow lobes in this region.

The main results suggest that the major axes of the cores are not randomly oriented with respect to the magnetic field, showing that the magnetic field is well coupled to the dense material composing the cores. Instead, the cores are compatible with an orientation of 20-50° with respect to the magnetic field. Protoplanetary disks are formed by the gravitational collapse of pre-stellar cores, and if confirmed, this result could rule out the magnetically-controlled core-collapse models, in which a flattened envelope (or pseudodisk) is expected to develop orthogonally to the magnetic field lines at scales of a few thousands of au. It is interesting to point out that ideal MHD simulations of gravitational collapse of cores have shown that such configurations, where the rotation axis of the core is not parallel to the magnetic field direction, reduce the magnetic braking and favor the formation of circumstellar disks (e.g., Joos et al. (2012)). MHD simulations by Lebreuilly et al. (2021) also found that reducing the impact of magnetic braking favors the formation of small disks. More specifically, non-ideal MHD simulations reported that such configurations would engender warped disks, very common features among transitions disks, implying that the PA of the pseudo-disks would differ from the PA of the inner-disks (see, e.g., the Fig. 3-middle row of Tsukamoto et al. (2018)).

The non-random 50-70° configuration found for the orientation between the magnetic field and a sample of 28 outflow lobes, suggests that, in some cases, the magnetic field at core-scale is strong enough to maintain a consistent orientation of the outflows down to 0.1-10 au scales. In this scenario, the magnetic field at core-scale also sets the orientation of the disk. This is interestingly coherent with the fact that a population of cores with their major axes oriented 20-50°, as also obtained for this region, would translate into a population of outflows oriented 40-70° with respect to the magnetic field lines (i.e. the orientation of the cores plus 90°). The differences in the statistical significance (p-value) between the 20-50° CDF of the cores PA versus the magnetic field, and the 50-70° CDF of outflows orientations versus the magnetic field, could be explained if considering a weaker magnetic field in certain samples. This could be the explanation for the second resulting configuration, which favors a random orientation between the outflows and the magnetic field lines. This result suggests that, in some pre-stellar cores, the magnetic field is actually not strong enough to govern the

angular momentum and, thus, set the orientation of the disk. The latter is then controlled by other mechanisms such as angular momentum redistribution and/or gravitational interaction in multiple systems.

It is worth noting that these results consider that the elongation of the analyzed cores is representative of the PA of their underlying disk. The random configuration that matches the CDF of the orientation between the cores and outflows PA does not agree with previous observations of low-mass protostellar objects, where outflows tend to be perpendicular to their underlying disks at <200 au scales. Given this, the random orientations observed in this case could reflect that the elongation of the cores is actually not representative of the PA of the disks, or that the outflows get randomly deflected at scales below our angular resolution (∼2700 au). In such cases, the angular momentum of the disks is set by processes acting at scales smaller than the resolution of the observations presented in this thesis.

The work presented in chapter 3 and its conclusions have been published in Arce-Tord et al. (2020a).

5.3 The lopsided disk of DoAr 44

Chapter 4 reports ALMA 230 GHz and 350 GHz observations of DoAr 44 with a linear resolution of ∼10 au, as well as new differential polarized SPHERE/IRDIS observations. The new $Q_\phi(H)$ observations correspond to a 3-year time difference follow-up.

The most interesting features are the observed intensity dips in the resolved ALMA imaging of the radio continuum, which confirm the predictions from paper I. The locations of the northern radio decrements in both 230 GHz and 350 GHz are fairly aligned, with position angles of 316.3 deg and 316.9 deg, east of north, respectively. The southern radio decrements, which seem broader, are both aligned at a position angle of 152.9 deg east of north. If considering DoAr 44 as a retrograde disk (this is, rotating clockwise), the observed temperature decrements are leading in the direction of rotation relative to the $Q_\phi(H)$ decrements, by $\eta = 14.95$ deg in the location of the northern dips and $\eta = 7.92$ deg in the location of the southern dips. Geometrical models of $Q_\phi(H)$ provide support for a misaligned inner disk, with a relative inclination of $\xi = 21.4\,^{+6.7}_{-8.3}$ deg. The position angle joining both $Q_\phi(H)$ decrements results in a shift along the direction west of north, compared to previous observations presented in paper I. This is reflected in the morphological change in the location of the southern decrement, which also implies a variation in the orientation of the inner disk between the two $Q_\phi(H)$ epochs. Also, the analysis suggests that the intensity dips may correspond to temperature decrements, since the spectral index map between 230 GHz and 350 GHz shows values $\alpha \sim 2$ in the location of the shadows, which is consistent with optically thick emission. Disk gas mass estimates using the angular shifts between the radio and IR decrements, and for a standard dust population, give surface density values of $\Sigma_g = 117 \pm 10$ g/cm^2 for the northern decrement, and $\Sigma_g = 48 \pm 10$ g/cm^2 for the southern decrement. A lower value of Σ_g is consistent with a broader and smoother temperature decrement in the south. The spectral index values $\alpha \sim 3.3$ in the inner cavity, where a faint mm-wavelength dust pedestal at the edge of the cavity is observed, are typical for the ISM and suggest optically thin emission due to the presence of smaller grains compared to the outer regions of the disk where $\alpha \sim 2$. The

observed mm-wavelength outer dust halo shows spectral index values around $\alpha \sim 2$, which can be interpreted as optically thick emission or as a shallow dust opacity index, and suggests the presence of fluffy large grains.

Multi-wavelength data of DoAr 44 is required to further constrain the spectral index variations observed in this thesis. The intensity dips in the DoAr 44 continuum imply that the dust in the outer ring has time to cool as it enters the shadow, so the shadow crossing time must be comparable to the gas cooling time. A further analysis of multi-frequency data will allow to measure the depths of the drops under the shadows at different frequencies, in order to accurately locate the shift of the decrements in the direction of rotation, as a result of a finite cooling timescale. The dynamical consequences of the deep shadows remain unclear, particularly how they affect the temperature and pressure of the gas. In the case of the spectral index variations, a more detailed characterization of the physical and chemical properties of dust grains is relevant for comprehending their effects on disk evolution and planetesimal formation.

The work presented in chapter 4 and its conclusions have been published in Arce-Tord et al. (2023).

5.4 Future prospects and upcoming work

The results and conclusions presented in this thesis can be used as a basis for a better understanding of the formation and evolution of circumstellar disks, using dust emission observations of highly sensitive radio-interferometers. By understanding the role of PAHs as the carriers of AME in molecular clouds (specifically in PDRs), low-frequency radio-interferometric observations at au-scales will open a new window for analyzing the chemical composition of dust in protoplanetary disks. The detection of local spinning dust emission in disks can be used as an additional tracer of the distribution of VSGs. At cm- and mm-wavelengths, spinning dust emission can be further resolved in PDRs with arc-second resolution observations using the VLA at frequencies between 5 and 50 GHz. This can be complemented with arc-second observations using ATCA or the Large Millimeter Telescope (LMT), at frequencies up to 100 GHz. Moreover, more exciting possibilities arise with the ALMA Band 1 low frequency receivers, that cover the frequency range between 30 and 50 GHz at sub-arc-second angular resolutions. This will allow for much better constraints of the AME and the opportunity of exploring the nature of its carriers in a wide variety of sources, from extragalactic diffuse regions, down to compact objects, such as protoplanetary disks. These observations will be further improved with the next generation of low frequency interferometers, such as the ngVLA and the SKA.

The formation of circumstellar disks depends on the characteristics of the gravitational collapse of pre-stellar cores, where the magnetic field also plays a fundamental role. As previously discussed, simulations have shown that properties such as the strength of the magnetic field or its interaction with the dense core matter (e.g. magnetic braking) can influence on outcomes, such as the number of disks formed in an SFR, and even on their geometry. Understanding the influence of the magnetic field at core-scale is a starting point to trace more accurately the characteristics of the circumstellar disk to be formed. At sub-mm

wavelengths, the unprecedented angular resolution achieved by polarimeters such as ALMA, along with the SMA and CARMA, are opening a very exciting window to the analysis of polarized dust-emission mechanisms in protoplanetary disks.

At disk size-scales, the nature of the observed polarized light is still a subject of debate: the effects of self-scattering are more pronounced at au-scales, leading to ambiguities in the analysis of polarization patterns. However, the observation of polarized emission is crucial to constrain the properties of dust grains in disks, and can be used as an independent method from the spectral energy distribution characterization (Pohl et al., 2016). On the other hand, simulations have suggested that the polarization observed in certain disks could be explained as polarized thermal emission in the Mie regime (Guillet et al., 2020). The difference between these two scenarios would lie in the observed polarization patterns. In this sense, polarimetric radio-interferometric observations, with angular resolutions reaching au size-scales, are becoming increasingly important to understand the nature of the polarized dust emission from disks.

5.4.1 The spectrum and characterization of resolved AME

The ALMA Band 1 receivers offer the potential to resolve and analyze the diffuse spinning dust emission of PAHs. To do this, it is important to separate the stellar free-free flux densities, that dominate below ∼40 GHz, from the spinning dust component. Even when VLA and ATCA observations are able to resolve dust structures in several disks, they are limited in dynamic range. Given this, we have presented a proposal to analyze the Band 1 continuum of Herbig Ae/Be disks that are bright in PAHs IR bands, such as, HD 97048 and HD 142527. The main goals are to confirm the nature of the extended cm-wavelength signal previously detected in both disks and to provide high-fidelity images in order to constrain the population of the very small grains.

Another intriguing dust-correlated phenomenon, besides the AME, is the Extended Red Emission (ERE). This is an ISM dust-related photoluminescence process, that can be observed between 500 and 1000 nm. It is thought to be produced by the absorption of a high energy photon (E > 10.5 eV) which leads to the emission of photons at a lower energy observed in the optical range (Leger et al., 1988). ERE has been show to be present in many dusty interstellar environments, such as reflection nebulae and HII regions. Similar to AME, the nature of the carriers producing ERE is still debated, but it has been proposed that they may be nanometer-sized grains resulting from photodissociation processes. A key characteristic of the ERE spectrum is its correlation with the intensity of the UV radiation field (Witt et al., 2006). Both ERE (Witt et al., 2006) and AME (Tibbs et al., 2011) have been observed to be strongly correlated to the local density of the UV illuminating radiation field. It is possible that ERE and AME are produced by the same carrier particle: the smallest grains that can survive under strongly irradiated interstellar conditions in PDRs. I was allocated observing time with the VLA as a PI (PID = 19B-260), to map the AME in a well known ERE source. The main goal is to analyze the AME spectrum between 5 and 50 GHz at arc-second angular resolutions. This data-set resolves the AME and will allow for a detailed analysis to test if there is a real connection between AME and ERE through a morphological correlation between both dust-emission mechanisms.

5.4.2 Multi-frequency characterization of dust grains at au-scales

One of the most relevant issues in the study of dust in protoplanetary disks is the appropriate estimation of the effects of self-scattering. This applies to dust characterization in the continuum and to polarized dust emission. One of our upcoming projects will focus on the analysis of a Herbig disk that has shown to harbour planet formation signposts, including a cavity, prominent spiral arms and a lopsided mm-continuum. Very elongated vortexes seem to be consistent with observations of this disk, in particular, the presence of a long arc. With a multi-frequency data-set, we aim to place constraints on the dust grain population in these disks using forward-modeling of the multi-frequency continuum. We will use the uniform slab approximation to relate the emergent continuum with the dust properties, including a simplified treatment of self-scattering as in Casassus et al. (2019a) and Casassus et al. (2023). The thermal continuum from dust emerging from a slab depends on the dust temperature, the dust albedo, and the total optical depth, including both absorption and scattering opacities. The opacities can be calculated using Mie theory for a given dust population, characterized by the power-law exponent in grain sizes and the maximum grain size. We can thus use multi-frequency continuum data to extract maps for the dust temperature, albedo and maximum grain size.

In this case, we will perform this analysis on transition disk HD 135344B by adding long-baseline (LB) Band 6 observations to available archive data from 0.43 mm to 2.8 mm. This approach will allow a measurement of the maximum grain size as a function of radius and azimuth, thus testing: 1- the theoretical models that predict the trickle of the mm-sized grains through the ring gaps, and 2- the vortex hypothesis to shape the lopsided outer ring.

Bibliography

Ali-Haimoud, Y. Astrophysics Source Code Library, 2010.

Ali-Haïmoud, Y., et al. *MNRAS*, 395:1055–1078, 2009.

Ali-Haimoud, Y. *A New Spin on Primordial Hydrogen Recombination and a Refined Model for Spinning Dust Radiation*. Phd thesis, California Institute of Technology, 2011.

Allamandola, L. J., et al. *ApJL*, 290:L25–L28, 1985.

Allen, A., et al. *ApJ*, 599(1):363–379, 2003a.

Allen, A., et al. *ApJ*, 599(1):351–362, 2003b.

Ami Consortium, et al. *MNRAS*, 394:L46–L50, 2009.

Andersson, B. G., et al. *Ann. Rev. of Astron. and Astroph.*, 53:501–539, 2015.

André, P., et al. *Astronomy & Astrophysics*, 518:L102, 2010.

Andrews, S. M., et al. *ApJ*, 700(2):1502–1523, 2009.

Andrews, S. M., et al. *ApJ*, 732(1):42, 2011.

Antilen, J., et al. *MNRAS*, 522(2):2611–2627, 2023.

Arce-Tord, C., et al. *Astronomy & Astrophysics*, 640:A111, 2020a.

Arce-Tord, C., et al. *MNRAS*, 495(3):3482–3493, 2020b.

Arce-Tord, C., et al. *MNRAS*, 526(2):2077–2085, 2023.

Avenhaus, H., et al. *ApJ*, 781(2):87, 2014.

Avenhaus, H., et al. *ApJ*, 863(1):44, 2018.

Bacciotti, F., et al. volume 55 of *Astrophysics and Space Science Proceedings*, page 87, 2019.

Battistelli, E. S., et al. *ApJ*, 801:111, 2015.

Battistelli, E. S., et al. *ApJ*, 877(2):L31, 2019.

Benisty, M., et al. *Astronomy & Astrophysics*, 597:A42, 2017.

Bennett, C. L., et al. *ApJ Suplement Series*, 208:20, 2013.

Beuther, H., et al. *ApJL*, 724(1):L113, 2010.

Beuther, H., et al. *Astronomy & Astrophysics*, 617:A100, 2018.

Beuzit, J. L., et al. *Astronomy & Astrophysics*, 631:A155, 2019.

Biller, B., et al. *ApJL*, 753(2):L38, 2012.

Blandford, R. D. et al. *MNRAS*, 199:883–903, 1982.

Bohn, A. J., et al. *Astronomy & Astrophysics*, 658:A183, 2022.

Bondar, A. *MNRAS*, 423(1):725–734, 2012.

Bouvier, J., et al. *Astronomy & Astrophysics*, 636:A108, 2020.

Brunngräber, R. et al. *Astronomy & Astrophysics*, 640:A122, 2020.

Camenzind, M. In Klare, G., editor, *Reviews in Modern Astronomy*, volume 3, pages 234–265, 1990.

Cárcamo, M., et al. *Astronomy and Computing*, 22:16–27, 2018.

Carrasco-González, C., et al. *Science*, 330(6008):1209, 2010.

Casassus, S., et al. *ApJ*, 639:951–964, 2006.

Casassus, S., et al. *MNRAS*, 391:1075–1090, 2008.

Casassus, S., et al. *ApJL*, 754(2):L31, 2012.

Casassus, S., et al. *ApJ*, 811(2):92, 2015a.

Casassus, S. et al. *MNRAS*, 513(4):5790–5798, 2022.

Casassus, S., et al. *ApJ*, 812(2):126, 2015b.

Casassus, S., et al. *MNRAS*, 477(4):5104–5114, 2018.

Casassus, S., et al. *MNRAS*, 483(3):3278–3287, 2019a.

Casassus, S., et al. *MNRAS*, 486(1):L58–L62, 2019b.

Casassus, S., et al. *MNRAS*, 507(3):3789–3809, 2021a.

Casassus, S., et al. *MNRAS*, 502(1):589–600, 2021b.

Casassus, S., et al. *MNRAS*, 526(1):1545–1558, 2023.

Castellanos, P., et al. *MNRAS*, 411(2):1137–1150, 2011.

Chandrasekhar, S. et al. *ApJ*, 118:113, 1953.

Chapman, N. L., et al. *ApJ*, 770(2):151, 2013.

Ching, T.-C., et al. *ApJ*, 838:121, 2017.

Cieza, L. A., et al. *MNRAS*, 482(1):698–714, 2019.

Cieza, L. A., et al. *MNRAS*, 501(2):2934–2953, 2021.

Clayton, D. D. et al. *Ann. Rev. of Astron. and Astroph.*, 42(1):39–78, 2004.

Commerçon, B., et al. *ApJL*, 742:L9, 2011.

Compiègne, M., et al. *Astronomy & Astrophysics*, 525:A103, 2011.

Condon, J. J., et al. *The Astronomical Journal*, 115:1693–1716, 1998.

Cortes, P. et al. *ApJ*, 639:965–968, 2006.

Cortes, P. C., et al. *ApJL*, 825:L15, 2016.

Cortes, P. C., et al. *ApJ*, 884(1):48, 2019.

Croiset, B. A., et al. *Astronomy & Astrophysics*, 590:A26, 2016.

Crutcher, R. M. *Annual Review of Astronomy and Astrophysics*, 50(1):29–63, 2012.

Crutcher, R. M., et al. *ApJ*, 600(1):279–285, 2004.

Davidson, J. A., et al. *ApJ*, 732:97, 2011.

Davies, R. D., et al. *MNRAS*, 370:1125–1139, 2006.

de Boer, J., et al. *Astronomy & Astrophysics*, 633:A63, 2020.

Dehant, V., et al. *Cosmic Dust: From science questions to Solar System exploration*. 2021.

Dent, W. R. F., et al. *MNRAS*, 482(1):L29–L33, 2019.

Dickinson, C., et al. *MNRAS*, 379:297–307, 2007.

Dickinson, C., et al. *ApJ*, 690:1585–1589, 2009.

Dickinson, C., et al. *New Astronomy Reiew.*, 80:1–28, 2018.

Dohlen, K., et al. In *Ground-based and Airborne Instrumentation for Astronomy II*, volume 7014, page 70143L, 2008.

Dong, R., et al. *ApJ*, 809(1):93, 2015.

Draine, B. T. *ApJ*, 636(2):1114–1120, 2006.

Draine, B. T. et al. *ApJ*, 508:157–179, 1998a.

Draine, B. T. et al. *ApJL*, 494:L19+, 1998b.

Draine, B. T. et al. *ApJ*, 285:89, 1984.

Draine, B. T. et al. *ApJ*, 657:810–837, 2007.

Draine, B. T. *Physics of the Interstellar and Intergalactic Medium*. 2011.

Erickson, W. C. *ApJ*, 126:480, 1957.

Espaillat, C., et al. *ApJ*, 717(1):29, 2010.

Evans, I., Neal J., et al. *ApJ Suplement Series*, 181(2):321–350, 2009.

Falceta-Gonçalves, D., et al. *ApJ*, 679(1):537, 2008.

Fazio, G. G., et al. *ApJ Suplement Series*, 154:10–17, 2004.

Ferreira, J. *Astronomy & Astrophysics*, 319:340–359, 1997.

Finkbeiner, D. P. *ApJ*, 614:186–193, 2004.

Franco, G. A. P., et al. *ApJ*, 723:146–165, 2010.

Fukagawa, M., et al. *ApJL*, 636(2):L153–L156, 2006.

Gaia Collaboration, et al. *Astronomy & Astrophysics*, 616:A1, 2018.

Galametz, M., et al. *Astronomy & Astrophysics*, 616:A139, 2018.

Galli, D. et al. *ApJ*, 417:220, 1993a.

Galli, D. et al. *ApJ*, 417:243, 1993b.

Galliano, F. *MNRAS*, 476(2):1445–1469, 2018.

Génova-Santos, R., et al. *MNRAS*, 452:4169–4182, 2015.

Girart, J. M., et al. *ApJL*, 856(2):L27, 2018.

Girart, J. M., et al. *Science*, 324(5933):1408, 2009.

Greaves, J. S., et al. *MNRAS*, 340(2):353–361, 2003.

Greaves, J. S., et al. *Nature Astronomy*, 2:662–667, 2018.

Griffin, M. J., et al. *Astronomy & Astrophysics*, 518:L3, 2010.

Griffith, M. R., et al. *ApJ Supplement Series*, 90:179, 1994.

Guillet, V., et al. *Astronomy & Astrophysics*, 634:L15, 2020.

Gunkelmann, N., et al. *Astronomy & Astrophysics*, 589:A30, 2016.

Habart, E., et al. *Astronomy & Astrophysics*, 397:623–634, 2003.

Harper, S. E., et al. *MNRAS*, 453:3375–3385, 2015.

Healey, S. E., et al. *ApJ Supplement Series*, 171:61–71, 2007.

Hennebelle, P., et al. *Astronomy & Astrophysics*, 528:A72, 2011.

Hensley, B., et al. *MNRAS*, 449:809–819, 2015.

Hensley, B. S. et al. *ApJ*, 834:134, 2017a.

Hensley, B. S., et al. *ApJ*, 827:45, 2016.

Hensley, B. S. et al. *ApJ*, 836(2):179, 2017b.

Higdon, S. J. U., et al. *ApJ*, 787(2):103, 2014.

Hoang, T., et al. *ApJ*, 741:87, 2011.

Hoang, T., et al. *ApJ*, 824:18, 2016.

Hoang, T. *arXiv e-prints*, art. arXiv:1511.05997, 2015.

Hoang, T. et al. *ApJ*, 697(2):1316–1333, 2009.

Hoang, T. et al. *ApJ*, 821(2):91, 2016.

Hoang, T., et al. *ApJ*, 862(2):116, 2018.

Hocuk, S., et al. *Astronomy & Astrophysics*, 604:A58, 2017.

Houk, N. et al. *Michigan Catalogue of Two-dimensional Spectral Types for the HD Stars. Volume 4, Declinations -26*deg.*0 to -12*deg.*0.* 1988.

Hull, C. L. H., et al. *ApJ*, 768:159, 2013.

Hull, C. L. H., et al. *ApJS*, 213:13, 2014.

Hull, C. L. H. et al. *Journal of Astronomical Instrumentation*, 4, 2015.

Hull, C. L. H. et al. *Frontiers in Astronomy and Space Sciences*, 6:3, 2019.

Hull, C. L. H., et al. *ApJ*, 860(1):82, 2018.

Isella, A., et al. *ApJ*, 775(1):30, 2013.

Jones, A. P. et al. *Astronomy & Astrophysics*, 530:A44, 2011.

Jones, A. P. et al. *Astronomy & Astrophysics*, 627:A38, 2019.

Joos, M., et al. *Astronomy & Astrophysics*, 543:A128, 2012.

Kataoka, A., et al. *Astronomy & Astrophysics*, 568:A42, 2014.

Kataoka, A., et al. *ApJ*, 809(1):78, 2015.

Keppler, M., et al. *Astronomy & Astrophysics*, 639:A62, 2020.

Kim, S.-H., et al. *ApJ*, 422:164, 1994.

Koch, P. M., et al. *ApJ*, 797(2):99, 2014.

Kogut, A., et al. *ApJ*, 460:1, 1996.

Konigl, A. et al. *Protostars and Planets IV*, page 759, 2000.

Krause, M. et al. *Phys. Rev. Lett.*, 93:021103, 2004.

Ladjelate, B., et al. *Astronomy & Astrophysics*, 638:A74, 2020.

Lam, K. H., et al. *MNRAS*, 507(1):608–620, 2021.

Lazarian, A. *Journal of Quantitiative Spectroscopy and Radiative Transfer*, 106:225–256, 2007.

Lazarian, A. et al. *ApJL*, 536(1):L15–L18, 2000.

Lebreuilly, U., et al. *ApJL*, 917(1):L10, 2021.

Lee, J. W. Y., et al. *ApJ*, 834(2):201, 2017.

Leger, A., et al. *Physical Review Letters*, 60:921–924, 1988.

Leitch, E. M., et al. *ApJL*, 486:L23+, 1997.

Leone, F. *MNRAS*, 382(4):1690–1696, 2007.

Liseau, R., et al. *Astronomy & Astrophysics*, 344:342–354, 1999.

Lopez-Rodriguez, E., et al. *ApJ*, 893(1):33, 2020.

Louvet, F., et al. *Astronomy & Astrophysics*, 570:A15, 2014.

Louvet, F., et al. *Astronomy & Astrophysics*, 596:A88, 2016.

Louvet, F., et al. *Astronomy & Astrophysics*, 618:A120, 2018.

Marino, S., et al. *ApJL*, 798(2):L44, 2015.

Mathis, J. S., et al. *ApJ*, 217:425–433, 1977.

Matsushita, Y., et al. *MNRAS*, 475:391–403, 2018.

McMullin, J. P., et al. In *Astronomical Data Analysis Software and Systems XVI*, volume 376, page 127, 2007.

Meisner, A. M. et al. *ApJ*, 781:5, 2014.

Min, M., et al. *Astronomy & Astrophysics*, 604:L10, 2017.

Miotello, A., et al. In Inutsuka, S., et al., editors, *Protostars and Planets VII*, volume 534 of *Astronomical Society of the Pacific Conference Series*, page 501, 2023.

Miyake, K. et al. *Icarus*, 106(1):20–41, 1993.

Motte, F., et al. *Nature Astronomy*, 2:478–482, 2018.

Murphy, E. J., et al. *ApJL*, 709:L108–L113, 2010a.

Murphy, E. J., et al. *ApJ*, 862:20, 2018.

Murphy, T., et al. *MNRAS*, 402(4):2403–2423, 2010b.

Nolan, P. L., et al. *ApJ Suplement Series*, 199(2):31, 2012.

Nony, T., et al. *Astronomy & Astrophysics*, 636:A38, 2020.

Okuzumi, S., et al. *The Astrophysical Journal*, 752(2):106, 2012.

Padgett, D. L., et al. *ApJ*, 672(2):1013–1037, 2008.

Padin, S., et al. *Publications of the ASP*, 114:83–97, 2002.

Pearson, T. J., et al. *ApJ*, 591(2):556–574, 2003.

Pérez, L. M., et al. *ApJL*, 869(2):L50, 2018.

Pilbratt, G. L., et al. *Astronomy & Astrophysics*, 518:L1, 2010.

Pilleri, P., et al. *Astronomy & Astrophysics*, 542:A69, 2012.

Pinilla, P., et al. *ApJ*, 868(2):85, 2018.

Planck Collaboration, et al. *Astronomy & Astrophysics*, 536:A20, 2011.

Planck Collaboration, et al. *Astronomy & Astrophysics*, 557:A53, 2013.

Planck Collaboration, et al. *Astronomy & Astrophysics*, 571:A11, 2014a.

Planck Collaboration, et al. *Astronomy & Astrophysics*, 571:A12, 2014b.

Planck Collaboration, et al. *Astronomy & Astrophysics*, 565:A103, 2014c.

Planck Collaboration, et al. *Astronomy & Astrophysics*, 582:A28, 2015.

Planck Collaboration, et al. *Astronomy & Astrophysics*, 586:A138, 2016a.

Planck Collaboration, et al. *Astronomy & Astrophysics*, 586:A136, 2016b.

Pohl, A., et al. *Astronomy & Astrophysics*, 593:A12, 2016.

Potapov, A., et al. *Physical Review Letters*, 124(22):221103, 2020.

Price, D. J., et al. *MNRAS*, 477(1):1270–1284, 2018.

Qiu, K., et al. *ApJL*, 794:L18, 2014.

Readhead, A. C. S., et al. *ApJ*, 609(2):498–512, 2004a.

Readhead, A. C. S., et al. *Science*, 306(5697):836–844, 2004b.

Remjian, A., et al. 2019, 2019.

Ricca, A., et al. *ApJ*, 754(1):75, 2012.

Rieke, G. H., et al. *ApJ Suplement Series*, 154:25–29, 2004.

Rybicki, G. B. et al. *Radiative processes in astrophysics*. 1979.

Sadjadi, S., et al. In *Journal of Physics Conference Series*, volume 728 of *Journal of Physics Conference Series*, page 062003, 2016.

Scaife, A. M. M., et al. *MNRAS*, 403:L46–L50, 2010a.

Scaife, A. M. M., et al. *MNRAS*, 406(1):L45–L49, 2010b.

Schlemmer, S., et al. *Laboratory Astrochemistry*. 2015.

Sellgren, K., et al. *ApJ*, 299:416–423, 1985.

Seok, J. Y. et al. *ApJ*, 835(2):291, 2017.

Shu, F. H., et al. *Protostars and Planets IV*, pages 789–814, 2000.

Shu, F. H., et al. *Annual Review of Astronomy and Astrophysics*, 25(1):23–81, 1987.

Shu, F. H., et al. *ApJ*, 601(2):930–951, 2004.

Shu, Q., et al. *Metallurgical and Materials Transactions B*, 52(3):1818–1829, 2021.

Siebenmorgen, R. et al. *Astronomy & Astrophysics*, 543:A25, 2012.

Sierra, A. et al. *ApJ*, 892(2):136, 2020.

Sierra, A., et al. *ApJ*, 876(1):7, 2019.

Sofia, U. J. et al. In *American Astronomical Society Meeting Abstracts*, volume 199, page 91.11, 2001.

Sowards-Emmerd, D., et al. *ApJ*, 609:564–575, 2004.

Sridharan, T. K., et al. *ApJL*, 783:L31, 2014.

Stolker, T., et al. *Astronomy & Astrophysics*, 607:A42, 2017.

Tang, Y.-W., et al. *ApJL*, 947(1):L5, 2023.

Taylor, A. C., et al. *MNRAS*, 418:2720–2729, 2011.

Testi, L., et al. In Beuther, H., et al., editors, *Protostars and Planets VI*, page 339, 2014.

Tibbs, C. T., et al. *MNRAS*, 418:1889–1900, 2011.

Tibbs, C. T., et al. *ApJ*, 768(2):98, 2013.

Tibbs, C. T., et al. *MNRAS*, 456(3):2290–2300, 2016.

Tielens, A. G. G. M. *Ann. Rev. of Astron. and Astroph.*, 46:289–337, 2008.

Tielens, A. G. G. M. et al. In *Physical Processes in Interstellar Clouds*, volume 210, pages 333–376, 1987.

Tomisaka, K. *MNRAS*, 298(3):797–810, 1998.

Tsukamoto, Y., et al. *ApJ*, 868(1):22, 2018.

Umurhan, O. M., et al. *ApJ*, 895(1):4, 2020.

University of Cambridge. 2012. http://web.archive.org/web/20080207010024/http://www.808multimedia.com/winnt/kernel.htm [Accessed: 06-07-2023].

Vaillancourt, J. E. *Publications of the ASP*, 118:1340–1343, 2006.

van der Marel, N., et al. *Astronomy & Astrophysics*, 579:A106, 2015.

van der Marel, N., et al. *Astronomy & Astrophysics*, 585:A58, 2016.

van der Plas, G., et al. *Astronomy & Astrophysics*, 624:A33, 2019.

van Holstein, R. G., et al. *Astronomy & Astrophysics*, 633:A64, 2020.

Vidal, M., et al. *MNRAS*, 414:2424–2435, 2011.

Vidal, M., et al. *MNRAS*, 495(1):1122–1135, 2020.

Watanabe, M., et al. In *Ground-based and Airborne Instrumentation for Astronomy VII*, volume 10702, 2018.

Watson, R. A., et al. *ApJL*, 624:L89–L92, 2005.

Whittet, D. *Dust in the Galactic Environment*. 2022.

Williams, J. P., et al. *ApJL*, 875(2):L9, 2019.

Witt, A. N., et al. *ApJ*, 636:303–315, 2006.

Wolff, M. J., et al. *ApJ*, 423:412, 1994.

Wright, E. L., et al. *The Astronomical Journal*, 140:1868–1881, 2010.

Ysard, N., et al. *Astronomy & Astrophysics*, 509:L1, 2010.

Ysard, N., et al. *Astronomy & Astrophysics*, 535:A89, 2011.

Zhang, B., et al. *ApJ*, 781(2):89, 2014a.

Zhang, Q., et al. *ApJ*, 792:116, 2014b.

Zhu, Z. et al. *MNRAS*, 458(4):3918–3926, 2016.

Zurlo, A., et al. *MNRAS*, 496(4):5089–5100, 2020.